UNIVERSIDAD DE CHILE
FACULTAD DE CIENCIAS FÍSICAS Y MATEMÁTICAS
DEPARTAMENTO DE GEOLOGÍA

GAS-TRANSPORTED ELEMENTS AS AN EXPLORATION TECHNIQUE UNDER POST-MINERAL COVER: ATLÁNTIDA DEPOSIT AND SURROUNDINGS

TESIS PARA OPTAR AL GRADO DE MAGISTER EN CIENCIAS, MENCIÓN GEOLOGÍA

MEMORIA PARA OPTAR AL TÍTULO DE GEÓLOGA

PAULINA IGNACIA PIZARRO PAVEZ

PROFESOR GUÍA:
BRIAN TOWNLEY CALLEJAS

PROFESOR CO-GUÍA:
MCLEAN TROTT

MIEMBROS DE LA COMISIÓN:
XAVIER EMERY
KATJA DECKART
DAVID HOPPER

SANTIAGO DE CHILE
MARCH 2016

Abstract

Soil gas sampling technique by means of passive collectors devices (OreHound®) was carried out over the Atlántida porphyry deposit, located in the Atacama Region of northern Chile. Atlántida is a porphyry Cu-Au-Mo deposit with adjacent development of skarn, in the contact between intrusives and limestones, and it is almost completely covered by post-mineral pediment gravels, ranging from 5-80 meters in thickness.

Because of the wide combination of preexistent analysis (38 drillcores, surface mapping, surface geochemistry and geophysical data) plus the known of extent and its location in an arid climate, Atlántida is a suitable place to test the usefulness of gas sampling through collectors and figure if it is effective at reducing an exploration area to the scale of the deposit. Furthermore, the combination of high seismicity and hyper-aridity makes this region ideal for employing the anomalies in prospecting for concealed mineral deposits (Cameron et al., 2002).

A total of 234 collectors were installed over Atlántida and surroundings and, after three months in the field, were retrieved and analyzed by ALS Chemex by their Super Trace aqua regia technique (ME-MS41L). From basic statistics of the results, it was determined that there is clear capture of signal to present real time processes, evidenced by lower and higher concentrations than the blanks. To localize contrast anomalies, univariate and multivariate methods are used in this study in order to define background and anomalous concentrations. 'Rabbit ear' anomaly patterns were obtained in two WE profiles sections above Atlántida. Semi-anular anomaly patterns were obtained in the factor analysis interpolation maps and in the raw data ordinary cokriging interpolation maps above Atlántida. In particular, the elements Cu, Mn, Pb, Rb and Sr showed background values over the concealed deposit and positive anomalous values adjacent to it. On the other side, Zn showed a positive contrast anomaly over the deposit with background concentrations around it. Such patterns are believe to represent present oxidation processes and are most likely explained in terms of chemical dispersion mechanisms. Another factor shaping the surficial gas anomalies found in this study is the existence of preferential pathways (faults and/or fractures) through which gases move from underground upward to the surface.

Resumen

La técnica de muestreo de gases en suelo por medio de colectores pasivos (OreHound®) se llevó a cabo sobre el depósito de pórfido Atlántida, ubicado en la Región de Atacama en el norte de Chile. Atlántida es un pórfido Cu-Au-Mo con desarrollo adyacente de skarn, en el contacto entre intrusivos y calizas, y esta casi completamente cubierto por pedimento de gravas post-mineral, que van desde los 5-80 metros en espesor.

Debido a la amplia combinación de análisis preexistentes (38 pozos perforados, mapeo de superficie, geoquímica de superficie y datos geofísicos), además de la conocida extensión del depósito y su ubicación en un clima árido, Atlántida es un lugar adecuado para poner a prueba la utilidad del muestreo de gas a través de colectores y descubrir si es eficaz en la reducción de un área de exploración a la escala del depósito. Por otra parte, la combinación de alta sismicidad y la híper-aridez hace que esta región sea ideal para el empleo de las anomalías en la prospección de yacimientos minerales ocultos (Cameron et al., 2002).

En total 234 colectores fueron instalados sobre Atlántida y sus alrededores y, después de tres meses enterrados en terreno, fueron recuperados y analizados por ALS Chemex por su técnica Super Traza aqua regia (ME-MS41L). A partir de la estadística básica de los resultados, se determinó que existe una clara captura de señal a los procesos en tiempo real, evidenciado por concentraciones más bajas y más altas respecto a la de los blancos. Para localizar anomalías de contraste, métodos univariantes y multivariantes se utilizan en este estudio con el fin de definir concentraciones background y anómalas. Anomalías con forma 'oreja de conejo' se obtuvieron en dos secciones WE sobre Atlántida. Patrones de anomalías semi-anulares se obtuvieron en los mapas de interpolación de análisis de factores y en los mapas de la interpolación de los datos originales por cokriging ordinario sobre Atlántida. En particular, los elementos Cu, Mn, Pb, Rb y Sr mostraron concentraciones background sobre el depósito oculto y positivas concentraciones anómalas adyacentes a la misma. Por otro lado, Zn mostró una anomalía de contraste positiva sobre el depósito con concentraciones background alrededor de ésta. Tales patrones se creen representan procesos de oxidación actuales y son probablemente explicados en términos de mecanismos de dispersión químicos. Otro factor que regula las anomalías en superficie presente en este estudio es la existencia de vías preferenciales (fallas y/o fracturas) a través de las cuales los gases se mueven desde el frente de oxidación hacia la superficie.

TABLE OF CONTENT

LIST OF FIGURES

LIST OF TABLES

Chapter 1

Introduction

Mineral exploration and mining companies around the world have experienced a global trend towards the discovery of mineral deposits under post-mineral cover (Figure 1.1) in the 60 years preceding 2015, wherein new ore bodies are being located progressively deeper or under significant overburden (Richard Schodde, 2014). In this scenario, the rate of greenfield discoveries has decreased while the rate of brownfield discoveries has increased.

In order to more effectively explore covered areas, particularly in the greenfield environments, new techniques as well as poorly understood existing techniques require further study to validate them for integration into more traditional approaches to exploration.

This thesis attempts to test the usefulness and pitfalls of an existing surface technique, in this case using OreHound® collectors, a method consisting of adsorption of gases rising from the subsurface and accumulated in collector devices placed beneath the surface of the soil. The premise of this technique is that bacterial activity related to oxidation of deeply buried or covered ore bodies produces gases and liberates metal ions which are transported to the surface via a number of possible gas transport mechanisms (electrochemical processes, cyclical dilatancy pumping, etc). This technique relies on gas-transported metal anomaly detection and definition rather than direct detection of these gases at surface. The effective interpretation of geochemical data derived thusly involves consideration of multiple populations of data and robust statistical analysis.

This technique has been used historically, as indicated by Howard et al. (1986). Over time, the technique has changed in terms of the device shape, the absorbant material and exposure time. According to Howard et al. (1986), Hinkle and Kantor (1978) used artificial zeolites as gas collectors. Later on Klusman and Voorhees (1983) used a thin wire coated with activated charcoal buried in a cup about 15-30 cm below the surface

and retrieved them after 1-2 weeks. Pauwels et al. (1999) used activated carbon held inside a bag of Gore-Tex within a cylindrical plastic container and retrieved them form the soil after 100 days. More recently in Cameron et al. (2004), collector devices similar to Pauwel's were installed in the Mike deposit[1], where they were placed at the top of a 50 cm length PVC pipe inserted into auger holes, leaving the collectors above ground and later retrieving them after three months.   Similar collectors were installed over the Spence deposit and at a background location west of the deposit, and in this case were retrieved after one year.

Similar studies were conducted during research and development of the OreHound geo-organo chemical collectors, these as part of state funded R&D projects and published in Townley et al. (2007).

There are many variables associated with gas geochemistry, most to do with metal ion transport mechanisms. Previously investigated metal ion transport mechanisms include electrochemical cell(s), gaseous flux or barometric pumping (Cameron et al., 2004; Aspandiar et al., 2008). However, it may be assumed that in differing environments combinations of varying transport mechanisms are at work to different extents, depending upon cover composition, depth, hydrological regime and the presence or absence of structural conduits. Another important variable in historical tests of this technique is the elution method used since batch level shift problems have been observed in several historical studies.

In summary, this study emphasizes transport of metal ions through overburden via gaseous mechanisms, and attempts to assess the feasibility of utilizing gas-transported geochemistry through collectors installed under real world circumstances as a cost effective exploration tool for the modern explorer.

---

[1] The Mike deposit in Nevada, is a Cu-Au deposit hosted by sedimentary rocks.
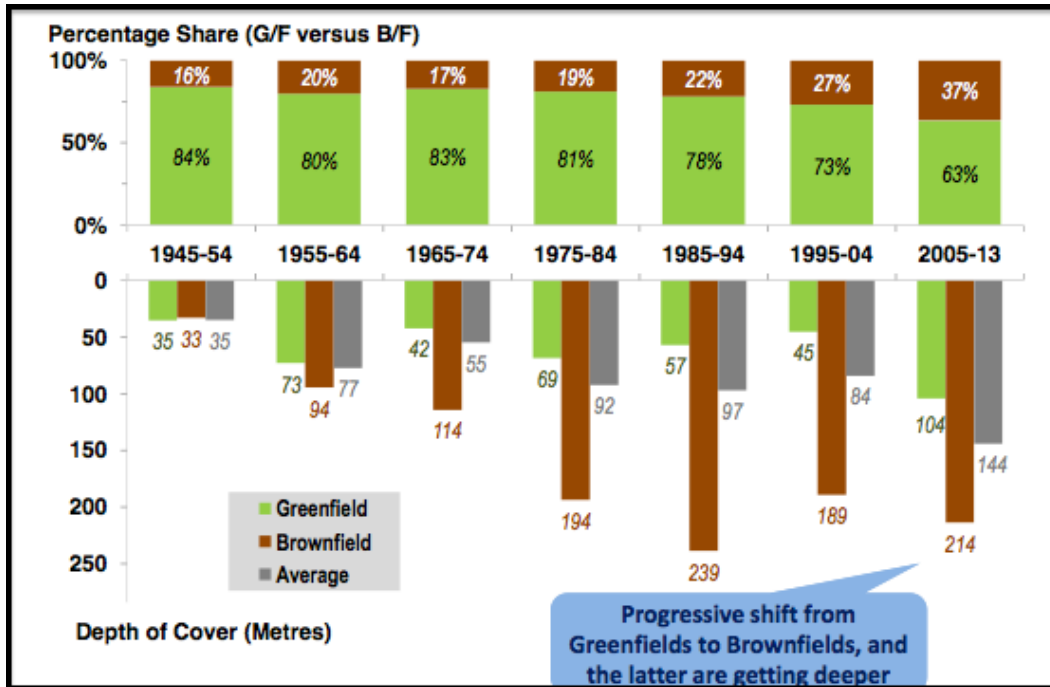
Figure 1.0.1. Cumulative base metal discoveries (greenfields and brownfields) in the World diagram illustrating transition toward deeper cover (Schodde, 2014).
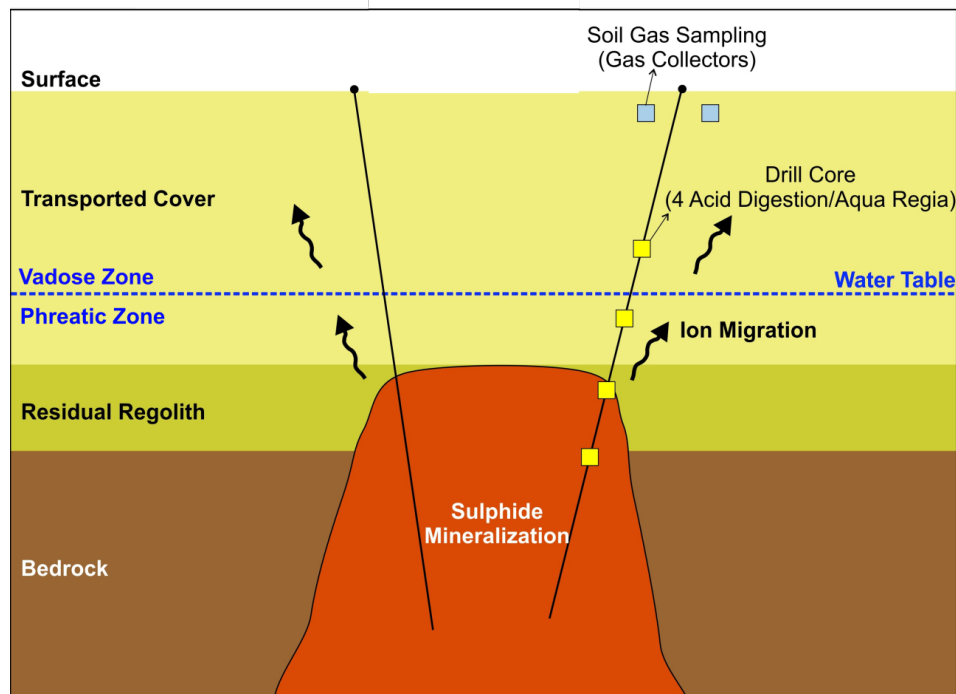
Figure 1.0.2. Cartoon diagram showing the relative positions of samples and respective analytical techniques used in this study.

1.1 Project Aims and Objectives

1.1.1 General Aim

The aim of the present study is to assess the usefulness of trace level metals analysis applied to activated carbon passive collectors as a cost-effective and potentially robust exploration tool in areas dominated by post-mineral overburden. As this is a relatively new approach (albeit to an old technique) to exploration under cover, the study will also attempt to address the pitfalls and technical details involved in applying this or similar techniques.

1.1.2 Specific Aims

Assessment of which metals are liberated at the oxidation front and transported upwards via gaseous mechanisms.

Understand the nature and extent of the footprint (if any) of metal ions transported via gaseous mechanisms above a copper sulfide deposit.

This thesis attempts to assess what geological, alteration, or prospectivity information may be interpreted from gaseous geochemical data collected by artificial collectors.

1.2 Hypothesis

Oxidation of sulfide minerals at the active oxidation front above a buried ore deposit generates ions and gaseous compounds (inorganic and organic) that migrate upward until reaching the surface. Components of the regolith then adsorb the particles that have migrated to surface, developing metal contrast anomalies. In this case, the OreHound® detectors attempt to enhance contrast anomalies derived from gas-transported metals by providing a homogenous, adsorptive sample medium in the form of activated carbon, thereby minimizing the effects of regolith composition which are a common pitfall of several commonly used partial leach geochemical techniques applied on in situ soil samples.

Metal contrast anomalies may be detected at surface by trace element analysis of activated carbon sachets extracted from the collectors, which have accumulated adsorbed metals transported by gases. Such metal anomalies may be distinctive of copper sulfide orebodies and reflective of the ore and/or alteration chemistry of the deposit in question.

1.3 Study Area

Location and Access

The Atlántida prospect is located in the 'III Región de Atacama', northern Chile, approximately 60 km NE of Copiapó city (Figure 1.3), at an elevation of 1,700 m. The project is located in the Upper Cretaceous porphyry belt of the Chilean Andes, about 25 km SW of the Inca de Oro Cu-Au-Mo porphyry deposit, 15 km SW of Carmen, and 20 km SW of the Dinamarquesa project. Figure 2.6 shows a location map of Atlántida prospect relative to major porphyry deposits in the area.

Access from Copiapó is by the 'Carretera del Inca' followed by the C17 highway, which connects Copiapó with Diego de Almagro. A left turn is taken in Flamenco – Bella Ester, near Carrera Pinto, after which 8 km of an unpaved but stable road called C261 leads to the prospect.

Figure 1.0.3. Location map showing the Atlántida project relative to urban centers in the region.

1.4 Methodology

This study contains two main components:

Field work

Field work consisted of:

- Core-logging of drillholes on an east-west type section that crosses the mineralized prospect. It consists of seven diamond drill cores for a total of 4,500 meters. This was intended to provide context to later analytical results by understanding the geology, alteration, morphology, and geochemical behavior of the deposit. Core-logging was done with an 'assay in hand' approach in an attempt to characterize distinctive geochemical characteristics of different geological subdivisions with the potential to later be reflected in OreHound results.

- Installation and subsequent removal of OreHound® activated carbon gas collectors on a 500 m spaced staggered grid above Atlántida, consisting of 234 passive gas collectors, buried at 30 to 40 cm depth for a period of three months.

Office work

Involved literature review during the whole process, compilation of old and new data, processing and interpretation of all data available and statistical analysis of such.

1.5 Background

Geochemical dispersion is the process by which atoms and particles move to new locations and geochemical environments (Rose et al., 1979). Dispersion of metals from buried deposits through transported or in situ cover regimes are in mobile forms such as ions or micro-particles carried upward by water or gas, which can occur either in the phreatic zone[2] or in the vadose zone[3].

Any upward movement of ions and particles through transported cover requires a medium (water, air, mineral particles) and a driving force (concentration, electrical,

---

[2] Phreatic or satured zone: zone below the water table in which all the pore spaces are filled with water (except for phenomena such as natural gas traps).
[3] Vadose or unsaturated zone: zone above the water table, only periodically saturated with water.

temperature, density or pressure gradients) to drive the upward transfer of elements and compounds via diffusion[4] or advection[5] (Aspandiar et al., 2008).

This review discusses the main hypotheses regarding geochemical dispersion mechanisms responsible for potential surface anomalies above a buried sulfide body. Moreover, the processes described below are well documented and known to be active factors in ion transport in northern Chile.

Migration of gases

Similar to dissolved solids in water, gases may migrate by diffusion through air or water, or advectively, as a result of the movement of a mass of air or water containing the gases (Cameron, 2004). For gases, as for dissolved solids in water, advective flow is a far more rapid and effective transport mechanism than diffusion of ions in water or gases in air, which is orders of magnitude slower, particularly through vadose zones and clay units (Cameron et al., 2004). Adherence of trace element compounds to volatiles may, however, aid in the transport through the vadose zone (Clark, 1996; Clark, 1997).

The movement of gases below the water table primarily involves movement in an aqueous solution. This can take place either by diffusion through the water or by mass transport of the water itself. Above the water table, movement of gases takes place by a combination of diffusion and mass transport. At the water table, the movement of gases across the water-air interface is by evaporation or condensation (Rose et al., 1979).

Although movement of water in the subsurface may not seem relevant to gaseous transport, understanding aqueous processes is key to understanding gaseous processes, as both transport media are affected by similar factors. Above and beyond that, dissolved gases in aqueous solution may be re-distributed substantially by aqueous processes prior to separation and subsequent gaseous migration above the water table (as mentioned above).

Barometric pumping

Barometric pumping provides a mechanism for the advective transfer of gases to the surface in arid terrains with a thick, fractured vadose zone (Cameron et al., 2004). It is the process wherein cycles of high and low barometric pressure (perhaps even diurnal variation) first force air into the earth and then withdraw a mixture of the air plus gases

---

[4] Diffusion is the net movement of material from an area of high concentration to an area with lower concentration. The difference of concentration between the two areas is often termed as the concentration gradient, and diffusion will continue until this gradient has been eliminated.
[5] Advection is the transport mechanism of a substance by fluid flow.

that were in the rock. Barometric pumping applies only to fractured rock. In unbroken materials, even if they are permeable, the process is not significant.

According to Cameron et al., (2004, largely derived from Nilson et al., (1991)), high barometric pressure forces air down fractures and into pore space in the rock around the fractures. Gases within the rock, such as CO_2 or hydrocarbons, mix with air by molecular diffusion. When the barometric pressure drops, air in the porous rock, now containing the gases, returns to the fracture and, after several cycles of high and low pressure, reaches the surface. Pumping occurs because the volume of air entering rock porosity is much greater than the volume of air present in the fractures. For a fractured permeable medium, barometric transport can be several orders of magnitude greater than molecular diffusion, whereas for unfractured soil and alluvium, molecular diffusion is more important.

According to Rose et al. (1979), aside from changes in pressure, other factors that exert an effect on the flow of air in the vadose zone are temperature and moisture[6]. Regarding the temperature, an increase of surface temperature not only causes soil air to expand and escape, but also tends to release vapor species adsorbed to the surface of soil particles. If the heating of surface soils is uneven, lateral flow of air may occur. Similarly, convection of soil air may occur in the pore space within hills, because of temperature gradients created in horizontal planes by heating the hillsides. Finally, the fluctuations in pressure and temperature operate on a daily cycle (Turk, 1975) and over longer periods. The net effect of this process is an outward movement of the gases generated at depth at rates faster than diffusion, and corresponding inward movement of atmospheric air.

Bubble Migration

The following descriptions are taken from Aspandiar (2004) and Aspandiar et al. (2008). According to the authors, bubble migration (also called Gas Streaming) is a potential gas and metal transfer mechanism acting in the phreatic zone and it is the upward transfer of microscopic gas bubbles that form within the groundwater due to overpressure, and are then released from the water table. During their ascension, the bubbles (dominantly composed of CO_2) can attach specific metals (Cu, Zn, Pb, Hg, actinides) and ultra-fine particles (clays, oxides, bacteria) to their surfaces. The bubbles release metals when pressure changes induce instability, although the stability of bubbles during their transfer from a saturated to an unsaturated medium is unclear. For more details see references.

---

[6] Moisture refers to the presence of a liquid, especially water, often in trace amounts. Moisture also refers to the amount of water vapor present in the air.
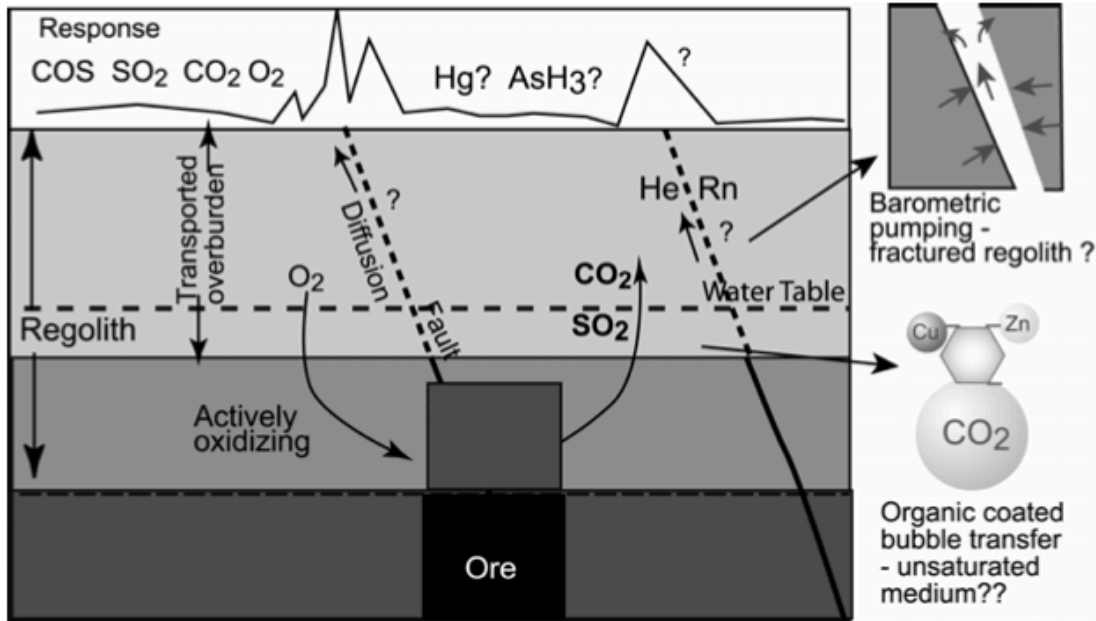
Figure 1.0.4. Illustration of potential gas migration mechanism through transported regolith. Aspandiar, 2004.

Migration of dissolved solids in water

Electrochemical cells

A phreatic process that involves the movement of charged ions within an electrical field generated by the presence of an oxidizing orebody. It requires saturated sediment cover and discrete massive sulfide mineralization. The main concept behind this dispersion model is the rapid upward migration of metal in solution or along the sulfide ore (Aspandiar et al., 2009) which can be considered a conductor immersed in an electrolyte, groundwater (Cameron, 2004).

Spontaneous Potential

First proposed by Sato & Mooney (1960) and later extended by Govett (1973; 1976), Bolviken and Logn (1975). This model explains the development of self-potentials associated with sulfide bodies in response to the development of an Eh differential along its length. The upward force is generated by electrical or redox potential differences between the underlying (reducing, anodic) and the overlying (oxidizing, cathodic) parts of the sulfide body. In fact, within the deeper areas (below the water table) of the conductive ore, oxidation of the reducing agents proceeds along the edges of the conductor between sulfide minerals and the electrolyte (groundwater), releasing

electrons. The electrons move upwards through the conductive sulfide body to locations where oxygen or other oxidants are available and take part in its cathodic reduction. The simultaneous oxidation and reduction give rise to an Eh differential between the near surface (cathodic) and deeper areas (anodic) resulting in current flow, carried by ions in the groundwater. Cations migrate to the cathode and anions to the anode (Cameron, 2004). According to Govett (1976), the cathode edges around the oxidized sulfide body served as high cation densities with a cation deficient zone in between. The accumulations of cations at the edges of the cathode subsequently diffuse upwards along concentration gradients to the surface and collect in soil horizons resulting in twin H$^+$ responses and in a soil pH change (Smee, 1983).
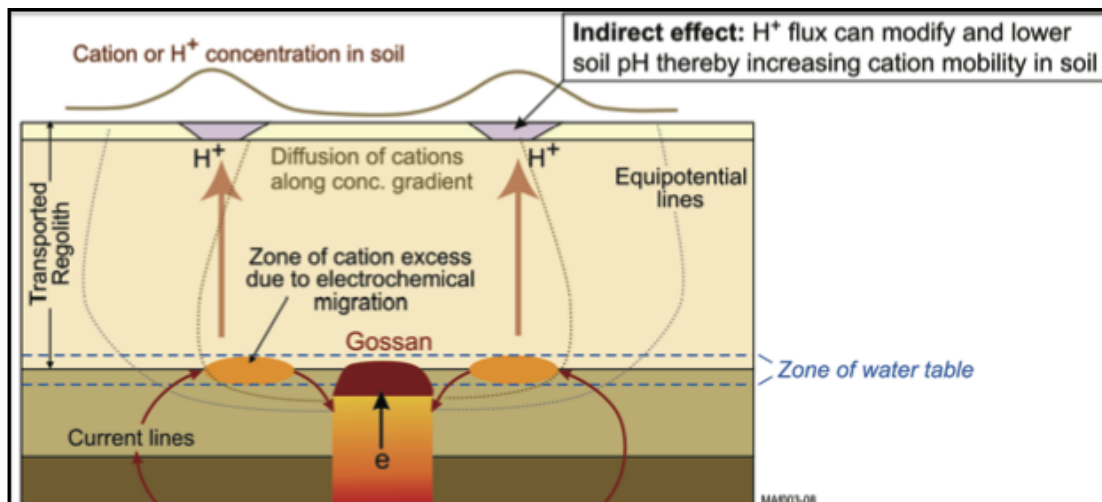
Figure 1.0.5. Conceptual model by for the electrochemically induced dispersion in arid terrain. Electrochemical cell set up with generation of excess cations at the edges of the conductor (sulphide) and their subsequent diffusion through unsaturated cover. The diffusion results in excess H+ within the soil which in turn affects mobility of exchangeable ions (indirect pathway). Aspandiar et al. 2008 (Modified from Govett et al. 1984).

Dilatancy Pumping

Sibson (1975) termed dilatancy pumping as the process of groundwater pumping along faults and fracture systems in neo-tectonically active areas. The theory behind this is based on the existence of pre-seismic fractures in the brittle upper crust, acting as storage compartments and pathways for groundwater movement (Aspandiar et al., 2008). During and after earthquake events, the compressional stress causes fault closure resulting in the release of metal-bearing groundwater along faults to areas of lower pressure at the surface. This mechanism is limited to areas located in arid climates (low-rainfall) and neo-tectonic areas that have regular seismic activity. The high evaporation rates in semi-arid and arid settings result in the transferred metals being incorporated into the soils in close proximity to the mineralization, rather than widespread dispersion at the surface (Aspandiar et al, 2008).

10

Studies carried out in northern Chile by Cameron et al (2002; 2004) successfully indicate that cyclical dilatancy pumping explain the surface geochemical contrast anomalies in areas with a thick vadose zone. Whilst these anomalies are derived from metals carried in aqueous solution, dissolved gases in the subsurface are similarly affected by re-distribution driven by dilatancy pumping.

The Deep Penetrating Geochemistry Phase I and II of the CAMIRO project demonstrated that in hyper-arid, tectonically active terranes such as northern Chile, movement of water by seismic activity is a viable mechanism for the production of surficial geochemical contrast anomalies (Cameron, 1998; Cameron et al., 2008). In particular, northern Chile is a region of high seismicity and the rate of erosion is mostly too low to disperse anomalies derived from seismic-related flooding once they have formed (Cameron et al., 2008). Movement of water in the subsurface is indeed relevant to this study, as dissolved gases in such waters may be redistributed notably before separated from solution and rising to surface with their load of adsorbed metals.

Chapter 2

Geological Background

2.1 Regional Geological Setting

The area of study is comprised of rocks belonging to the Jurassic and Cretaceous periods and Paleocene epoch (Lower Paleogene), primarily the results of an important tectonic change marked by the onset of the Andean tectonic cycle with the initiation of subduction-related magmatism. Figure 2.1 shows the setting of the study area.

The evolution of the Andes of northern Chile during this cycle can be divided into two major stages:

(1) from the Jurassic to the end of the Early Cretaceous, when a magmatic arc system flanked on the east side by a sedimentary marine back-arc basin was developed within an extensional tectonic setting.

(2) from the Late Cretaceous to the present, when arc systems developed in a continental environment within an overall compressional tectonic setting (Maksaev, 2005). This compressive regime was critical in terms of porphyry system development in the Andes, as an overall compressive environment enabled long term fractionation processes to proceed without degassing magma chambers through the regular volcanism typical of more extensional regimes, allowing the generation of large volumes of magmatic-hydrothermal fluids (Cooke et al., 2005; Sillitoe, 1998).

Figure 2.0.1. Chañarcillo basin Tectono-stratigraphic chart showing a generalized stratigraphy of northern Chile and magmatic arc and deformation migration towards the east since Early Cretaceous time coeval with the beginning of a contractional regime in the South American plate. CCP: Coastal Cordillera-Precordillera. Modified from Amilibia (2009).

2.2 Regional Geology

The geological framework of the project area is mainly taken from Sernageomin's Copiapo 1:100,000 scale mapsheet (Matthews et al., 2006), and the stratigraphic regional representative sequence is presented in Figure 2.2.

2.2.1 Stratigraphic Sequence / Regional Stratigraphy

The units described in this chapter are listed from oldest to youngest as follow:

Figure 2.0.2. Approximate Atlántida stratigraphic column (Modified from Martínez et al.,2012). The red star represents the chronological position of Atlántida.

La Negra Formation (201 – 191 Ma)

The La Negra Formation, a 3,000 – 10,000 m thick volcanic sequence, represents the first substage of the first Andean stage in the Copiapó region (Figure 2.2). This formation belongs to the Coastal Cordillera (Figure 2.1) and conformably overlies the late pre-Andean Hettangian-Sinemurian deposits. It is composed mainly of subaerial lava flows (amygdaloidal lavas), andesitic and basaltic in composition, with interbedded volcanic breccias and volcarenites as well as occasional calcareous beds. The lavas present are black with reddish oxidation coatings and contain large plagioclase phenocrysts with smaller pyroxene (clino and orthopyroxene) and olivine phenocrysts. These lavas commonly contain quartz and/or chlorite amygdales.

It is assigned to the mid-upper Jurassic Period (García, 1967) and is the oldest unit present in the area of study.

Punta del Cobre Formation (145 – 132 Ma)

This formation discordantly overlies the La Negra Formation. Corresponding to arc deposits of the second Andean substage, the Punta del Cobre formation has a transitional boundary with the underlying La Negra Formation (Godoy & Lara, 1998), indicating continuous Jurassic to Early Cretaceous (Valanginian) volcanic activity in the region (Arévalo, 2005a).

The Punta del Cobre Formation is a volcano-sedimentary sequence composed of two members, from bottom to top (Marschick and Fontboté, 2001):
1) The Geraldo-Negro Member, is a mainly volcanic member dominated by porphyritic andesitic lavas (with pyroxene and/or hornblende) interbedded with feldspar-rich tuffaceous sandstones, and pyroclastic breccias intruded by andesitic to dacitic porphyry stocks (Khp) and sills.

2) The Algarrobos Member, mainly volcaniclastic, is composed of fine sandstones interbedded with volcanic rock and hyaloclastic breccias, most likely corresponding to deposits of the intermediate region between the arc and the back-arc environments (Charrier et al., 2007). According to Amilibia (2009), the upper part of the Punta del Cobre Formation represents the deposits of the syn-extensional back-arc basin.

This formation hosts the iron-oxide-rich Cu-Au (-Zn-Ag) deposits of the Punta del Cobre belt (Marschik and Fontboté, 2001*b*; Arévalo et al., 2006).

Because the Punta del Cobre Formation occurs below beds attributed to the Late Valanginian-Early Hauterivian (Corvalán, 1974) and because ammonites indicate a Berriasian age for the upper part of the Algarrobos Member (Tilling, 1962), usually a (Tithonian?) – pre-Late Valanginian age is assumed (Marschick and Fontboté, 2001).

Chañarcillo Group (139 – 113 Ma)

In the Copiapó region, the marine back-arc deposits of the second Andean substage correspond to the Chañarcillo Group (Segerstrom & Parker, 1959), which interfingers to the west with the Bandurrias Group (Charrier et al., 2007). The lower deposits of this group transgressively overlie the Punta del Cobre Formation (Segerstrom & Ruiz, 1962). In the Copiapó region this formation is comprised of a sequence of richly fossiliferous deposits subdivided into four formations (from base to top): the Abundancia, Nantoco, Totoralillo and Pabellón Formations (Charrier et al., 2007, from: Tavera, 1956; Segerstrom, 1960; Segerstrom and Parker, 1959; Corvalán, 1974; Jurgan, 1977a, b; Pérez et al., 1990; Mourgues, 2004; Arévalo 2005a, b).

According to Mourgues (2007) on the basis of paleontological evidence this group of four formations ranges in age from late Berriasian to early Albian (139 – 113 Ma).

Bandurrias Group (132 – 125 Ma)

It forms a 2,500 meter thick predominantly volcanic and volcaniclastic succession with sedimentary detrital and marine calcareous intercalations. The Bandurrias Group corresponds to the transition zone between the arc to the west and the back-arc basin to the east, represented by the Chañarcillo Group (Charrier et al., from Segerstrom 1960; Segerstrom and Ruiz 1962; Jurgan 1977a, *b;* Arévalo 1995, 2005a).

Hauterivian to early Aptian in age (Charrier et al., 2007).

Cerrillos Formation (110.7 – 69.5 Ma)

Defined by Segerstrom and Parker in 1959, they estimated an aggregate thickness of more than 4,000 m. The Cerrillos Formation unconformably overlies the transitional arc-back-arc Bandurrias Group (continental) and the marine back-arc Chañarcillo Group (Arévalo 2005a,b). This continental sedimentary sequence consists of two parts (Maksaev et al., 2009):

1) A conglomeratic lower part, about 2,000 m thick, composed predominantly of red orthoconglomerate, paraconglomerate, and eastward-dipping sandstone beds, with intercalation of tuffs, andesitic lava flows, breccias, agglomerates and volcanic avalanche deposits, and local horizons of fresh-water limestone and siltstone.

2) An upper part, about 2,000 m thick, dominated by andesitic lavas, sedimentary breccias, agglomerates, and tuffs. The lavas are mostly porphyritic pyroxene-bearing andesites. The rocks are often chloritized, have abundant epidote, and appear greenish-grey to reddish-brown in outcrop. The volcanic rocks of the upper portion represent the development of a new subduction-related magmatic arc roughly located along the site of the former Early Cretaceous back-arc marine sedimentary basin of the Chañarcillo Group, thus marking an eastward shift of the magmatic foci.

The Cerrillos Formation belongs to the first volcanic deposits of the second stage of Andean evolution (Charrier et al., 2007). Nevertheless, its origin is unclear. Some authors argue that the continental sedimentation and coeval subaerial volcanism of this post-rift succession mark an abrupt change from previous syn-rift marine carbonate sedimentation within the back-arc setting (Segerstrom and Parker, 1959; Zentilli, 1974; Jurgan, 1977; Perez et al., 1990; Arévalo, 2005a,b).

In contrast, for Marschik and Fontboté (2001) and Maksaev et al. (2009), the change from marine successions of the Chañarcillo Group to continental deposits of the Cerrillos Formation have been interpreted as the transition from the Lower Cretaceous extensional regime to the Andean compressional tectonics. Coherent with the authors above, Amilibia (2009) suggests that the Cerrillos Formation was possibly deposited coeval to the contractional episode that uplifted the Chañarcillo western margin in Albian times and interpreted these syninversion deposits as the distal part of a fan-delta system located at the western border of the basin.

Finally, Martínez et al. (2012) suggest that the accumulation of the Cerrillos Formation may well be related to a post-rift thermal subsidence preceding the well-documented compressional deformation in the Hornitos Formation.

The deposition of the Cerrillos Formation resulted from tectonic uplift during the middle to late Aptian (119 to 113 Ma) of the area formerly occupied by the Early Cretaceous magmatic arc (current Coastal Cordillera) and the concurrent marine regression within the back-arc basin. This deformative episode was related to a major change from a rifted (extensional or transtensional) to a left-lateral compressional tectonic setting of the Chilean active continental margin, which also represents a major paleogeographic change in the evolution of the Chilean Andes. Partly in response to this change of the tectonic setting, a period of Cu-Au porphyry mineralization occurred along the easternmost part of the Coastal Cordillera of northern Chile, thus also marking a significant change in the metallogeny of the Chilean Andes (Maksaev et al, 2009).

Based on zircon U-Pb age determinations in the lower conglomeratic and the upper volcanic parts of the Cerrillos Formation, the deposition of this formation extended in time at least from 110.7 ± 1.7 Ma to 69.5 ± 1.0 Ma (Maksaev et al., 2009).

Early Upper Cretaceous

Intrusive Rocks of the Early Upper Cretaceous

Granodiorites, hornblende quartziferous tonalites and diorites   (95-88 Ma)

They correspond to plutons, small stocks and laccoliths intruding Jurassic to Neocomian sequences. They consist mainly of granodiorites, tonalites and quartziferous diorites, light greenish gray in color, fine to medium grained with equigranular to porphyritic textures. Based on radiometric studies, they range from 60 to 110 Ma in age (Matthews et al., 2006). The oldest intrusives are located to the west of the described segment and the youngest to the east.

Venado Formation (64 - 62 Ma)

The Venado Formation is a volcano-sedimentary continental sequence in which Sepúlveda and Naranjo (1982) and Iriarte et al. (1996) recognized three stratigraphic levels:

1) a basal level, predominantly sandy sediments,
2) an intermediate level of sedimentary breccias and
3) an upper level of andesitic lavas.

Between the latitudes 26º and 27º30'S just the upper level of this formation is present and consists of an approximately 1,500 m thick succession of trachyandesitic and dacitic lavas (reddish gray color), andesitic volcanic breccias (dark red color), a 10 m thick ignimbritic intercalation (whitish), and red sandstones and sedimentary breccias (Charrier et al., 2007).

The Venado Formation unconformably overlies the Hornitos Formation in the type locality but in the area of study, the formation unconformably rests over the Llanta and the Cerrillos Formations.

Based on U-Pb radiometric studies carried out by Matthews et al. (2006) together with the paleontological information, the formation ranges from Maastrichtian to Lower Paleocene in age (64 to 62 Ma).

Hypabyssal Intrusives (Inmet Internal Report, 2012) (60 – 66 Ma)

Small intrusive bodies intruding rocks ranging from those of the Venado Formation through all the units described above. Based on their composition two groups of intrusives are described:

1) Dacitic and andesitic porphyries, hornblende and/or biotite phyric, and

2) Mantles, sills, and pyroxene-bearing andesitic stocks. Radiometric K-Ar ages in biotite for this unit vary between 60 to 66 Ma. Preferentially located at the eastern edge of the area of study.

Geological Map
scale 1:100,000

Figure 2.0.3. Regional geology map (modified from Sernageomin's mapsheets of Copiapó, Ojos del Salado, Inca de Oro y Quebrada Salitrosa).

20

Legend

Qa
Alluvial deposits (Quaternary)
Gravel and coarse sand lenses, unbound.

Qc
Colluvial deposits (Quaternary)
Mono compositional blocks, sand matrix, unbound.

PQc
Inactive colluvial deposits (Pliocene-Pleistocene)
Gravel, sand and monomictic blocks deposits, exposed as stable colluvial cones or fans.

KPv
Venado Formation
(a) Dacitic and trachyandecitic lavas.

Kc
(2) **(1)**
Cerrillos Formation (Albian-Turonian)
(2) Upper Level: sedimentary breccias, conglomerates and sandstones.
(1) Lower Level: volcaniclastic sandstones and carbonated sandstones.

Kib
(2) **(b)**
Bandurrias Formation (Hauterivian- Lower Aptian)
(2) Red andesitic lavas.
(b) Lenticular interbedded of ferruginous limestones and r eddish mudstones.

Kch
(2)
Chañarcillo Group (Valangian-Aptian)
(2) Upper Level: marine fossiliferous limestone and sandstone.

JKpc
(b)
(c)
(a)
Punta del Cobre Group (Late Jurassic-Early Cretaceous)
(a) Andesitic lavas; **(b)** Tuffs and tuffaceous sandstones with interbedded carbonate; **(c)** Domes and andesitic-dacitic dikes.

Jln2
La Negra Formation (Middle-Upper Jurassic)
Massive andesitic lavas.

TPsr
Rhyolitic dykes and domes (Upper Paleocene)

TPh
(b)
Hypabyssal Intrusive (Upper Paleocene)
Pyroxene-bearing andesitic porphyry.

Kpg
(d)
Quartziferous monzodiorites, diorite and quartziferous monzonite (high Upper Cretaceous-Lower Paleocene)
(d) Pyroxene and biotite-bearing quartziferous monzodiorites.

Kglv
Granodiorite, tonalite and hornblende-bearing quartziferous diorite (low Upper Cretaceous)

Symbology

——————	Observed geologic contact
——————	Observed fault
• • • • •	Covered fault
	Normal fault; Symbol indicates sunk block
	Low angle normal fault; Symbol indicates upper block
	Thrust fault; Teeth indicates fixed block
	Syncline axial plane trace
24	Direction and dip of strata
	Dry stream or intermittent course
	Surface outline projection of Atlántida deposit.

Figure 2.0.4. Legend and symbology of the regional geology map (Figure 9).

2.2.2 Structures

A common feature of the geology of this part of northern Chile is the existence of north-south to northeast-southwest trending crustal-scale megastructures which controlled magmatism and associated hydrothermal alteration and mineralization in the last 140 Ma (Townley and Palacios, 1993, from Baker and Guilbert, 1987; Colley et al., 1989; Brown et al., 1991; Davidson and Mpodozis, 1991; Palacios et al., 1992a, b). Thus mineralization is generally restricted to four longitudinal metallogenic belts (Figure 2.5):

21

(1) along the Atacama Fault System, (2) along the Inca de Oro Belt, (3) along the West Fissure System, and (4) along the Maricunga Belt (Palacios and Townley, 1993).
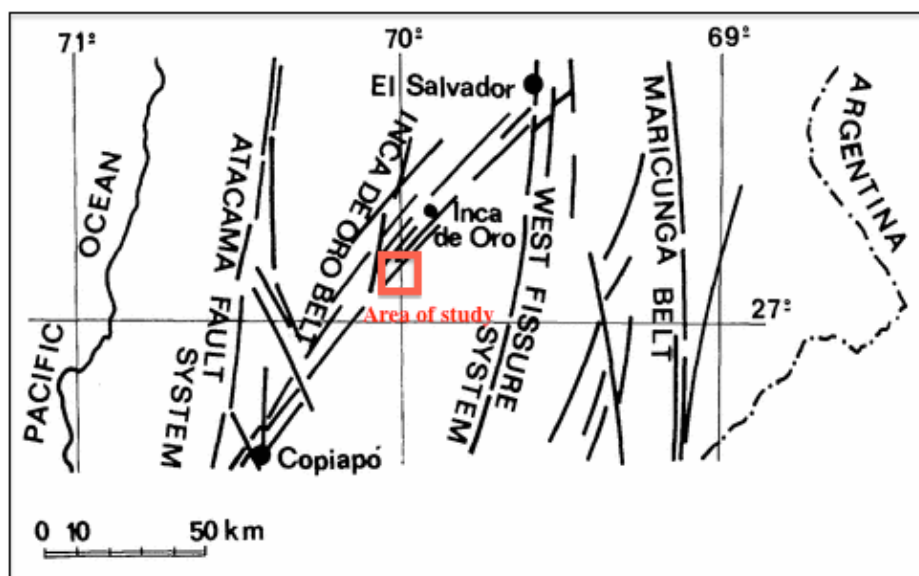
Figure 2.0.5. Distribution of megastructures and related metallogenic belts in the Copiapo-El Salvador region of northern Chile (Palacios and Townley, 1993).

The Inca de Oro fault system, of north-east tendency, is the principal megalineament of the study area and is associated with porphyry copper systems of the Upper Cretaceous. It is bounded by two main structures, to the west by the Atacama Fault System (AFS) and to the east by the Domeyko Fault System (DFS).

The AFS, of north-south tendency, is a continental-scale, trench-parallel strike-slip fault located along the Coastal Cordillera. This segmented feature of more than 1,000 km length is related to Fe-Apatite mineralized systems (e.g. Boquerón Chañar, Los Colorados) and IOCG deposits (e.g. Manto Verde, Candelaria) in Chile, whilst the DFS, a major transpressive sinistral strike-slip fault system, controls the emplacement of porphyry systems ranging from the Paleocene (e.g. Relincho) to Eocene-Oligocene (e.g. El Salvador, Potrerillos). The DFS, like the AFS, also follows an approximately north-south, trench (and arc) parallel trend.

At a more local scale, the prospect and associated ore deposits of the Upper Cretaceous porphyry belt, where Atlántida is located, may be subdivided into three sub-belts where the age of the ore-related intrusives diminishes from west to east. The westernmost sub-belt, which partially overlaps with the eastern margin of the IOCG belt (115-130 Ma), corresponds to an age range of 100-110 Ma (Chivato, Berta, Coloso, Buenaventura). These porphyries are located along the north-northeast-trending Chivato regional fault, marking the eastern edge of the IOCG belt and the western edge of the early Upper Cretaceous porphyries. The second sub-belt contains an age of

22

mineralization of around 90 Ma, including the principal known porphyry in this segment (Inca de Oro). Finally, the eastern belt would be in the Upper Cretaceous, with porphyry system ages of around 60-65 Ma (Atlántida, Chimberos), located adjacent to the Paleocene porphyry belt (Andersson, Inmet internal report).

2.2.3 Mineralization

Northern Chile, including the Copiapó area, is a Cu-rich region with a world-class provenance of porphyry copper, IOCG, and skarn deposits, closely linked to its tectonic setting characterized by a magmatic arc related to subduction of the Nazca plate under the South American plate and the change from extensional to contractional regime from the Late Cretaceous to the present.

According to Maksaev (2005), Northern Chile is characterized by large volumes of arc-related igneous rocks intruded into volcanic and volcanosedimentary rocks with limited successions of carbonate rocks. The latter were deposited mostly within shallow Jurassic and Lower Cretaceous back-arc marine basins, but also deposited as units intercalated within arc-related Lower Cretaceous volcanic successions.

Porphyry Cu-Au deposits developed as a result of focusing of the mineralizing fluids at depths of 1 – 2 km in the cooler apophyses to magmatic sources at greater depths, and so extend from intrusion host rocks into the wall rocks (Corbett, 2004). Overprinting intrusions provide multiple events of mineralization and locally recycle ore minerals into settings with higher metal grades, but may also overprint and obliterate mineralization related to earlier porphyry Cu-Au intrusions, therefore downgrading the total ore system (Corbett, 2004).

A Mid-Late Cretaceous Sub-belt extends between 26º and 31º comprising porphyry copper deposits with U-Pb ages from 108 to 88 Ma (Maksaev et al., 2006b), including Inca de Oro-Dinamarquesa-Carmen, Los Toros, Domeyko, etc. Atlántida is included within this sub-belt (Figure 2.6), with U-Pb ages of 89.8 to 90 Ma (Olson et al, 2014).
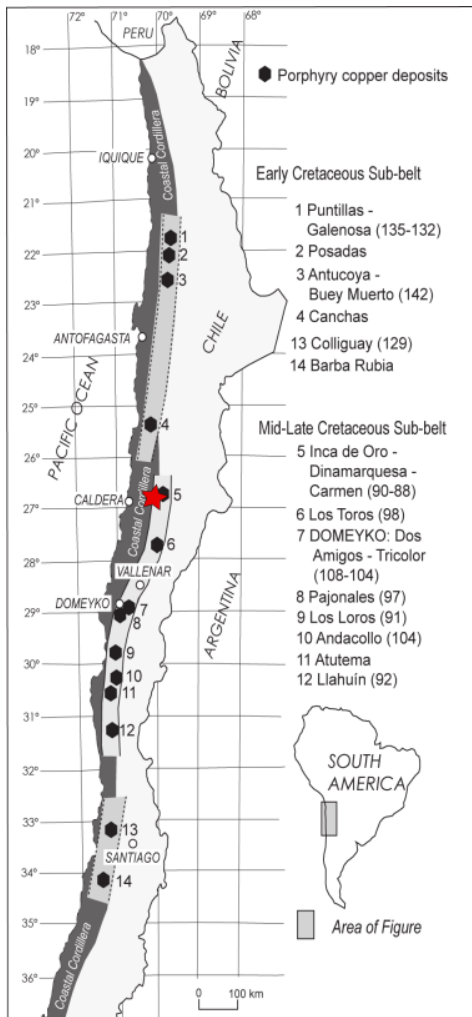
Figure 2.0.6. Cretaceous porphyry copper belt of Northern Chile. Red star represents approximate position of Atlántida project. (Modified from Maksaev, 2010).

2.3 Local Geology

The local geology of the area of study described here is the result of two sources:

1) An internal report from Inmet (2012) carried out by the geologist Steve Andersson based on detailed surface mapping of the Atlántida area and logging of 42 drill cores and,

2) Detailed logging of seven drill cores belonging to an east-west type section across the deposit (Figure 2.7), carried out by the author.

24

2.3.1 Stratified Rocks

Limestones and calcareous sandstones.

Limestones, fossiliferous limestones and folded calcareous sandstones, white to black in color. These are intruded by the Tonalite Porphyry with moderate development of calc-silicification or silicification in contact areas. Calcite veins are commonly found in the matrix of breccias in the area. These calcareous rocks are also affected by some quartz and hematite-bearing structures that provide pathways and accumulation sites for Au, Cu, Pb and Zn mineralization. Outcrops occur principally in the northern part of the project, but also appear at depth in the southern area (evidence from drillcore). This unit is assigned to the upper formation of the Chañarcillo Group.

Northern volcano-sedimentary sequence.

This sequence is located north of the tenement and includes reddish volcanoclastic sandstones, conglomerates of andesitic composition, sedimentary breccias, carbonate-bearing sandstones and interbedded fine-grained sandstones with planar stratification. These stratified sandstones commonly show desiccation cracks and ripple marks. The unit as a whole is very red, possibly due to hematitic cement (hematite pigmentation); it is also highly magnetic. These rocks are cross cut by hematite bearing barite veins with no clear trend. This unit can be assigned to the Cerrillos Formation.

Southeast volcano-sedimentary sequence.

This sequence is located southeast of the property and is composed of volcanic and volcano-sedimentary rocks of andesitic composition. Breccias and fine-grained porphyritic lavas are common, with pervasive and/or vein-hosted chlorite and epidote alteration, moderately magnetic. This unit is assigned to the Venado Formation.

Modern Sediments

They are widely distributed in the study area and correspond to alluvial and colluvial deposits composed of polymictic and monolithic gravels with clay matrices. Approximately 70% of the Atlántida area is below post-mineral cover.

2.3.2 Intrusive Units

Tonalite Porphyry

It is located immediately west of the project area, and corresponds to a hypabyssal stock of tonalitic composition, leucocratic, ranging in color from light gray to greenish gray to white. It has a porphyritic texture within which phenocrysts consist of large quartz eyes, hornblende, plagioclase, and primary biotite "books" immersed in a quartz feldspar groundmass. It is non-magnetic. This unit intrudes mainly into limestones of the Chañarcillo Group, creating silicified or calc-silicified zones of contact-altered rock. It is interpreted to be the host rock to porphyry style mineralization.

Zircon U-Pb geochronology of three samples belonging to the drill holes ATL11-06, ATL11-21 and ATL11-25 (not described in this thesis) were submitted to Oregon State University by First Quantum Minerals, Ltd. in 2014. The U-Pb isotopic determinations yielded Cretaceous ages between 89.8 ± 1.6 Ma and 90.5 ± 2.2 Ma for the Tonalite Porphyry.

Feldspar Porphyry

This lithology has a wide distribution at depth, in the central part of the project area (Figure 2.7). It is a mesocratic rock of granodioritic composition, medium to dark green in color. It displays a porphyritic texture consisting of feldspar phenocrysts, mainly as euhedral, coarse-grained crystals, and mafic phenocrysts immersed in a quartz feldspar groundmass. It is at times weakly magnetic. A common feature is a pinkish color in the matrix and as partial replacement of plagioclases, most likely caused by hematite dusting. This unit is interpreted to intrude the prior Tonalite Porphyry unit and host the mineralization.

First Quantum Minerals, Ltd. submitted four samples of the Feldspar Porphyry from the ATL12-26 drillhole to Oregon State University for Zircon U-Pb geochronology. U-Pb geochronologic analysis for these samples yielded Cretaceous ages between 90 – 92 Ma.

Andesitic Dykes

Light to dark green porphyrytic dykes with andesitic compositions that intrude the above lithologies in all drill cores, up to 20 m in thickness. They are comprised mainly of white plagioclase phenocrysts immersed in a green aphanitic groundmass. The andesitic dykes are post-mineral, and barren.
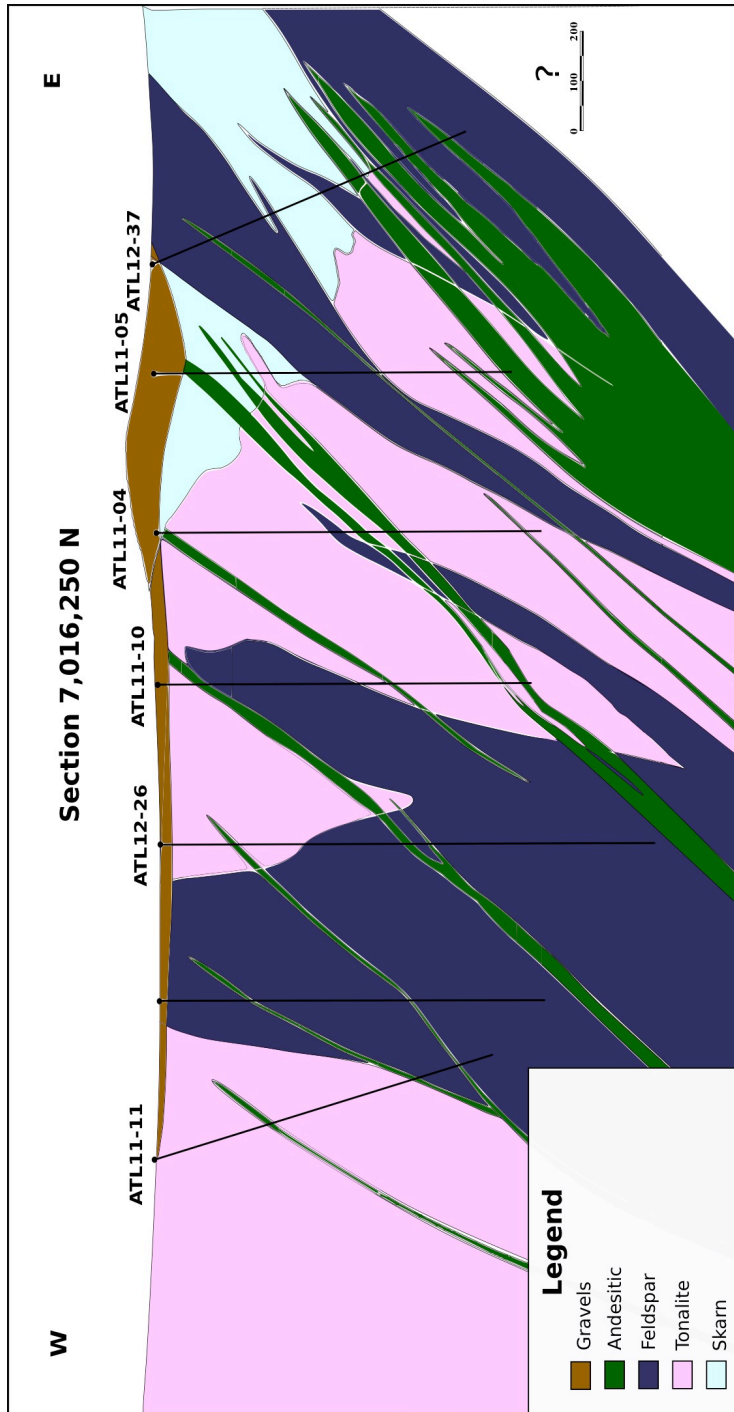
Figure 2.0.7. Lithology of the Atlántida type section.

28

2.3.3 Structures

The following structural features were described by Andersson (2012, Inmet internal report). The Atlántida project is mainly covered by gravels and therefore historic structural interpretation was carried out mainly using Landsat Enhanced Thematic Mapper (ETM) imagery, Digital Elevation Model (DEM) data and terrestrial magnetometry, supplemented with data from surface mapping.

The structural setting is dominated by northwest and northeast trending lineaments (Figure 2.8), which define distinct structurally constrained domains. These faults may have controlled the intrusive and hydrothermal activity related to mineralization. The main structural feature is a major northeast trending lineament (a geological discontinuity referred to as the Falla Valle or Valley Fault), which separates the domain of carbonate rocks in the northwest from the volcanic domain in the southeast, the latter being displaced downward with respect to the northeast block.
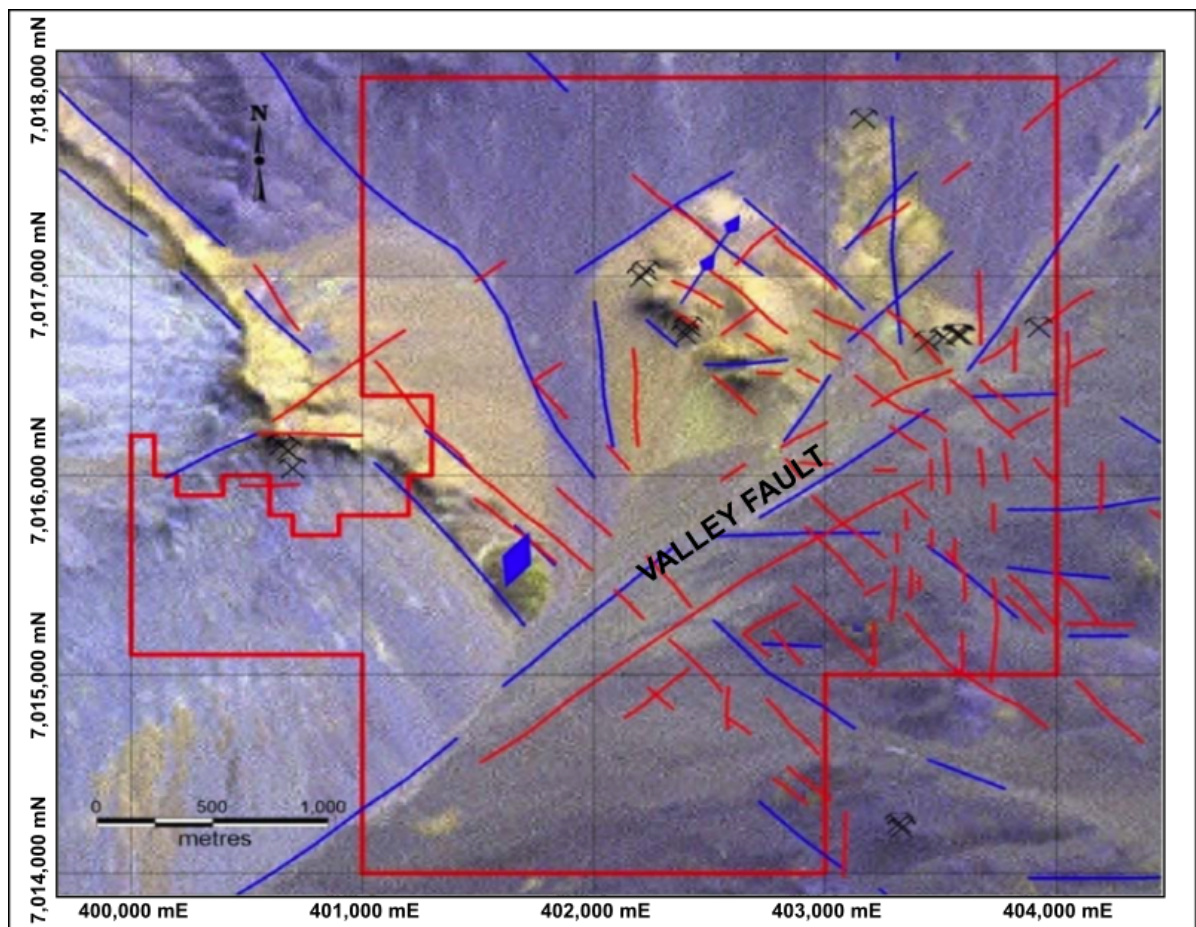
Figure 2.0.8. Local structural setting of Atlántida (Andersson, 2012).

2.3.4 Hydrothermal Alteration

The description of the hydrothermal alteration is based on core logging of a type section, detailed petrographic studies, geochemical data of the cores, and on Andersson, 2012 (Inmet internal report). At the deposit scale, five styles of alteration are recognized (Figure 2.8):
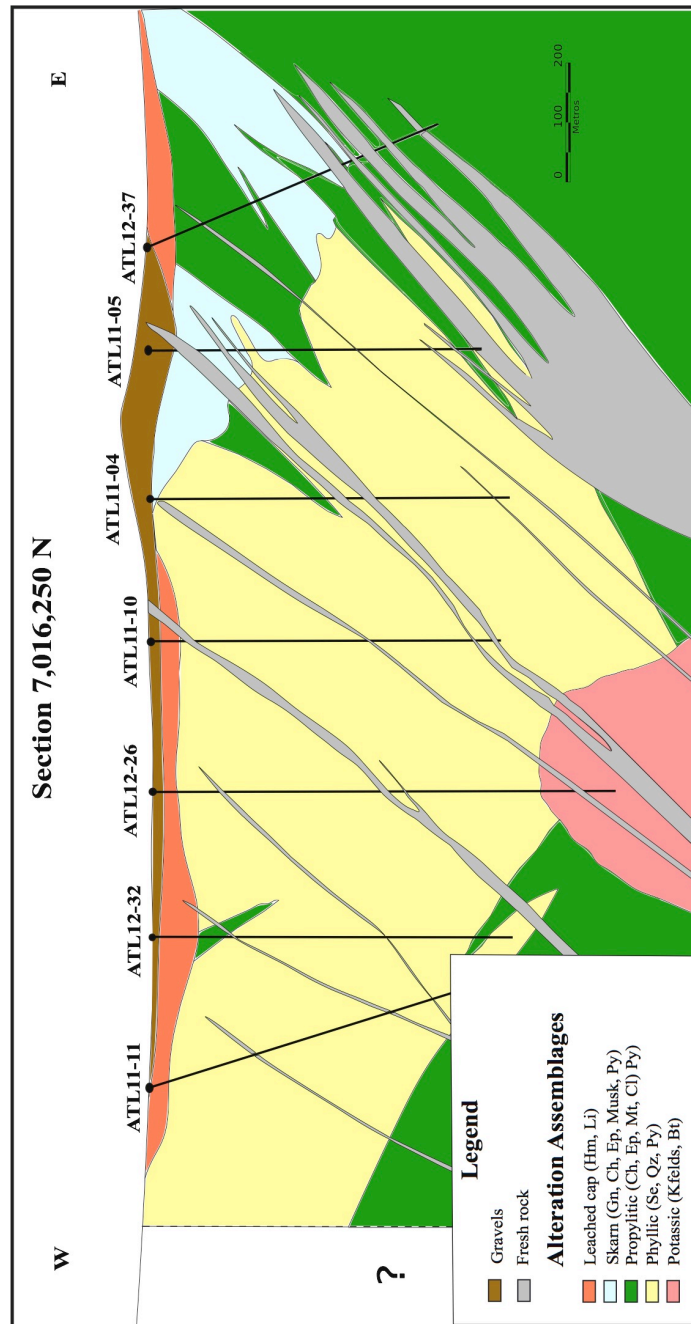
Figure 2.0.9. Diagram showing the Atlántida alteration in the type section (this thesis).

Calc-silicification (Skarn)

Carbonate-bearing rocks, including limestones, calcareous sandstones and calcilutites are affected by silicification and moderate calc-silicification along the contact areas with intrusives. Evidenced by mineral assemblages dominated by garnet, chlorite, epidote, mushketovite and pyrite mineralization. Moving away from the contact zone, the rocks are relatively fresh. At surface, areas with skarn alteration, some with garnet, are recognizable.

Potassic Alteration

Particularly recognizable as a continuous, 130 m intercept in drillhole ATL12-26 of the type section (Figure 2.8). Potassic alteration is observed as a pinkish to salmon color obliterating the rock (K-feldspar pervasive alteration). K-feldspar veins intergrown with quartz to create a graphic texture are also observed, perhaps a variation of aplite veining. This zone is also characterized by the presence of quartz A veins, indicating high temperature and proximal (and typically potassic) location with regard to the hydrothermal core.

Propylitic Alteration

Characterized by a typical mineral assemblage of chlorite-epidote-calcite-magnetite, propylitic alteration occurs locally in contact with the zone of potassic alteration in the centre of the system and peripherally in the outer margins of the Feldspar Porphyry, at the east side of the type section, beyond the zone of phyllic alteration (Figure 2.8). Chlorite strongly to moderately replaces mafics and locally replaces plagioclase phenocrysts. Secondary epidote appears mainly as weak replacement of plagioclase feldspar and less commonly as weak replacement of mafic minerals in the Feldspar Porphyry. Calcite is most commonly present as thin veinlets of millimeter-scale.

Phyllic Alteration

Phyllic alteration is the dominant alteration style in the type section (Figure 2.8). It is located in the centre of the system, above the potassic core, overprinting the earlier propylitic alteration. It consists of chlorite-sericite and quartz-sericite assemblages, affecting both the Tonalite Porphyry and the Feldspar Porphyry (Figures 2.7 and 2.8). The chlorite-sericite alteration occurs selectively replacing feldspars and mafic minerals,

while intense quartz-sericite alteration is associated mainly with selvages in D veins and less commonly as a pervasive feature in the rocks.

Supergene Alteration

Supergene alteration is weakly developed in Atlántida deposit. Oxidation extends down to 100 meters depth (Figure 2.8) and it is characterized by the presence of limonites (e.g. jarosite, goethite), hematite and supergene clays.

Based on the alteration and its distribution, described above, a fairly typical porphyry system zonation (Figure 2.9) is interpreted.
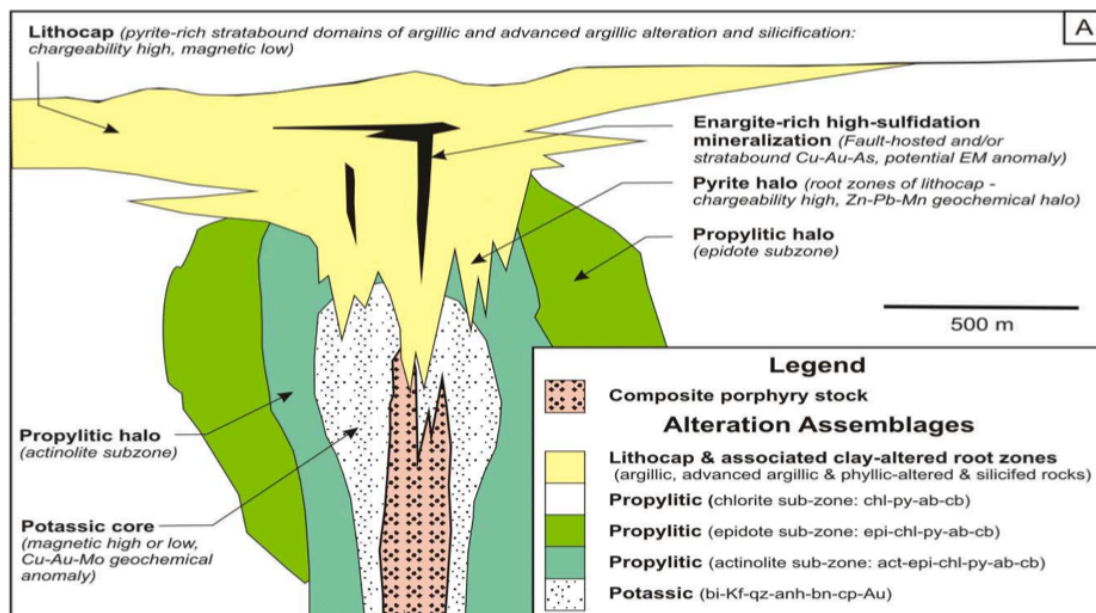
Figure 2.0.10. Schematic alteration zoning and overprinting relationships in a calc.alkalic porphyry system (Holliday and Cooke, 2007). In the case of Atlántida, no advanced argillic alteration is observed, and phyllic-type assemblages are common above the potassic zone (in this schematic, phyllic alteration is included in the yellow area above the core and grouped with argillic alteration type).

2.3.5 Mineralization

Supergene Mineralization

Some leaching is observed in the upper portions (up to 100 m) of drillholes (e.g. ATL11-11, ATL12-32, ATL12-26 and ATL11-10 of the type section) but no significant supergene mineralization has accumulated in conjunction with these leaching processes. Cu-Au-Mo mineralization is almost entirely hypogene.

Copper

Copper (as chalcopyrite) is present in the Feldspar Porphyry, Tonalite Porphyry and skarn. Copper mineralization is associated with pyrite, mainly restricted to D veins of millimeter to decimeter scale. The highest grades can be found above the potassic zone, in the phyllic zone of the Feldspar Porphyry and in lesser grades in the Tonalite Porphyry surrounding the Feldspar Porphyry. Chalcopyrite mineralization is also present in the skarn where it is restricted to patches in massive pyrite and less commonly related to calcite veins, showing overall grades between 0.1% and 2%.

The Atlántida porphyry does not contain a bornite zone of copper mineralization, a common feature in many other porphyry copper deposits.

Gold

Gold mineralization is predominantly present in the phyllic alteration zones of the Feldspar Porphyry and in the brecciate parts of the Tonalite Porphyry. It is also important in the skarn.

Molybdenum

Most of the molybdenum mineralization at Atlántida is hosted in quartz veins and vein halos. The mineralization is restricted to some drill cores and is not widely found.

Other

Gold, copper, lead, and zinc mineralization is at times linked to structures containing crystalline, dogtooth-textured quartz veins, crustiform and/or brecciated, and can be interpreted as being related to sub-epithermal environments adjacent to a lateral or central porphyry system. These features can be observed as far as 3 km from the property.

Chapter 3

Sampling and Analysis procedures

The present chapter briefly describes the sampling process, treatment, and chemical analysis of samples.

3.1 Gas Sampling Procedure

Also known as the OreHoun® collector, it is a passive gas sampling collector containing a sachet of a highly pure activated carbon (MERCK©), which is a highly absorbent material. The collectors used in this study contain about 20 g of activated carbon held within a cloth bag. This bag is placed inside a cardboard tube, which is inside another cloth bag (Figure 3.1). The final device is kept in a sealed plastic bag prior to use to prevent contamination. The method is seasonally dependent, as exposure to water (e.g., rainfall) may 'reset' the carbon by washing out accumulated ions. Therefore the most apt time for implementation of these collectors is a prolonged dry period, particularly conductive to application in arid to hyperarid Atacama Desert of northern Chile.

For the installation of collectors a hole about 40 cm in depth is dug (Figure 3.2, A). The sampler must record relevant data from the hole, including humidity, color and fractures, before removing the collector from the plastic bag and placing it into the hole with the mesh facing upward (Figure 3.2, B). The collector is then covered with rocks and finally covered with soil removed during the initial digging (Figure 3.2, C and D).

After 90 to 120 days the sampling medium equilibrates with the gaseous composition of the underlying environment and the collectors may be removed. For this purpose, once the collector is recovered from the hole, the sampler must take out the outer cloth bag and the cardboard tube, and keep the inner cloth bag (containing the activated carbon). The cloth bag containing the activated carbon is then placed in a plastic bag, making

sure that the plastic bag is squeezed out and contains a minimum of ambient air when sealed.

In this study, the OreHound® installation was carried out during November 3rd to 7th 2014 by the author and FQM[7] field teams. A total of 234 activated carbon collectors (including QAQC) were installed over the Atlántida deposit and its surroundings on a 500 m spaced staggered grid (see Figure 5.1), buried at 30 to 40 cm depth. When retrieved after 90 days, during February 4th to 8th, all collectors were in excellent condition. No rainfall occurred during the exposure time of the collectors. The activated carbon was analyzed by ICP-MS in two laboratories: 1) for 50 elements at Andes Analytical Assay, in Santiago Chile and, 2) for 53 elements at ALS Chemex in Vancouver, Canada.
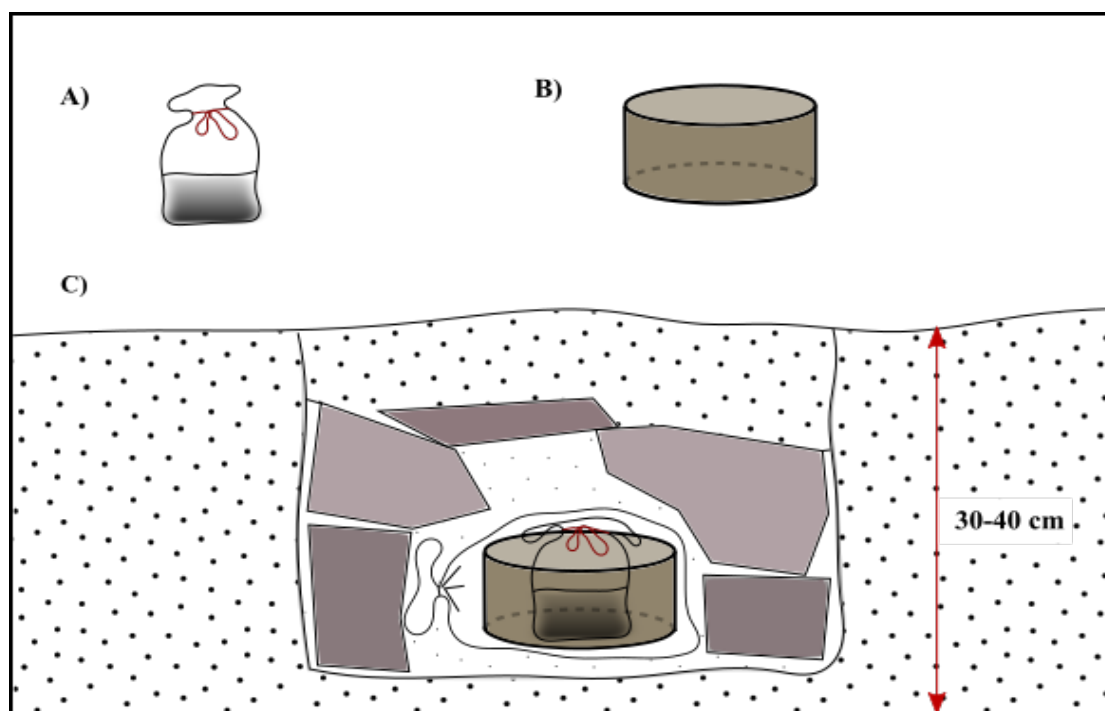
Figure 3.0.1. Cartoon showing: A) sachet (cloth bag) containing approximately 20 [gr] of activated carbon, B) cardboard tube and, C) diagram showing the spatial disposition of a type collector within the hole in the ground. Modified from López (2014, p. 33).

---

[7] FQM: First Quantum Minerals (company).
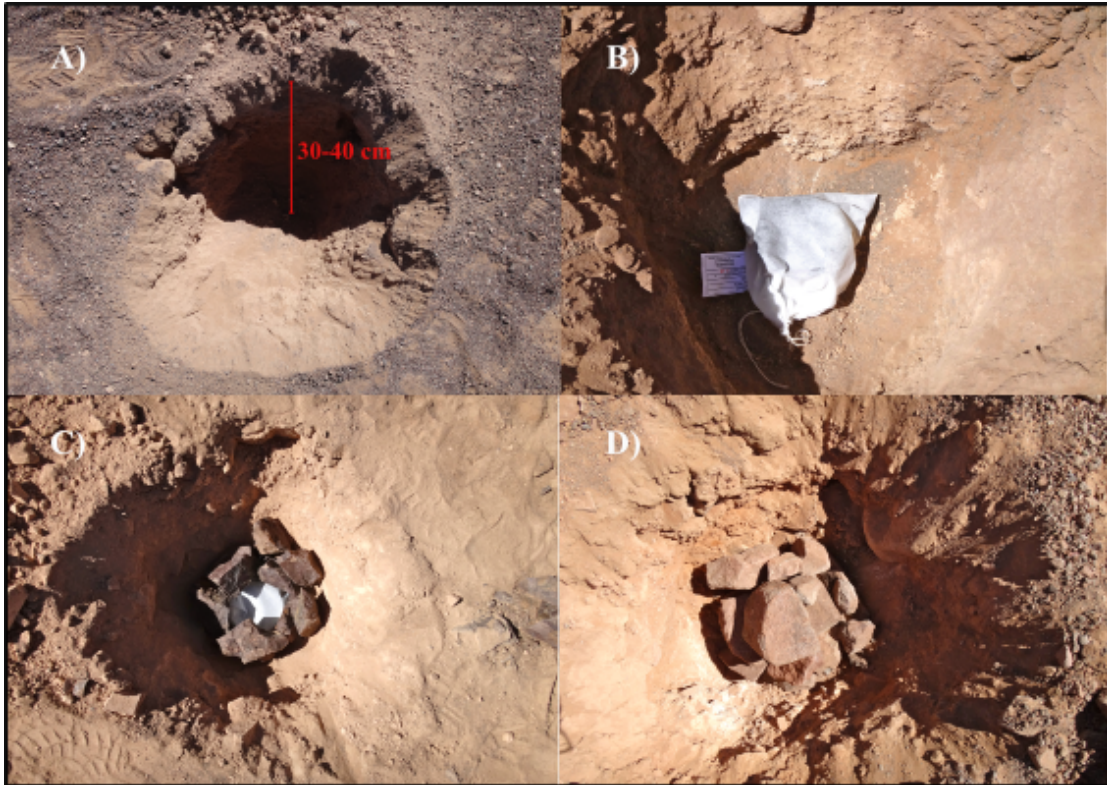
Figure 3.0.2. Picture taken during the field campaign. A) hole of 30 to 40 cm depth, B) collector placed in the hole, C and D) rocks placed to protect the collector before covering it with the removed soil.

3.2 Analytical Techniques

The activated carbon was first treated and analyzed by Andes Analytical Assay (AAA) laboratory. The elution methodology used by this lab consisted of attacking 5 g of activated carbon with 150 mL of ultrapure nitric acid in three progressive aliquots of 50 mL. The resulting solution is then heated to concentrate metals through evaporation. This process causes a decrease in volume of the solution. This procedure achieves a nearly 100% elution of adsorbed metals.

After the above process is complete, the result is a 10 ml solution. This final solution is diluted three times with distilled water until reaching 100 ml. This final solution is then analyzed by ICP-MS (inductively coupled mass spectrometry) and ICP-OES (inductively coupled atomic emission spectrometry) in AAA laboratory (item code: ICP_N50_MS_OP01).

Table 3.1. Detection limits of activated carbon analysis by ICP_N50_MS_OP01 in Andes Analytical Assay laboratory.

Element	Range [ppm]	Element	Range [ppm]	Element	Range [ppm]	Element	Range [ppm]
Ag	0.01 - 40	Dy	0.002 - 40	Na	20 - 5,000	Sr	0.2 - 100
Al	20 - 10,000	Er	0.002 - 40	Nd	0.002 - 40	Tb	0.002 - 40
As	0.02 - 1,000	Eu	0.002 - 40	Ni	0.02 - 1,000	Te	0.005 - 100
Au	0.1 - 100 [ppb]	Fe	20 - 15,000	P	2 - 1,000	Ti	1 - 10,000
B	2 - 1,000	Gd	0.002 - 40	Pb	0.2 - 1,000	Tl	0.005 - 100
Ba	0.2 - 1,000	Hg	0.002 - 100	Pr	0.002 - 40	Tm	0.002 - 40
Bi	0.01 - 100	Ho	0.002 - 40	S	20 - 10,000	V	0.05 - 1,000
Ca	20 - 15,000	K	20 - 10,000	Sb	0.01 - 1,000	Y	0.002 - 400
Cd	0.01 - 1,000	La	0.01 - 100	Sc	0.002 - 400	Yb	0.002 - 40
Ce	0.002 - 40	Lu	0.002 - 40	Se	0.05 - 100	Zn	0.1 - 1,000
Co	0.01 - 1,000	Mg	20 - 15,000	Si	10 - 10,000	Zr	0.05 - 200
Cr	0.02 - 1,000	Mn	0.2 - 1,000	Sm	0.002 - 40		
Cu	0.1 - 1,000	Mo	0.05 - 1,000	Sn	0.01 - 100		

Although the intention of this method is to achieve 100% dissolution of the activated carbon, a notable drawback is the multi-step process which involves excessive handling and re-introduction of liquids (nitric acid and distilled water), leading to a higher probability of contamination and/or trace level shift problem between batches. During the Atlántida work, a distinct level-shift issue appeared in results derived from this process involving several elements (Figure 17). As such, the results obtained by this analysis were discarded for any further study. Such level shift problem had occurred previously (Castillo et al., 2015). The analytical procedure confirmed not to be adequate for the purpose desired. Despite that such problems may be dealt with by means of statistical processing and data correction (Castillo et al., 2015), such requirement is by far ideal.
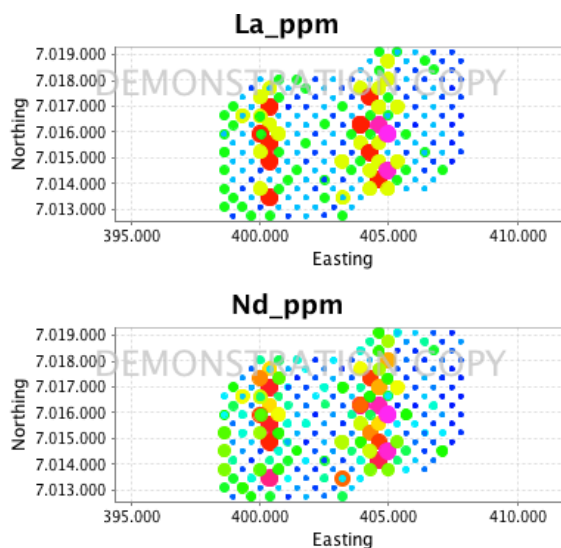
Figure 3.0.3. Two elements representing the massive level shift problem obtained with the nitric acid elution method of AAA laboratory.

As the results of analysis carried out at AAA laboratory were discarded, a fully new batch of samples was sent to ALS Chemex for ME-MS41L analysis technique. This technique involves an aqua regia digestion followed by multielement ICP-MS and ICP-OES analysis, optimized to minimize lower limits of detection for all included elements.

Lesser handling and introduction of foreign liquids results in the elimination of the batch level shift problems found in AAA laboratory results and produced reliable, internally consistent data, apt for interpretation. PART OF THE CONCLUSION MAYBE?

Table 3.2. Detection limits of activated carbon analysis by super trace aqua regia by ICP-MS.

Element	Detection Limit [ppm]	Element	Detection Limit [ppm]	Element	Detection Limit [ppm]	Element	Detection Limit [ppm]
Au	0.0002	Cu	0.01	Nb	0.002	Ta	0.005
Ag	0.001	Fe	0.001 [pct]	Ni	0.04	Te	0.01
Al	0.01 [pct]	Ga	0.004	P	0.001 [pct]	Th	0.002
As	0.01	Ge	0.005	Pb	0.005	Ti	0.001 [pct]
B	10	Hf	0.002	Pd	0.001	Tl	0.002
Ba	0.5	Hg	0.004	Pt	0.002	U	0.005
Be	0.01	In	0.005	Rb	0.005	V	0.1
Bi	0.001	K	0.01 [pct]	Re	0.001	W	0.001
Ca	0.01 [pct]	La	0.002	S	0.01 [pct]	Y	0.003
Cd	0.001	Li	0.1	Sb	0.005	Zn	0.1
Ce	0.003	Mg	0.01 [pct]	Sc	0.005	Zr	0.01
Co	0.001	Mn	0.1	Se	0.1		
Cr	0.01	Mo	0.01	Sn	0.01		
Cs	0.005	Na	0.001 [pct]	Sr	0.01		

Chapter 4

Quality Control and Exploratory Data Analysis

In order to identify the source of errors, establish the level of confidence and assess the limitations of analytical data, the results of the analyses are subjected to quality control.

Precision is the measure of reproducibility of a measurement, while accuracy is how close a measured value is to a known or accepted value (Piercey, 2014). The measurement of precision is done using reference materials (standards) and duplicates. Accuracy is measured using standards. Finally, contamination is tested through the analysis of blanks.

4.1 Quality Control

4.1.1 Lower Limit of Detection and Limit of Quantification

The lower limit of detection (LOD) or detection limit (DL) is an indicator of the minimum detectable analyte net signal, amount, or concentration that can be detected with a specifically defined level of confidence using a given method of analysis. The limit of quantification (LOQ) is the concentration above the background where the result is considered quantifiable and trusted (Piercey, 2014), at approximately 3.3 times the DL.

Based on the above definitions, this thesis considers results to be uncertain unless they are greater than 3 times the DL, above which they are then considered reliable. If more than 50% of samples do not comply with this rule for a given element, it is not considered for further statistical analysis.

For the remaining elements (those considered reliable), values below the DL were set to half [8] the DL value for the element in question to allow the use of the sample for further statistical analyses.

The reason for the elimination of the elements with these characteristics is that the variance of these elements is zero or near zero, not providing information and moreover, their presence hinders further multivariate analysis.

4.1.2 Coefficient of Variation

The coefficient of variation (%CV) or relative standard deviation (RSD) is a way to describe the variation of a test and expresses the standard deviation as a percentage of the mean, and is calculated as follows:

$$CV_i(\%) = \frac{s_i}{\mu_i} \cdot 100 \qquad (1)$$

Where $CV_i(\%)$ is the percent coefficient of variation for element i; s_i is the standard deviation of the series of analytical runs for element i; and μ_i is the mean value of the element i over a series of analytical runs (Piercey, 2014).

The coefficient of variation is an estimation of the relative error (Stanley and Lawie, 2007). Since standard deviation typically increases as the concentration of the analyte increases, the CV can be regarded as a statistical equalizer (qcnet website).

For the analysis of standard replicates (standard measurements), the %CV of a given element is obtained for every standard analyzed and then the average %CV (%CV_avg) is calculated.

4.1.3 Average Coefficient of Variation

The relative error of the field and analytical duplicates are calculated using the average coefficient of variation:

---

[8] There are other approaches for the handling of data values below detection limit, such as eliminating the specific data value or the data point itself. In this thesis, such approaches are not used since it is expected to have data values below DL for some elements and deletion of either only the specific value will lead to missing data which results in issues when applying statistical analysis, while deletion of the whole data point results in a reduction of relevant information.

$$CV_{avg}(\%) = \sqrt{\sum_{i=1}^{n} \frac{CV_i^2}{n}}$$ (2)

Where n is the number of duplicate pairs and CV_i is the coefficient of variation of the i pair "original-duplicate" or the coefficient of variation of a given standard.

For the analysis of duplicate samples, the average coefficient of variation method is the best and most robust method of measuring precision as it is independent of the nature of the distribution of errors and is equally applicable to elements that exhibit or do not exhibit the nugget effect (Piercey, 2014). There is no exact value which indicates whether or not the precision is good as it depends on the analysis, so before judging a CV, a look to the mean has to be taken, as at very low concentrations the CV may be high and vice versa.

In this thesis an average coefficient of variation lower than 10% is considered good while one between 10% and 20% is considered acceptable and will be judged depending on the mean. A %CV_{avg} greater than 20% is bad and the respective variables will be discarded.

4.1.4 Analytical Error

The analytical error (E_A) is useful to assess laboratory assay quality and is estimated by:

$$E_A = \sqrt{\frac{CV_{Dup}^2 + CV_{St}^2}{2}}$$

Where CV_{Dup} is the average CV of the lab duplicates and CV_{St} is the average CV of the lab standards.

In this thesis, values of the analytical errors lower than 10% is considered analytically reliable, values between 10% and 20% must be studied according to the total error and finally, variables with analytical errors greater than 20% are considered here as not precise and the variable in question is eliminated.

4.1.5 Total Error

The total error (E_T) corresponds to the field relative error and is calculated using the field duplicates (and the respective original samples) as they represent the total error adhered during sampling and laboratory analysis. The expression that represents the total error is the same used in *(2)*.

In this thesis, variables with total error greater than 30% will be eliminated, while variables with total error values between 0 and 30% will be evaluated together with scatterplots of the duplicates.

4.1.6 Sampling Error

The sampling error is calculated from:

$$E_s = \sqrt{E_T^2 - E_A^2}$$

Where E_T is the total error and E_A is the analytical error.

4.1.7 Scatterplot - Precision

Also called 'precision scatterplot', this diagram plots the original data on the X axis (independent variable) while the duplicate data is plot on the Y axis (dependent variable).

Precision scatterplots were performed in Excel, with control lines that represent a given level of precision. In this thesis, 20% precision was chosen.

The interpretation is by checking if the samples lie within the defined precision lines and seeing the geometric distribution of them. According to Piercey (2014), the geometric distribution of the samples provides insight into the nature of imprecision and also provides a means of monitoring the source of error. In fact, if all samples lie within the control lines the element in question is said to be precise. On the contrary, if most of the samples randomly lie outside the control lines, the element is said to be imprecise for that level of precision. Finally, an element has moderate precision when some of the samples lie outside the control lines.

4.1.8 Relative Difference Method - Accuracy

Percent relative difference (%RD) allows us to calculate accuracy. It is calculated from the replicate analyses of the standards using (Piercey, 2014):

$$\%RD = \frac{\mu_i - STD_i}{STD_i} \cdot 100$$

Where μ_i is the mean value of element *i* in the standard over a number of analytical runs; and STD_i is the 'known' or 'certified' value of element *i* in the standard or reference material.

According to Piercey (2014), in general %RD values of ± 0 – 3% are considered to have excellent accuracy, values between 3 – 7% are considered to have very good accuracy, values between 7 – 10% have good accuracy and values above 10% are not accurate (Jenner, 1996).

4.1.9 Contamination

Contamination is tested through blanks[9] by means of Shewart control charts. Control chart plots the time (or sequence number) on the X axis and the value measured in the Y axis (Scogings et al., 2014). According to Piercey (2014), the mean and standard deviation (SD) of the blank is calculated from the set of values resulted from the analyses and when doing so it is critical to not include the outliers in the dataset.

In control charts, acceptable values that the blank can take are those falling within the range [mean±2SD]. A blank value beyond the mean blank value plus 2 or 3 standard deviations of the mean might be due to potential contamination or product of an error.

4.2 Exploratory Data Analysis

4.2.1 Distribution

In order to understand the approximate distribution of the data, performance of histograms and Q-Q plots is done, since according to Reimann and Filzmoser (1999) these graphical tools give a good first impression of the data distribution.

---

[9] Blank is a material that contains nil to extremely low concentrations of the element(s) of interest (Piercey, 2014).

In particular, in order to test for normality distribution density trace of the data, density trace of a normally distributed data and marginal boxplots is plotted in the histograms, while normal control lines are plotted in conjunction with the Q-Q plots, allowing a graphical idea of the sample distribution. A normal distribution should approximate a symmetrical bell in a histogram, the median should be placed in the center of a boxplot and data points should approximate a straight line in a Q-Q plot. A log-normal distribution have the same features listed above but the plots are made with the log-transformed data values.

Also, the statistical Shapiro-Will test is used to test whether a single univariate data set differs significantly from a normal distribution. This test is chosen since it works even for a small sample size.

The null hypothesis of Shapiro-Will test is that the samples are taken from a normal distribution. So if the p-value is less than 0.05, the null hypothesis that the samples come from a normal distribution is rejected.

4.2.2 Background and outliers

The following procedures are aimed at the estimation of threshold values to define outliers and the range to establish the background data.

Outliers describe the abnormal data behavior, i.e. data that deviates from the natural data variability (Filzmoser, 2006). Hampel et al. (1986) and Barnett and Levis (1994) statistically defined outliers as "values belonging to a different population because they originate from another process or source, i.e. they derived from (a) contaminating distribution(s)" (Reimann et al, 2005). Detection is important since they can localize anomalisms that can either be an error or an indicator for mineral deposits.

Traditionally, the sample mean, variance and standard deviation give good estimations for data location and data shape, if they are not contaminated with outliers (Ben-Gal, 2005). When the database is contaminated, those parameters may deviate and significantly affect the outlier-detection performance (Ben-Gal, 2005). As the geochemical data set is likely to have outliers, just robust methods (methods not influenced by the presence of outliers) are used in this thesis in the search for outliers. Additionally, as geochemical data rarely follow a normal distribution (Reimann and Filzmoser, 2000), methods used in this thesis are nonparametric, i.e., methods that do not make any assumptions about the data distribution (Reimann and Filzmoser, 1999). In fact, geochemical data may have skewed distribution, i.e., its distribution may be asymmetric (one tail longer than the other).

Therefore, instead of the mean and standard deviation the median[10] and the median absolute deviation from the median (MAD[11]) are used respectively. The MAD is a measure of dispersion, highly robust to skewed distribution and to a high number of outliers. Furthermore for the use of median and MAD, the data do not need to follow any particular model (Reimann and Filzmoser, 1999).

4.1.9.1 Background and univariate outliers

Threshold[12] values for statistical outlier detection and range of background in one variable at the time are determined by a mixture of statistical tools like boxplots, 'median±2MAD' procedure and visual inspection of normal probability plots (equivalent to cumulative probability plot).

As suggested by Reimann et al. (2005), the first step performed here is the study of the empirical distribution of the data. To do so, visual inspection for slope changes and breaks in cumulative probability plots (CDF diagrams) aim to find multiple populations or isolated outliers and consequently establish a possible threshold and range.

The second step was to estimate the threshold and range through boxplot of the elements. Note that boxplot uses quartiles to differentiate between background and anomalous values (Figure 4.1), thus their output is resistant to the presence of outliers. Furthermore, their use is not seriously influenced by widely different data distributions (Hoaglin et al., 2000, from Reimann et al, 2005). In fact, the first and third quartiles, Q1 and Q3 respectively, are used to obtain the robust measures for the mean $\mu=(Q1+Q3)/2$ and the standard deviation $\sigma=Q3-Q1$. An outlier is any value that lies more than one and half times the length of the box from either end of the box (Figure 4.1), while the background is estimated as the concentration between the boxplot inner fences. Mild outliers are defined as any concentration or values lying within the inner and outer fences and extreme outliers are those concentrations lying outside the outer fence (Figure 4.1 and Table 4.1).

---

[10] Median: middle or 50th percentile value.
[11] MAD: Median of the set comprising the absolute values of the differences between the median and each data point.
[12] Threshold: Limit beyond which any data point is considered an outlier.
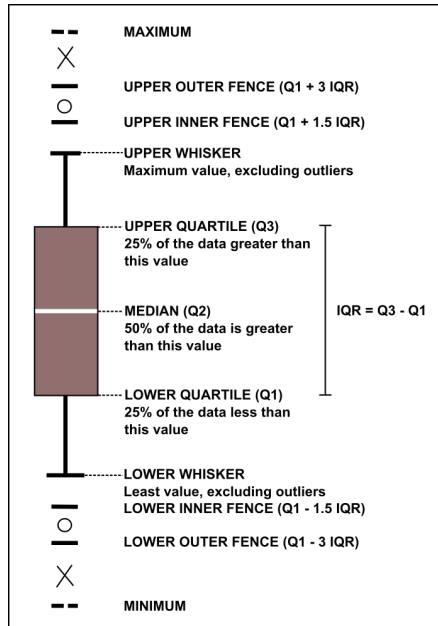
Figure 4.0.1. Schematic representation of boxplot (Tukey Plot).

Third, another common procedure is to mark as a potential outlier any point that is more than two standard deviations from the mean. Here the two MADs from the median or 'median±2MAD' procedure is used instead (for the reasons explained in 4.2.2) to estimate the threshold for outlier detection and the background range. The background are the concentration between the median±2MAD range (Table 4.1).

Table 4.1. Background range and outlier thresholds determined by two methods: boxplot (Tukey Plot) and 'median±2MAD'.

Class	Concentration boxplot	Concentration_[median±2MAD]	
Extreme negative anomaly	< Q1 – 3*IQR	< median – 2*MAD	*(symmetrical dist.)*
Mild negative anomaly	[Q1 – 3*IQR, Q1 – 1.5*IQR [	< median – 2*left MAD	*(asymmetrical dist.)*
Background	[Q1 – 1.5*IQR, Q1 + 1.5*IQR]	[median – 2*MAD, median + 2*MAD]	
Mild positive anomaly	] Q1 + 1.5*IQR, Q1 + 3*IQR]	> median + 2*MAD	*(symmetrical dist)*
Extreme positive anomaly	> Q1 + 3*IQR	> median + 2*right MAD	*(asymmetrical dist.)*

Finally, the data is grouped into classes as shown in Table 3. Geochemical data is also represented spatially in maps plotting the defined classes as different symbols with size proportional to the element concentration.

4.1.9.2 Multivariate outliers

According to Dol and Verhoog (2010), multivariate analysis is important to find outliers that cannot be found in a univariate approach. Supporting this idea, Ben-Gal (2005) mentioned that in many cases multivariate observations cannot be detected as outliers

when each variable is considered independently, and suggested that outlier detection is possible only when multivariate analysis is performed, and the interactions among different variables are compared within the class of data.

The methodology to assess multivariate outlier detection first begins with a simple approach through visual inspection of 2D scatterplots.

Second, statistical methods are used, most of which use robust and classic Mahalanobis distance to detect if a sample (collector) is far from the centre of the data distribution. Mahalanobis distance accounts for the different scale and variance of each of the variables in a set in a probabilistic way (Starkweather, 2013). Samples with large Mahalanobis distance are indicated as outliers. The theory of Mahalanobis distance assumes that the data is multivariate normally distributed (d dimensions) and Mahalanobis distance of samples follows a Chi-Square distribution with d degrees of freedom. In the robust Mahalanobis distance, mean and covariance matrix are estimated robustly.

*In order to distinguish between extremes of a distribution and outliers, Garret (1989) introduced the χ^2 – plot, which draws the empirical distribution function of the robust Mahalanobis distance against the χ^2 distribution. A break in the tail of the distributions is an indication for outliers, and values beyond this break are iteratively deleted. This is a really good plot for outlier detection in more than two dimensions.

Also here, the 'Adjusted Quantile plot' ('aq.plot' function in R) is used for outlier. Depends on distance between the cumulative distribution function (cdf) of Chi-Square and empirical cumulative distribution function (ecdf) of samples in tails. It simulates 'normal' deviations in the tails, so outliers have 'abnormally large' deviations in the tails.

Finally, the function 'pcout' in R was used. It is based on robust principal components.

The 'Chi-squared plot' plots the ordered robust Mahalanobis distances of the data against the quantiles of the Chi-squared distribution and the outliers are detected visually (Filzmoser and Gschwandtner, 2015).

The 'Moutlier' function in R used here plot the Mahalanobis distance against a variable. The robust distance is based on the minimum covariance determinant (MCD).

Q-Q plot is also a good tool used here for outlier detection, since this tool has no distributional assumption.

Now, in this thesis is considered that an isolated outlier is probably product of error whereas a group of outliers can belong to a population different from the main one. To clarify which is the case of the outliers previously found by boxplots is that these were plotted in conjunction with scatterplots.

Chapter 5

OreHound Results

5.1 Introduction

The OreHound gas collectors were utilized over Atlántida, in a grid of 9.5 km by 6.5 km comprising a total of 234 collectors (at times referred to as "samples" in this document). All samples were chemically analyzed by ICP-MS for 53 elements via ALS Chemex's ME-MS41L technique as described previously (see Chapter 3).

The 234 collectors included 14 field duplicates, 12 field blanks and 208 original collectors. In this project, no internal standard material was submitted. Analytical control management by the laboratory comprises analyses of 4 four international standards, seven blanks and seven analytical duplicates. The raw data can be found in Appendix A.1.

Figure 5.1 shows the location and extent of the program.

Figure 5.0.1. Sample locations at Atlántida are shown relative to the surface projection of the known extent of mineralization (hashed area). Area sampled is approximately 9.5 km by 6.5 km.
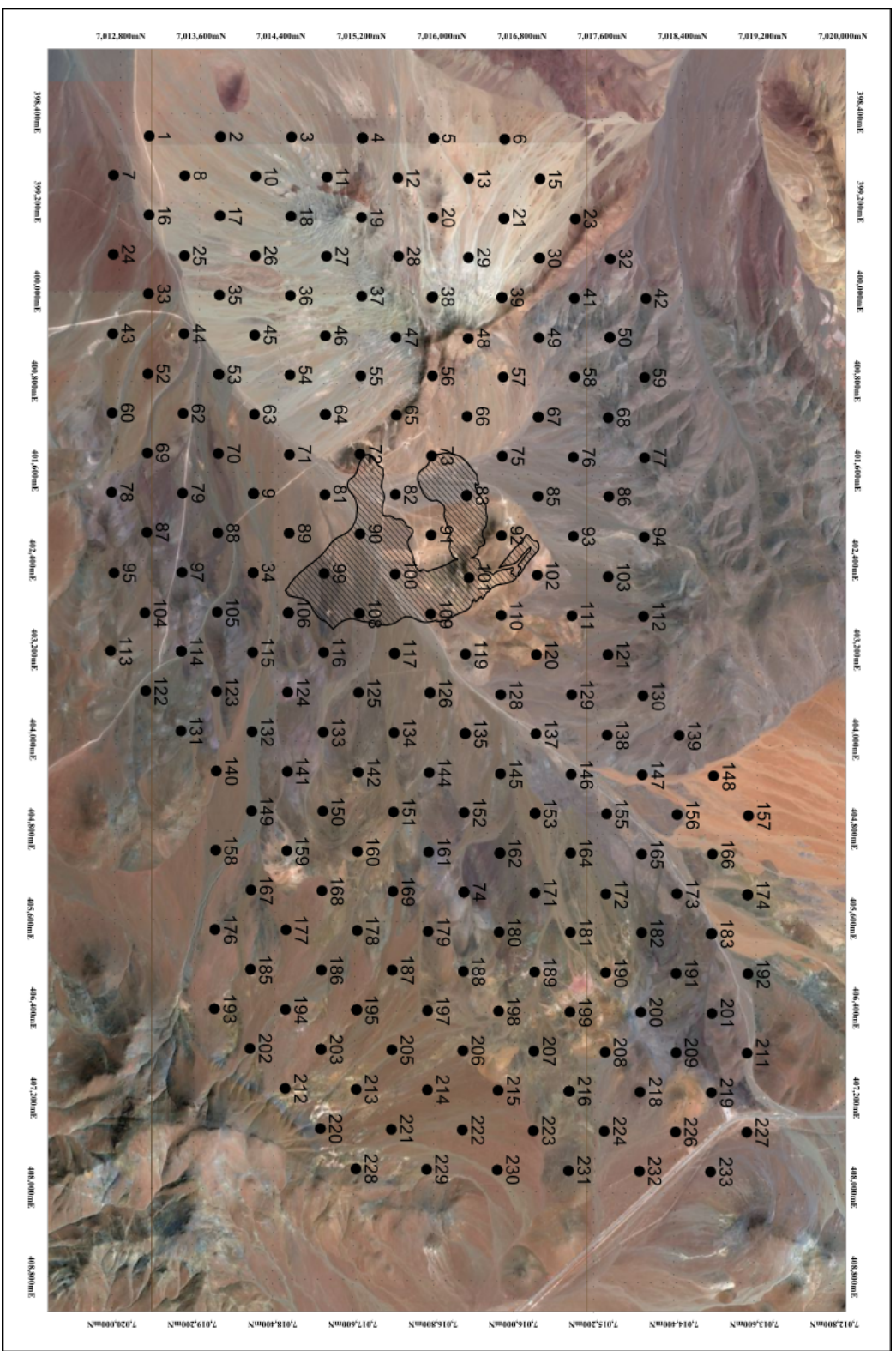
5.2 Quality Control

Precision was evaluated using analytical and field duplicates and standards by applying precision scatterplots and the average coefficient of variation. Accuracy was tested using standard material by calculating their percent relative difference and by using Shewart control charts[13]. Contamination was tested using laboratory and field blanks also by the use of control charts.

4.1.10 Detection Limits

A first inspection was done by looking at the values of the 234 samples analyzed by 53 elements. Contents below the detection limit for all samples were obtained for B, Pt, Re, S, Ta and Tl, while a total of 13 elements yielded values with more than 50% of the samples below detection limits: Au, B, Be, Cd, Hg, In, Pd, Pt, Re, S, Ta, Te and Tl.

Table 5.1. Percentage of samples below detection limit (%BDL) and below three times the detection limit (%3BLD). In red: elements with %BDL greater than 50%, in blue: element with constant value.

Elem.	% BDL	% 3BDL	Elem.	% BDL	% 3BDL	Elem.	% BDL	% 3BDL
Au	98.7	100.0	Hf	20.9	100.0	S	100.0	
Ag	0.0	0.0	Hg	95.7	100.0	Sb	15.8	96.6
Al	0.0	100.0	In	71.4	100.0	Sc	12.4	54.3
As	0.0	0.0	K	0.0	100.0	Se	49.1	100.0
B	100.0		La	0.0	0.0	Sn	0.0	67.9
Ba	0.0	0.0	Li	0.0	100.0	Sr	0.0	0.0
Be	91.9	100.0	Mg	4.3	100.0	Ta	100.0	
Bi	19.7	98.7	Mn	0.0	0.0	Te	67.5	100.0
Ca	0.0	82.9	Mo	0.0	97.4	Th	0.0	0.0
Cd	55.6	96.6	Na	0.0	0.4	Ti	0.0	100.0
Ce	0.0	0.0	Nb	3.8	96.6	Tl	100.0	
Co	0.0	0.0	Ni	0.0	0.0	U	2.1	99.6
Cr	0.0	0.0	P	0.0	0.0	V	0.0	97.0
Cs	0.0	46.2	Pb	0.0	0.0	W	0.0	0.4
Cu	0.0	0.0	Pd	94.4	100.0	Y	0.0	0.0
Fe	0.0	0.0	Pt	100.0		Zn	0.0	0.0
Ga	0.0	0.0	Rb	0.0	0.0	Zr	0.0	3.4
Ge	11.1	50.9	Re	100.0				

Additionally, the element Ti is discarded for taking a constant value (see raw data in Appendix A), in other words, for having zero variance.

---

[13] Shewart control charts plot the values relative to time or sequence, so that the value measured is plotted on the Y axis and time (or sequence number) is plotted on the X axis (Scogings et al, 2014).

Furthermore, 16 elements have 50% or more samples with values equal or lower than three times the lower limit of detection (below the 'limit of quantification'). These elements are: Al, Bi, Ca, Ge, Hf, K, Li, Mg, Mo, Nb, Sb, Sc, Se, Sn, U and V, and since they are not 100% trusted, they need to be studied carefully.

In essence, all elements with the majority of results below the DL, or elements with constant values are eliminated and not used for further analysis of any kind. See Table 4 for a list of the 14 elements discarded.

4.1.11 Precision

Precision is tested using standards (or reference materials) inserted by the laboratory and using duplicate analysis. In total seven laboratory duplicates, 14 field duplicates and 14 measurements in four standards (GBM908-10, MRGeo08, OREAS 90 and OREAS-45b) are used.

Precision test is carried out on the remaining 39 valid elements by means of visual inspection of field and laboratory duplicates by 'precision scatterplots'. These show the position of the original-duplicate data related to control lines representing 20% of precision (Appendix B.3). Analysis of scatterplots indicate that four (As, Cs, W and Y) of the 39 elements have a considerable amount of samples outside the control lines in either field or lab scatterplots and so do not comply within a 20% maximum precision error (Appendix B.3.3).

With the standards, precision is calculated using the coefficient of variation and its average. Regarding the field and lab duplicates, precision is calculated with the %CV, the average coefficient of variation (%CV$_{avg}$) and with scatterplots (see Chapter 4 for more details). The analytical and field %CV of every original-duplicate pair and the %CV of every standard run analysis for a given element can be found in Appendix B.3 and B.1 respectively. The %CV$_{avg}$ of analytical duplicates and standards, as well as the analytical, sampling and total errors are listed in Table 5.3 for the 39 elements.

The %CV$_{avg}$ or error of the standards resulted in values lower than 10% for all the 39 elements. Additionally, %CV$_{avg}$ of analytical duplicates is lower than 10% for Al, Ba, Ca, Cu, Fe, K, La, Li, Mg, Mn, P, Pb, Rb, Sr and U, between 10-20% for Ag, Ce, Cr, Ga, Na, Ni, Th, V, W, Y and Zn, and finally slightly exceeding the 20% acceptable limit for As, Cs, Se and Zr which are judged within the acceptable analytical and total error.

The elements Bi, Co, Ge, Hf, Mo, Nb, Sb, Sc and Sn have a %CV$_{avg}$ of laboratory duplicates higher than 30% and an analytical error higher than 20% and thus these nine elements are discarded by far exceed the permitted error limit. Besides that, most of the

elements measured have an analytical error lower than 10%, while elements As, Cr, Cs, Ga, Na, Se, Th, V, Zn and Zr have an analytical error between 10-20% and so were studied regarding the total error.

With respect to the total error, all the remaining elements excepting As and Se have an error lower than 30%. Arsenic and selenium are thus discarded for having a total error greater than the 30% permitted.

Finally, based on 'precision scatterplots', Cs is imprecise (even though doesn´t have resolution problems), so it is also discarded for any further analysis.

In summary, based on precision control and errors, out of 39 elements, 12 have been discarded from further analysis. Moreover, even though the 27 remaining elements (Ag, Al, Ba, Ca, Ce, Cr, Cu, Fe, Ga, K, La, Li, Mg, Mn, Na, Ni, P, Pb, Rb, Sr, Th, U, V, W, Y, Zn and Zr) are reliable, take note that concentrations for Al, Ca, K, Li, Mg, U and V are lower than the limit of quantification and so they: 1) have little variance, 2) have poor resolution issues and, 3) are not 100% trusted, that's why these seven elements will be consider for further analysis but not for further statistical analysis.

4.1.12 Accuracy

Accuracy was estimated through the analysis of international standard using the relative difference method (%RD, see Chapter 4) and Shewart control charts (Appendix B.1).

Shewart control charts showed excellent accuracy for the standards GBM908-10 and OREAS 90, as well as for the standard OREAS-45b for which only two elements (Au and Cd) fall outside acceptable variance limits.

The standard MRGeo08 presented several elements with samples outside the variance limit. Al, Ca, Cs, Fe, In, K, Li, Mn, Na, Re, Sr and Y have usually one of the three data points outside the accepted maximum variance. Moreover, some of these elements show a trend towards data that have gradually higher or lower concentrations, representing a clear bias.

As this problem only occurred for one out of four international standard samples, results for this particular standard MRGeo08 are discarded.

4.1.13 Blanks and contamination

The laboratory inserts seven blanks. From their analysis, most of the 53 elements yield concentrations below the DL while the remaining yield concentrations close to DL, evidencing no contamination during the analysis.

Regarding the field blanks and because all collectors contain the same activated carbon, the element concentration should be about the same and follow a normal distribution. Based on the Shapiro-Wilk test for normality, all the elements (Ag, Ba, Ce, Cu, Fe, La, Mn, P, Pb, Rb, Sr, Th, Y and Zn) but Cr, Ga, Na, Ni, W and Y are normally distributed (Appendix B.2.X incluir), although Q-Q plot rather shows that Cr, Ga and Na do approximate to a normal distribution but with the presence of one outlier (Appendix B.2.1).

Additionally, the elements Ba, Cr, Ga, Na, Ni, Pb and W all present statistical outliers beyond the $Q_1 \pm 1.5 \cdot IQR$[14] as evidenced by boxplots (Appendix B.2.1 incluir) as well as by Q-Q plots (Appendix B.2.1). The remaining elements have no outliers, which is the ideal situation.

Considering the non-normality and presence of outlier concentrations for some elements, Shewart control charts used to check for the presence of contamination or abnormalities in the blanks are prepared according to the condition of each element. In fact, visual inspection of Shewart control charts of field blanks (see Appendix B.2.2) indicate that the field blanks for elements Ag, Ce, Cu, Fe, P, Sr, Th, Y lie perfectly between the range [median – 2MAD, median + 2MAD] and that La, Mn, Rb and Zr lie within the range [mean* – 2SD*, mean* + 2SD*]. Cr and Zn have one sample value lying outside the range [mean* – 2SD*, mean + 2SD*], Ba, Ga, Na and W have two samples laying out of that range and Ni and Pb with three samples out of range. Moreover, Ba has two sample values lying outside 3 standard deviations of the mean (and outside 3 MAD of the median), Cr, Ga, Na, W has one sample value lying outside 3 standard deviations of the mean (and also outside 3 MAD from the median), Ni and Pb has the three outliers outside 3 standard deviations of the mean (as well as 3 MAD from the median). So care must be taken with the elements Ba, Cr, Ga, Na, Ni, Pb, W and Zn. Table 5.2 summarizes that mentioned above.

---

[14] IQR: interquartil range, or IQR=Q_3 – Q_1. See Figure 4.1.

Table 5.2. Shewart control chart summary. The total number of field blank samples is 12. The (*) means that the standard deviation (SD) and mean of the blanks are calculated without the outliers detected by boxplots and Q-Q plots.

Element	Within the median±2MAD	Within the mean*±2SD*	Nº of samples outside the mean*±2SD*
Ag	✓		
Al			
Ba	✗	✗	2
Ca			
Ce	✓		
Cr	✗	✗	1
Cu	✓		
Fe	✓		
Ga	✗	✗	2
K			
La	✗	✓	
Li			
Mg			
Mn	✗	✓	
Na	✗	✗	2
Ni	✗	✗	3
P	✓		
Pb	✗	✗	3
Rb	✗	✓	
Sr	✓		
Th	✓		
U			
V			
W	✗	✗	2
Y	✓		
Zn	✗	✗	1
Zr	✗	✓	

4.1.14 QAQC Summary

Firstly, 13 (Au, B, Be, Cd, Hg, In, Pd, Pt, Re, S, Ta, Te, Tl) out of 53 chemical elements are discarded for having most of their values below the detection limit. Ti is also discarded since it does not provide information (constant value for all samples).

Second, regarding 'precision scatterplot' graphs, which plot original measurements vs their field and laboratory duplicates, as other mean to inspect precision, they show that at a 20% precision level the elements As, Bi, Cs, Hf, Mo, Nb, Sb, Sc and Sn are imprecise. The remaining elements have moderate to good precision evidenced by both laboratory and field duplicates graphs.

In reference to the coefficient of variation and errors, the elements As, Bi, Co, Ge, Hf, Mo, Nb, Sb, Sc, Se and Sn yield either laboratory duplicates %CV, analytical and/or total errors above the acceptable limits.

For the reasons above mentioned, the elements discarded are 12. Although not discarded, the elements Na, Pb and W have a high total error (or %CV of field duplicates) but between the respective acceptable limits.

From the blanks, it is concluded that all laboratory blanks yield concentration below or near DL, evidencing no contamination. On the other hand, field blanks analysis yield some values lying outside the acceptable limits (either [mean±2SD] or [median±2MAD]) for the elements Ba, Cr, Ga, Na, Ni, Pb, W and Zn, evidencing a sort of contamination in those elements.
Regarding the analysis of the international standards, introduced by the laboratory, to test accuracy, most of the elements are precise but some bias is introduced during the analysis or lack proper calibration as evidenced by the standard MRGeo08 (Appendix B.1), but in general terms the analyses are accurate as evidenced by three out of four international standards.

Table 5.3. QAQC summary results.

Element	%CV$_{avg}$ (Analytical)	%CV$_{avg}$ (Standard)	Analytical Error	Total Error	Sampling Error	Pass	Reason
Ag	10.439	3.737	7.840	11.688	8.668	Yes	Highly precise
Al	0.000	2.072	1.465	0.000	not applicable	Yes	Highly precise
As	**20.704**	3.158	14.809	**36.619**	**33.491**	No	Imprecise and high total and sampling errors
Ba	4.100	1.984	3.221	17.353	17.051	Yes	Highly precise
Bi	**40.825**	3.889	**28.998**	**48.928**	**39.409**	No	High errors and imprecise
Ca	0.000	2.181	1.542	17.417	17.348	Yes	Errors within the limits
Ce	10.212	3.535	7.641	16.358	14.463	Yes	Precise with errors within the limits
Co	**30.166**	4.136	**21.530**	**21.391**	not applicable	No	Analytical error out of limit
Cr	18.275	2.954	13.090	10.606	not applicable	Yes	Precise with errors within the limits
Cs	**23.639**	4.108	16.966	**27.378**	**21.487**	No	Imprecise and high errors
Cu	3.165	1.724	2.548	3.537	2.453	Yes	Highly precise
Fe	5.878	2.799	4.604	9.174	7.935	Yes	Precise
Ga	17.715	2.690	12.670	10.401	not applicable	Yes	Moderate precision
Ge	**67.889**	9.393	**48.462**	**42.305**	not applicable	No	High errors
Hf	**39.242**	3.424	**27.853**	**43.480**	**33.387**	No	High errors and bad resolution
K	0.000	2.585	1.828	**25.198**	**25.131**	Yes	Precise although high sampling error and bad resolution
La	8.833	3.038	6.605	19.834	18.702	Yes	Moderate precision but analytical error close to limit
Li	0.000	4.050	2.864	0.000	not applicable	Yes	Precise
Mg	0.000	3.241	2.292	12.599	12.389	Yes	Precise
Mn	2.994	1.863	2.494	14.091	13.869	Yes	Precise
Mo	**37.268**	5.423	**26.630**	**32.660**	18.908	No*	Imprecise due to bad resolution and high errors
Na	15.224	9.436	12.665	**22.678**	18.812	Yes	Low precision and bad resolution
Nb	**36.025**	3.156	**25.571**	**35.477**	**24.591**	No	High errors and imprecise due to bad resolution
Ni	13.846	2.788	9.987	8.115	not applicable	Yes	Moderate precision
P	4.749	2.332	3.741	8.152	7.243	Yes	Precise
Pb	8.539	4.042	6.680	**26.206**	**25.340**	Yes	Moderate precision but high sampling error
Rb	5.469	5.448	5.458	17.577	16.707	Yes	Moderate precision
Sb	**35.504**	6.283	**25.495**	**49.614**	**42.563**	No	High errors and imprecise
Sc	**85.503**	5.168	**60.570**	**57.959**	not applicable	No	High errors and imprecise
Se	**23.570**	7.492	17.488	**37.796**	**33.507**	No*	High total and sampling error and bad resolution
Sn	**33.265**	5.066	**23.793**	**49.482**	**43.386**	No	High errors and imprecise due to bad resolution
Sr	5.514	4.851	5.193	6.212	3.410	Yes	Highly precise
Th	15.346	5.439	11.512	13.268	6.597	Yes	Poor precision due to bad resolution, although errors are between limits
U	9.879	2.595	7.222	12.718	10.468	Yes	Poor precision due to bad resolution, although errors are between limits
V	17.379	3.917	12.597	16.054	9.952	Yes	Poor precision due to bad resolution, although errors are between limits
W	10.341	7.813	9.165	**25.782**	**24.098**	Yes	Moderate precision due to poor resolution. High sampling error
Y	10.748	5.282	8.468	16.718	14.414	Yes	Moderate precision due to poor resolution
Zn	15.246	2.849	10.967	16.919	12.883	Yes	Moderate precision due to poor resolution
Zr	**20.678**	4.395	14.948	16.186	6.209	Yes	Moderate precision due to poor resolution

5.3 Exploratory Data Analysis

The OreHound gas collector data set composed of 208 samples (not including QAQC samples) and the 20 reliable elements were subjected to an exploratory data analysis in order to examine the distribution of elements, and to identify outliers and populations that will allow for robust interpretation of the geochemical data.

5.3.1 Basic statistics: all samples

Table 5.4 summarizes the basic statistics for the 208 samples and includes the following parameters calculated on a arithmetic base: minimum (min) and maximum (max) values, 5, 10, 25, 50 (median), 75, 90, 95 and 98th percentiles, mean, standard deviation (SD) and median absolute deviation (MAD).

Table 5.4. Basic statistics for 27 elements composed of 208 samples each. Minimum (Min) and maximum (Max) values, 5, 10, 25, 50, 75, 90, 95 and 98th percentiles, mean, standard deviation (SD), left and right median absolute deviation (MAD).

Elem. [ppm]	DL	Min	Percentiles									Max	Mean	SD	Left MAD	Right MAD
			5th	10th	25th	50th	75th	90th	95th	98th					
Ag	0.001	0.02	0.022	0.024	0.025	0.028	0.03	0.032	0.032	0.035	0.037	0.028	0.003	0.003	0.002
Ba	0.5	2.7	3.44	5.47	6.175	6.8	7.5	8.83	9.165	9.572	14.2	6.819	1.505	0.55	0.6
Ce	0.003	0.111	0.115	0.122	0.13	0.14	0.154	0.176	0.188	0.204	0.303	0.146	0.025	0.01	0.013
Cr	0.01	0.41	0.444	0.457	0.488	0.52	0.58	0.673	0.839	1.056	1.66	0.562	0.147	0.03	0.05
Cu	0.01	2.47	2.734	2.787	2.89	3.005	3.133	3.273	3.317	3.514	3.98	3.026	0.212	0.115	0.13
Fe	10	50	60	60	60	70	70	80	90	118.6	350	70.673	24.168	10	0
Ga	0.004	0.015	0.025	0.028	0.031	0.034	0.038	0.041	0.043	0.048	0.058	0.035	0.006	0.003	0.003
La	0.002	0.053	0.062	0.066	0.073	0.078	0.086	0.096	0.101	0.109	0.167	0.080	0.014	0.005	0.007
Mn	0.1	6.2	8.035	9.1	9.6	10.6	12	13.93	14.465	15.086	18.6	10.98	1.97	1	1.4
Na	10	10	40	50	60	70	90	110	120	130	150	76.25	22.72	10	10
Ni	0.04	0.31	0.334	0.35	0.36	0.39	0.44	0.503	0.619	0.834	1.45	0.424	0.124	0.03	0.04
P	10	80	90	90	100	110	120	130	130	140	150	108.5	13.99	10	0
Pb	0.005	0.343	0.500	0.924	1.034	1.175	1.411	1.637	1.761	2.122	2.65	1.218	0.348	0.14	0.205
Rb	0.005	0.431	0.520	0.542	0.612	0.704	0.792	0.947	0.995	1.037	1.08	0.721	0.146	0.092	0.090
Sr	0.01	1.34	1.524	1.56	1.68	1.79	1.94	2.08	2.153	2.227	2.35	1.81	0.194	0.11	0.14
Th	0.002	0.01	0.011	0.012	0.013	0.014	0.016	0.018	0.02	0.024	0.069	0.015	0.005	0.001	0.001
W	0.001	0.003	0.005	0.005	0.006	0.007	0.008	0.009	0.01	0.011	0.024	0.007	0.002	0.001	0.001
Y	0.003	0.016	0.021	0.024	0.027	0.031	0.036	0.041	0.045	0.054	0.084	0.033	0.009	0.004	0.004
Zn	0.1	1.7	1.8	1.9	2	2.2	2.5	2.6	2.9	3.2	13	2.325	0.813	0.2	0.2
Zr	0.01	0.03	0.04	0.04	0.04	0.05	0.06	0.07	0.076	0.08	0.1	0.053	0.012	0	0
Al [%] *	0.01	0.01	0.01	0.01	0.01	0.01	0.01	0.01	0.01	0.01	0.02	0.01	0.001		
Ca [%] *	0.01	0.02	0.02	0.02	0.03	0.03	0.03	0.04	0.04	0.04	0.04	0.029	0.007		
K [%] *	0.01	0.01	0.01	0.01	0.01	0.02	0.02	0.02	0.02	0.02	0.03	0.017	0.005		
Li *	0.1	0.1	0.1	0.1	0.1	0.1	0.1	0.1	0.1	0.1	0.2	0.101	0.012		
Mg [%] *	0.01	0.005	0.01	0.01	0.01	0.01	0.01	0.01	0.01	0.01	0.01	0.01	0.001		
U *	0.005	0.0025	0.005	0.005	0.006	0.006	0.007	0.008	0.009	0.009	0.042	0.007	0.003		
V *	0.1	0.2	0.2	0.2	0.2	0.3	0.3	0.3	0.3	0.4	1.9	0.266	0.128		

5.3.2 Basic statistics: Field blanks

Table 5.5 summarizes the basic statistics for the 12 field blank samples and includes the following parameters calculated on a arithmetic base: minimum (min) and maximum (max) values, 5, 10, 25, 50 (median), 75, 90, 95 and 98th percentiles, mean, standard deviation (SD) and median absolute deviation (MAD). Elements normally distributed (or close) have a single MAD, while elements with skewed distribution have two MAD, a left and a right MAD (See 4.).

Table 5.5. Basic statistics of 12 blank samples for 20 elements. Minimum (Min) and maximum (Max) values, 5, 25, 50, 75 and 95th percentiles, mean, standard deviation (SD) and median absolute deviation (MAD) for each element. Some elements have two MAD because their distribution is not symmetric.

Element [ppm]	DL	Min	Percentiles 5th	25th	50th	75th	95th	Max	Mean	SD	Var	Left MAD	Right MAD
Ag	0.001	0.025	0.026	0.027	0.029	0.03	0.031	0.032	0.029	0.002	4.42E-06		0.0022
Ba	0.5	3	3.11	5.75	6.55	6.9	8.36	8.8	6.208	1.697	2.8790		1.0378
Ce	0.003	0.119	0.120	0.129	0.142	0.148	0.155	0.162	0.138	0.013	1.7.E-04		0.0126
Cr	0.01	0.48	0.486	0.5	0.535	0.57	0.712	0.8	0.558	0.090	0.0081	0.035	0.045
Cu	0.01	2.87	2.876	2.978	3.165	3.258	3.471	3.52	3.149	0.216	0.0466		0.2817
Fe	10	0.005	0.005	0.006	0.007	0.007	0.008	0.008	0.007	0.001	9.92E-07		0.0015
Ga	0.004	0.019	0.023	0.032	0.036	0.037	0.039	0.039	0.034	0.006	3.49E-05	0.003	0.001
La	0.002	0.062	0.063	0.072	0.082	0.085	0.091	0.096	0.079	0.011	1.E-04		0.0067
Mn	0.1	7.4	7.4	10.1	11.1	12.1	13.815	14.2	10.908	2.106	4.4336		1.6309
Na	10	0.006	0.006	0.006	0.007	0.008	0.011	0.013	0.008	0.002	4.24E-06	0.001	0.001
Ni	0.04	0.37	0.37	0.418	0.43	0.433	0.509	0.58	0.432	0.053	0.0028	0.01	0
P	10	0.008	0.009	0.01	0.011	0.012	0.013	0.013	0.011	0.002	2.27E-06		0.0015
Pb	0.005	0.36	0.374	1.019	1.13	1.331	1.899	2.41	1.160	0.528	0.2789		0.2150
Rb	0.005	0.466	0.506	0.674	0.718	0.875	1.019	1.095	0.755	0.177	0.0313		0.1394
Sr	0.01	1.58	1.657	1.788	1.86	1.995	2.047	2.08	1.869	0.145	0.0209		0.1557
Th	0.002	0.011	0.012	0.013	0.014	0.015	0.017	0.018	0.014	0.002	4.52E-06		0.0022
W	0.001	0.004	0.004	0.006	0.006	0.007	0.013	0.016	0.007	0.003	1.14E-05	0	0
Y	0.003	0.022	0.022	0.024	0.029	0.036	0.038	0.039	0.030	0.006	4.16E-05		0.0096
Zn	0.1	1.8	1.965	2.2	2.35	2.6	2.87	3.2	2.383	0.349	0.1215	0	0.2965
Zr	0.01	0.04	0.04	0.04	0.04	0.05	0.07	0.07	0.047	0.012	0.0001	0	
Al [%]*	0.01	0.01	0.01	0.01	0.01	0.01	0.01	0.01	0.010	0.000	6.E-20		0
Ca [%]*	0.01	0.02	0.02	0.03	0.03	0.03	0.04	0.04	0.030	0.006	4.E-05		
K [%]*	0.01	0.01	0.01	0.018	0.02	0.02	0.02	0.02	0.018	0.005	2.E-05		
Li*	0.1	0.1	0.1	0.1	0.1	0.1	0.1	0.1	0.100	0.000	5.E-18		
Mg [%]*	0.01	0.005	0.008	0.01	0.01	0.01	0.01	0.01	0.010	0.001	2.E-06		
U*	0.005	0.1	0.1	0.1	0.1	0.1	0.1	0.1	0.100	0.000	5.E-18	0	
V*	0.1	0.005	0.008	0.01	0.01	0.01	0.01	0.01	0.010	0.001	2.E-06		

61

5.3.3 Distribution

Table 5.4 shows that median values are not so different from means, but the values of the standard deviation are notably different from MAD values in some elements, illustrating that at least some elements are not normally distributed. Histograms and normal-probability plots of the 20 variables are available in Appendix C.1.

A more objective approach, offered by Shapiro Wilk[15] (S-W) and Kolmogorov Smirnov (K-S) statistical tests, is used in order to test for univariate normality. Table 1 of Appendix C.2 shows the p-values of S-W and K-S tests applied to the original and the log-transformed data set. K-S test results are only referential owing to the reasons explained in section 4.4.

According to Shapiro Wilk, all the elements have p-values lower than 0.05, in other words, none of the elements have arithmetic-normal distribution, Sr being the closest element to a arithmetic-normal distribution. However, the p-value of the log transformed data gives a p-value greater than 0.05 for Sr, meaning that strontium distributes log-normally. Additionally, according to the K-S test, the elements Ag, Cu, Ga, Mn, Rb and Sr have arithmetic-normal distribution, while Ce, La and Y have lognormal distribution.

Given this scenario, Q-Q plot and the 2D scatterplot (Appendix C.1 and C.3) are used with the aim to define different populations in the data.

5.3.4 Background and univariate outliers

Outlier thresholds as well as the number of mild[16] and extreme[17] outliers estimated by boxplots are listed in Table 5.7 (boxplot are displayed marginal to histograms in Appendix C.1).

Similarly, outlier thresholds as well as the number of outliers estimated by the 'median±2MAD' procedure are provided in Table 5.8.

---

[15] Shapiro-Wilk and Kolmogorov-Smirnoff statistical tests are different possibilities for testing for univariate normality (and hence, log-normality) of the data. See Appendix X.

[16] Mild outliers are data points beyond 1.5 times the interquartil range from either end of the box (Q1 – 1.5*IQR or Q3 + 1.5*IQR), that is not an extreme outlier.

[17] Extreme outliers are data point beyond 3 times the interquartil range from either end of the box (Q1 – 3*IQR or Q3 + 3*IQR).

Table 5.6. Number of anomalies (outliers) identify by boxplot (Tukey Plots) in 20 elements and respective thresholds. LOF: lower outer fence, LIF: lower inner fence, UIF: upper inner fence, UOF: upper outer fence, LEA: lower extreme anomalies, LMA: lower mild anomalies, UMA: upper mild anomalies, UEA: upper extreme anomalies.

Element	LOF	LIF	UIF	UOF	Nº anomalous samples			
					LEA	LMA	UMA	UEA
Ag	0.01	0.0175	0.0375	0.045	0	0	0	0
Ba	2.2	4.1875	9.4875	11.475	0	12	4	1
Ce	0.058	0.094	0.19	0.226	0	0	3	4
Cr	0.212	0.35	0.718	0.856	0	0	10	10
Cu	2.1625	2.52625	3.49625	3.86	0	4	4	1
Fe	30	45	85	100	0	0	7	7
Ga	0.01	0.0205	0.0485	0.059	0	2	4	0
La	0.033	0.052875	0.105875	0.12575	0	0	5	3
Mn	2.4	6	15.6	19.2	0	0	1	0
Na	-30	15	135	180	0	1	1	0
Ni	0.12	0.24	0.56	0.68	0	0	6	9
P	40	70	150	180	0	0	0	0
Pb	-0.101	0.466	1.978	2.545	10	0	5	1
Rb	0.073	0.342625	1.061625	1.33125	0	0	2	0
Sr	0.9	1.29	2.33	2.72	0	0	1	0
Th	0.004	0.0085	0.0205	0.025	0	0	5	4
W	0	0.003	0.011	0.014	0	0	1	3
Y	0	0.0135	0.0495	0.063	0	0	2	3
Zn	0.5	1.25	3.25	4	0	0	2	1
Zr	-0.02	0.01	0.09	0.12	0	0	1	0

Table 5.7. Outlier threshold and number of outliers identified by the [median±2MAD] procedure applied to the 20 elements data composed of 208 samples. MAD: median absolute deviation.

Element	Median-2MAD	Median+2MAD	Nº anomalous samples	
			Negative	Positive
Ag	0.022	0.032	5	10
Ba	5.7	8	28	36
Ce	0.12	0.166	15	32
Cr	0.46	0.62	21	34
Cu	2.775	3.265	18	26
Fe*	50	70	0	40
Ga	0.028	0.04	16	24
La	0.068	0.092	30	30
Mn	8.6	13.4	14	29
Na	50	90	15	38
Ni	0.33	0.47	6	27
P*	90	110	10	55
Pb	0.895	1.585	17	25
Rb	0.5195	0.8825	11	34
Sr	1.57	2.07	22	22
Th	0.012	0.016	18	38
W	0.005	0.009	8	15
Y	0.023	0.039	15	27
Zn	1.8	2.6	5	19
Zr	0.05	0.05	56	74

The thresholds given by both procedures are referential and are further judged with probability plots for each element. Indeed, based on changes in slope on probability plots the background population limits for each element are defined (Table 9).

Table 0.8. Background limits defined by probability plot for each element.

Element	Background lower limit	Background upper limit	Number of background samples
Ag	0.022	0.035	
Ba	5.4	7.3	129
Ce	0.116	0.154	147
Cr	0.45	0.58	148
Cu	2.62	3.22	174
Fe	0.006	0.008	
Ga	0.027	0.043	185
La	0.057	0.091	175
Mn	9.6	12.3	115
Na	0.004	0.011	
Ni	0.35	0.48	157
P	0.009	0.012	
Pb	0.91	1.435	145
Rb	0.519	0.765	120
Sr	1.49	1.99	
Th	0.011	0.018	185
W	0.003	0.01	
Y	0.02	0.04	180
Zn	1.7	2.6	183
Zr	0.04	0.08	

In conclusion, of the three methods used to define background and other population, the 'median±2MAD' procedure was more suitable than the boxplot when looking for outliers. For instance, the boxplot of Mn found one single positive anomaly while the 'median±2MAD' method found 14 and 29 negative and positive anomalies respectively, being the later agreeable with Mn probability plot where there is clearly a population of low concentration defining a negative anomaly. In fact, several thresholds estimated by the 'median±2MAD' (Table 12) coincided with the limit of populations identified on normal-probability plots.

In conclusion, samples ID 65 (Ba), 70 (Cr), 150 (Fe, Ni), 44 (Mn), 120 (Pb), 229 (Th) and 37 (W) where the ones identify as isolated univariate outliers in Q-Q plots.

5.3.5 Multivariate outliers

According to Starkweather (2013) being an outlier on one of the variables under consideration is not a necessary condition for being a multivariate outlier, so the next step attempts to find multiple outlier(s).

In fact, firstly scatterplots in two dimensions with marginal boxplots are performed to assess the presence of bivariate outliers or group of samples separated from the main density of samples. Because of the excessive number of possible combinations of scatterplot between elements, in this study the elements are plotted versus the manganese concentrations.

Several samples in the bivariate scatterplots (Appendix C.3) appear outside the ellipse of main concentration but most important, some samples are isolated. Sample ID 44 in Mn and Zr, 65 in Ba and Zn, 70 in Cr, 150 in Fe and Ni, 229 in Th and 37 in W are isolated.

For multivariate outlier detection, implementation of several robust tests over the dataset are performed using the software R. Table 13 shows the first 30 outliers detected by the 'Chi-Squared plot' and the 'Moutlier plot', listed in descending order of importance.

Table 5.9. Sample ID of the first 30 extreme multiple outliers identified by two different statistical tests ("Chisq" and "Moutlier"). Cont.: continuation.

ID of outlier Chisq	ID of outlier Moutlier	Cont. ID of outlier Chisq	Cont. ID of outlier Moutlier
150	150	160	20
65	65	191	161
229	229	88	160
49	49	52	38
70	70	113	52
44	44	159	113
170	170	198	88
106	120	41	159
185	106	78	198
48	191	13	80
86	185	136	172
120	48	12	41
161	86	38	137
37	37	50	13
20	78	85	136

Both techniques are very consistent in relation to the first most extreme outliers detected. Note that the first six multivariate outliers contain the four isolated outliers detected previously in 5.3.3, although here the anomalous condition of sample 70 is significant and sample 229, which is a single extreme outlier for Th, is here considered as a multiple outlier.

The 'Moutlier' function detect 64 possible outliers, the 'Pcout' function detect 52 possible outliers. All the diagrams and list of these possible outliers are in Appendix C.4.
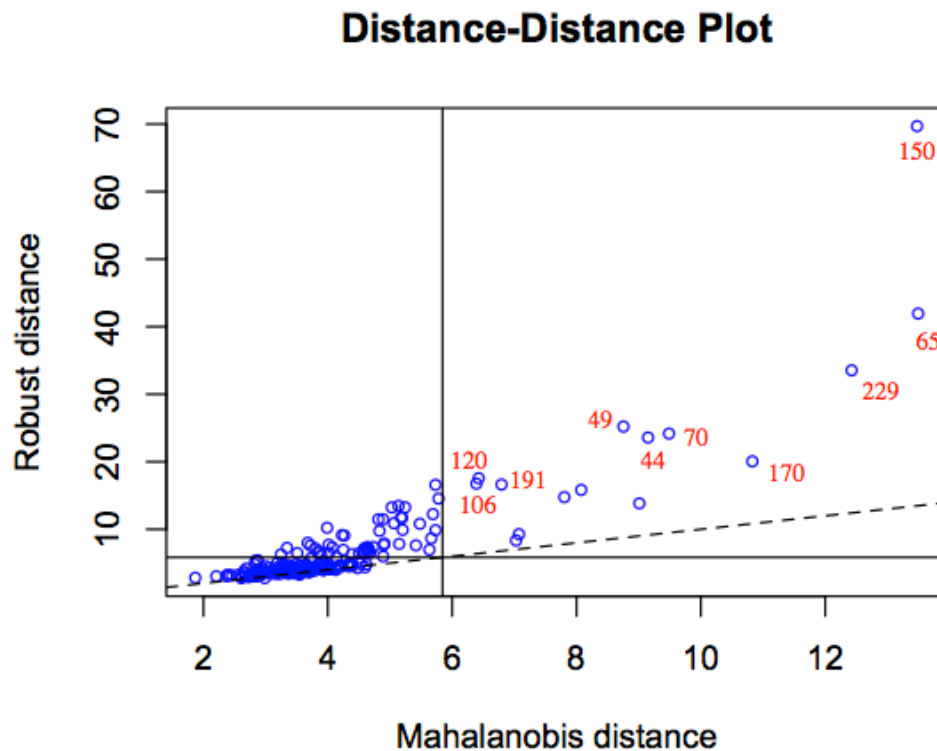
Figure 5.0.2. Distance-distance plot showing the samples relative to their Mahalanobis distance and their robust Mahalanobis distance from the center of all variables's distribution. In red: sample IDs or names of the samples with extreme Mahalanobis distances (upper right).

Summary

Taking into account the univariate and multivariate methods and the spatial distribution of concentration of elements, the presence of three 'isolated' outliers is interpreted (150, 65 and 229), at which point these samples are removed from the dataset. Removal of these three samples does not significantly affect the spatial distribution of elements, although the end result may be considered a more statistically valid product by virtue of removing these questionable samples.

Samples 49, 70, 44 and 170 are also identified as outliers although as they all have similar high Mahalanobis distances (from the center of all variables) they are not removed.

5.3.6 Spatial distribution of the data set

Univariate geochemical maps of the raw data showing the spatial distribution of element concentrations in plan view can be seen in Appendix C.6. Additionally, three cross-sectional views are displayed in order to analyze the variance of elements compared spatially to the vertical projection of mineralization.

Figure 5.3 shows the location of the three profile sections in relation to the surface projection of the known orebody (showing the location of sampling sites obtained in this study and historic drillholes). Profiles of all 20 reliable elements in the three sections are displayed in Appendix C.5.
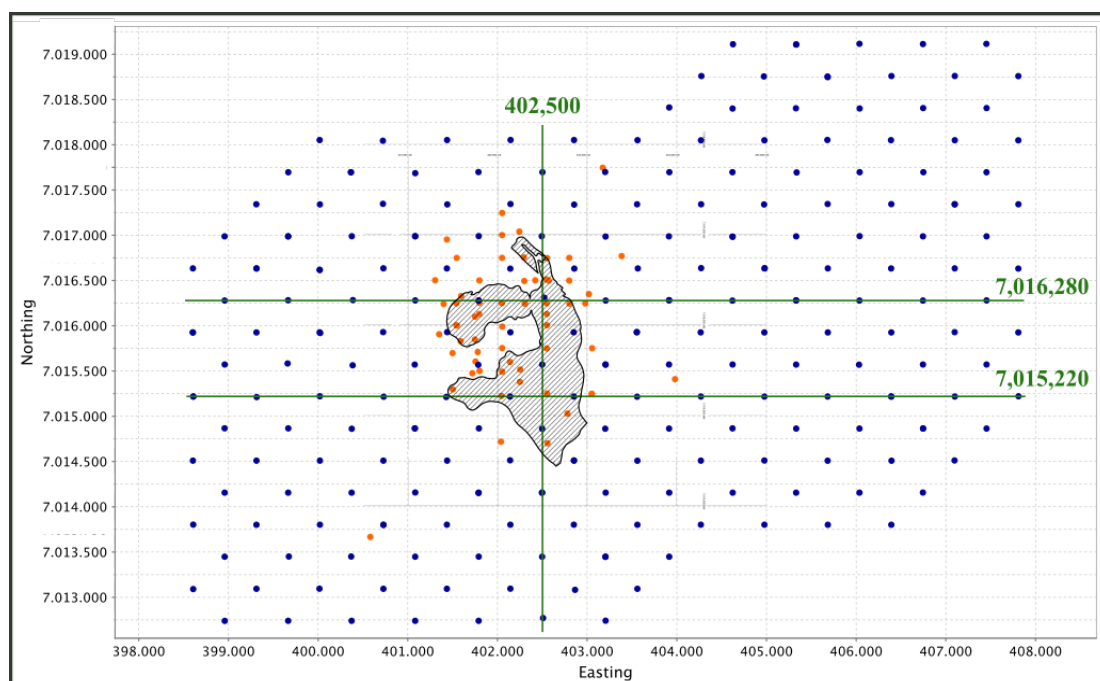
Figure 5.0.3. Spatial map with the location of collectors (blue circles), historic drillholes (orange circles) and approximate shape of Atlántida orebody. Green lines represent two WE and one NS sections.

Figure 0.4. Q-Q plots and spatial distribution of background and anomalous concentrations for Ba, Ce, Cr and Cu. Gray symbols represent the background concentration. Other symbols represent either higher or lower concentration than the background as shown in Q-Q plots.

68
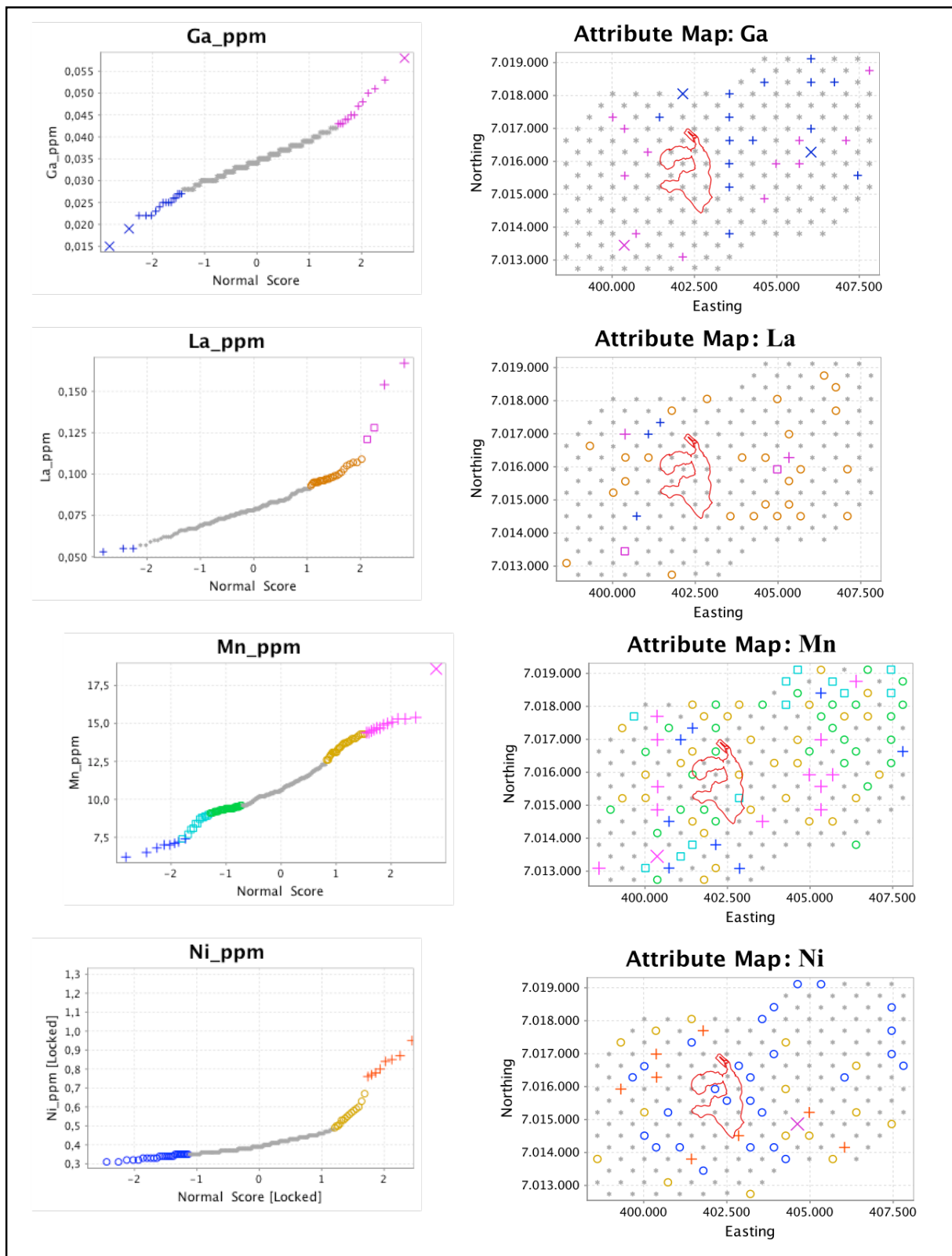
Figure 0.5. Q-Q plots and spatial distribution of background and anomalous concentrations for Ba, Ce, Cr and Cu. Gray symbols represent the background concentration. Other symbols represent either higher or lower concentration than the background as shown in Q-Q plots.
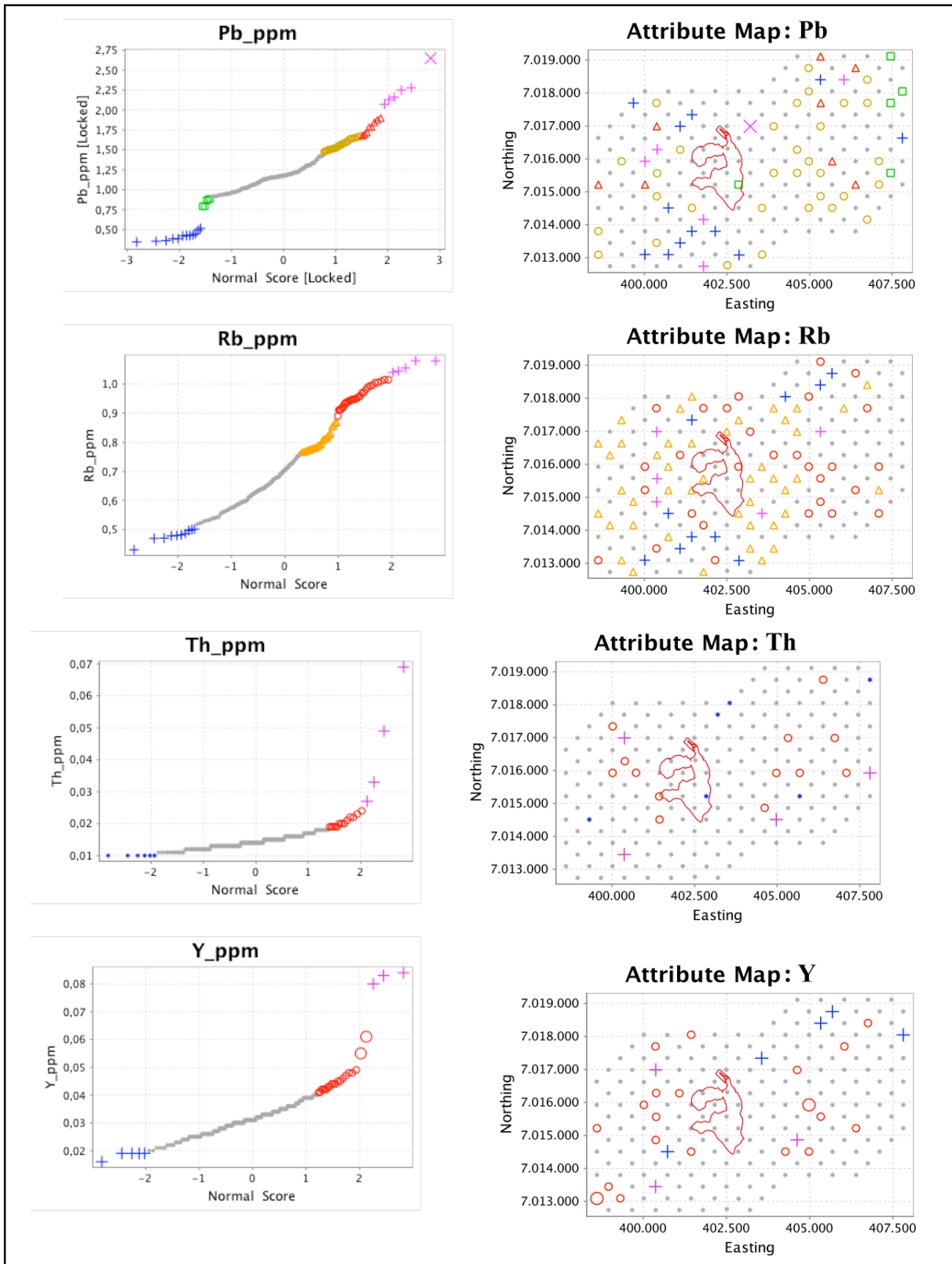
Figure 0.6. Q-Q plots and spatial distribution of background and anomalous concentrations for Ba, Ce, Cr and Cu. Gray symbols represent the background concentration. Other symbols represent either higher or lower concentration than the background as shown in Q-Q plots.

70

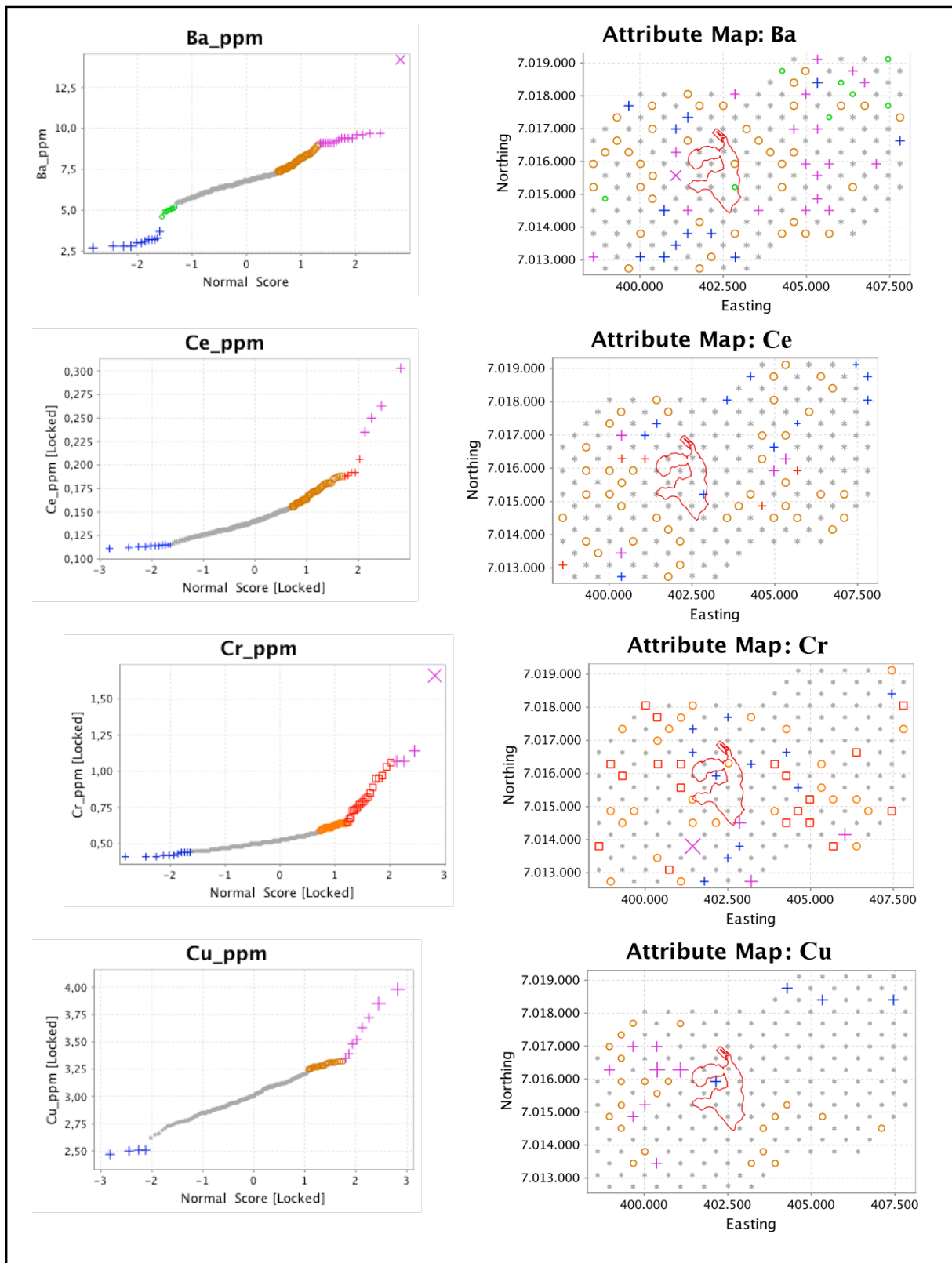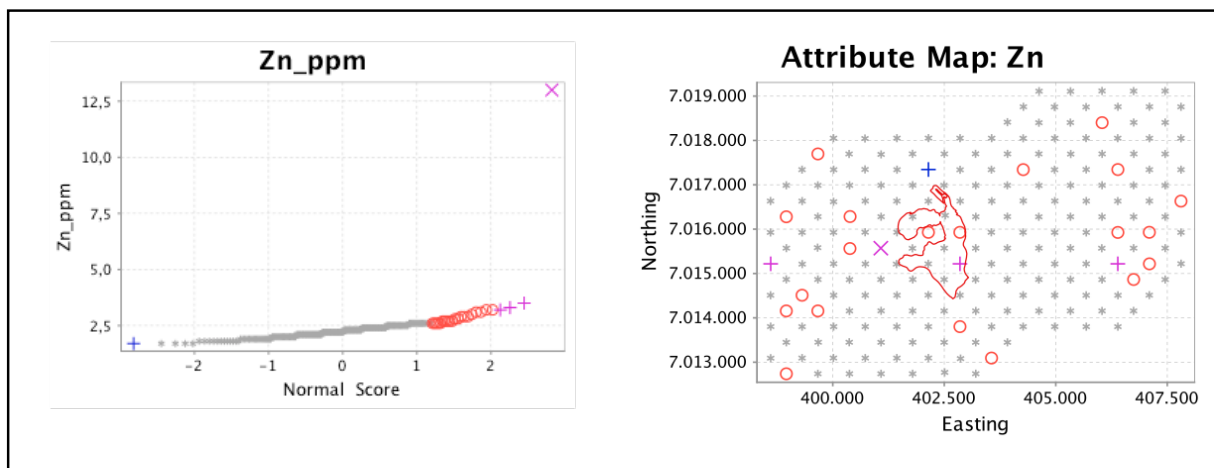**Figure 0.7.** Q-Q plots and spatial distribution of background and anomalous concentrations for Ba, Ce, Cr and Cu. Gray symbols represent the background concentration. Other symbols represent either higher or lower concentration than the background as shown in Q-Q plots.

In profile 7,016,280 N (Figure 5.4), anomalous values for Ba, Ce, Cr, Fe, La, Mn, P, Pb, Rb and Sr occur above background on either side of the mineralized deposit, showing a good 'rabbit ear' shape. This shape can also be seen subtly for Cu, Ni, W and Zn (see Appendix C.5.1). As can be observed, over the mineralized deposit the concentration of the elements mentioned are not depleted but rather are within the background concentration of each element.

Figure 5.0.8. Profiles of elements Ba, Ce, Mn, P, Pb, Rb and Sr in the 7,016,280 N section. The orange line represents the collectors along the section, which are separated about 710 m. The horizontal blue line represents the position of the Atlántida ore body. The two green lines defines the background range of each element (BUL: Background Upper Limit, BLL: Background Lower Limit), the two segmented green lines represent quartiles 1 (Q1) and 3 (Q3) of the background.

Cont. Figure 5.4. Profiles of elements Ba, Ce, Mn, P, Pb, Rb and Sr in the 7,016,280 N section. The orange line represents the collectors along the section, which are separated about 710 m. The horizontal blue line represents the position of the Atlántida ore body. The two green lines defines the background range of each element (BUL: Background Upper Limit, BLL: Background Lower Limit), the two segmented green lines represent quartiles 1 (Q1) and 3 (Q3) of the background.

Although not as neat as section 7,016,280 N, section 7,015,220 N (Figure 5.5) also describes 'rabbit ear' contrast anomalies for some elements but to a lesser grade. Only Cu, Mn, Ni and Rb describe positive contrast anomalies at each side of the deposit, while Ba, Ce, La, P and Sr describe more subtle 'rabbit ear' pattern, that is, if anomalies are considered as values greater than the background third quartile and lower than the background first quartile (Appendix C.5.2).

A characteristic feature of this section is the presence of positive contrast anomalies at the eastern part of the section in some elements like Mn and Rb (Figure 5.5) and in Ba, Ce, Pb, Sr, Y and Zn (Appendix C.5.2), presumably due to the presence of faults or joints that facilitate the ascent of gases.
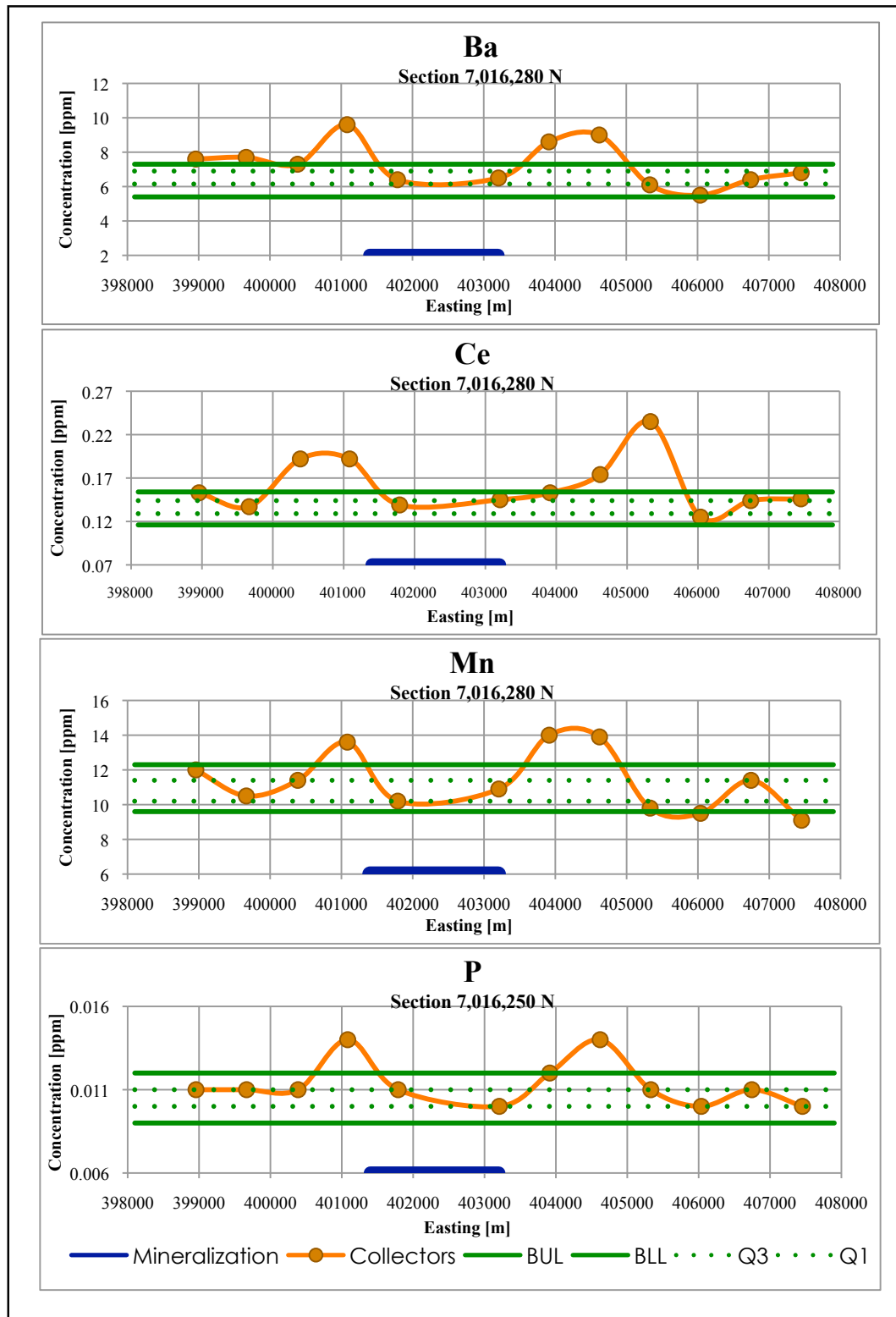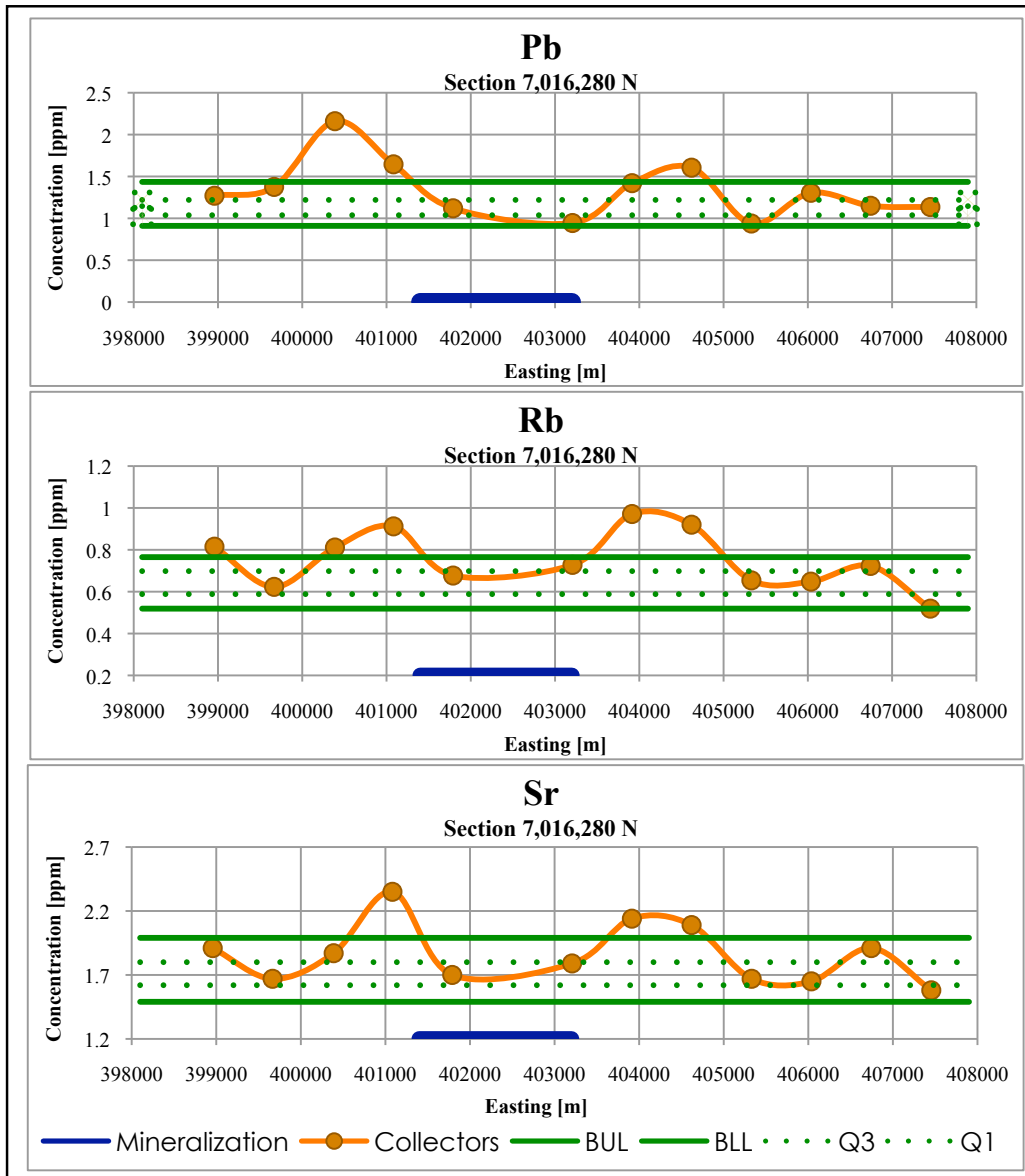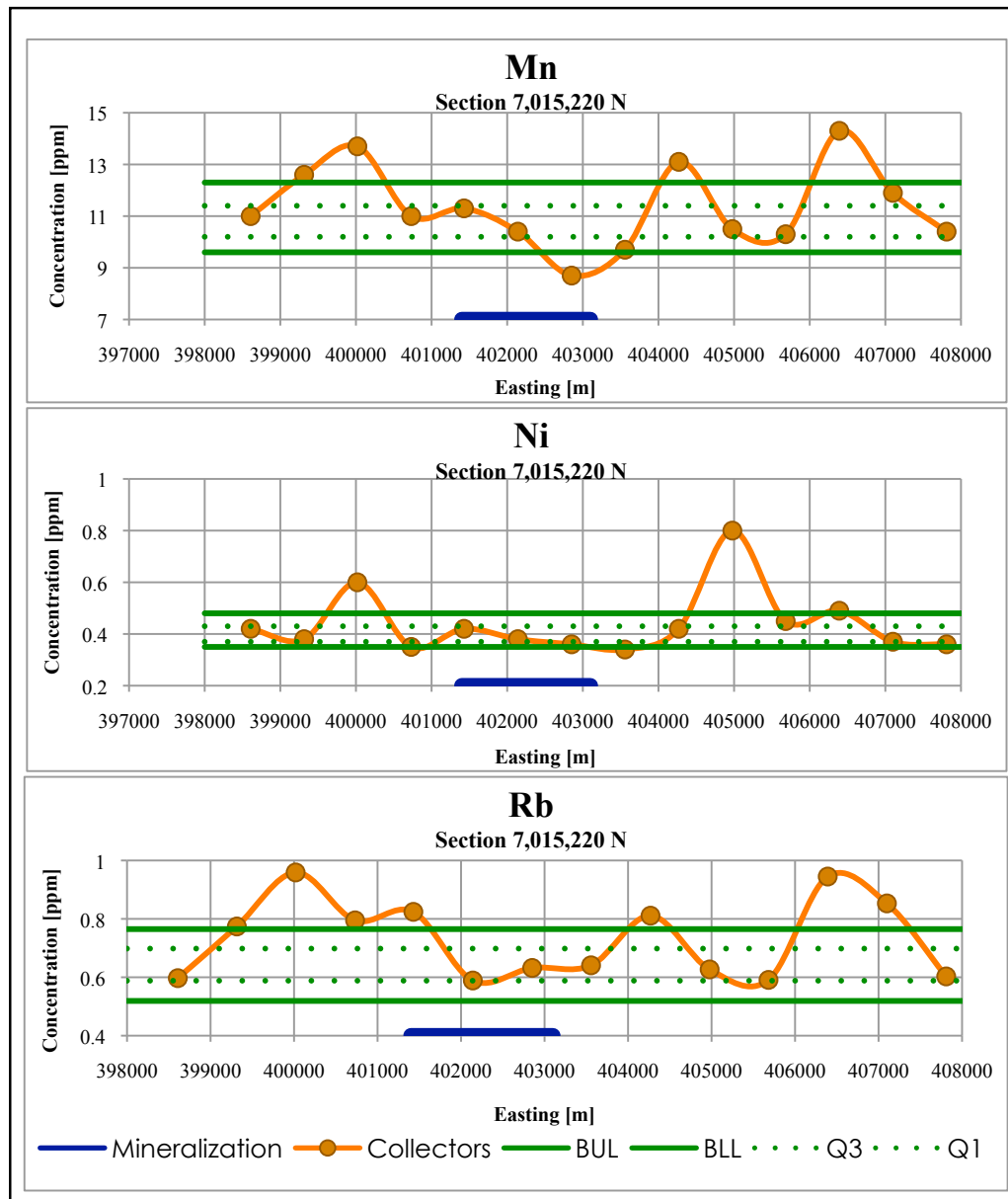

Figure 5.0.9. Profiles of elements Mn, Ni and Rb in the 7,015,220 N section. The orange line represents the collectors along the section, which are separated about 710 m. The horizontal blue line represents the position of Atlántida ore body, the two green lines defines the background range of each element (BUL: Background Upper Limit, BLL: Background Lower Limit), the two segmented green lines represent quartiles 1 (Q1) and 3 (Q3) of the background.

Surprisingly, none of the elements in the NS section 402,500 E show 'rabbit ear' anomalies and the closest one is the shape described by Na (Figure 5.6) over the deposit (observe concentration above the third quartile at either side of the deposit location). Just Ba, Mn and Rb (Appendix C.5.3) have one collector (the one located about 7,017,700 N) with concentration above background. When considering the background limits as the third and first quartile, positive anomalies arise at the eastern side of the deposit for the elements Ce, Cr, La, Ni, Pb, Sr, Th and Zn (Appendix C.5.3).
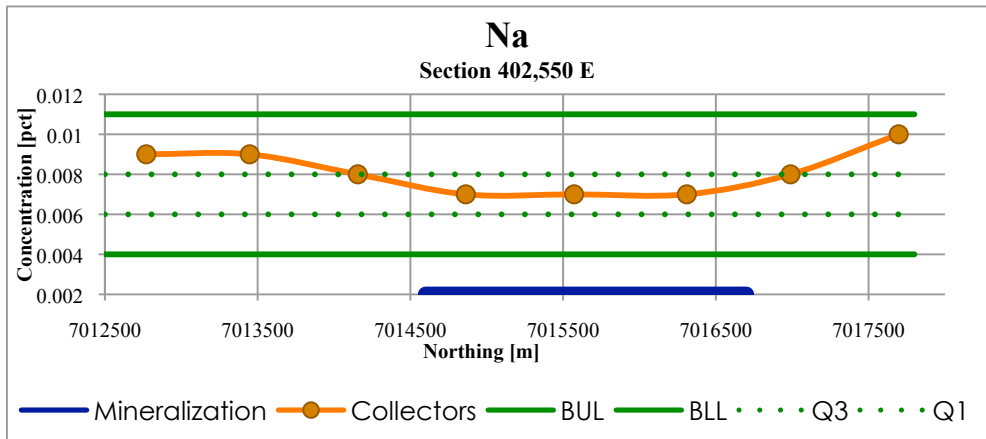
Figure 5.0.10. Sodium in 402,550 E section. The horizontal blue line represents the position of Atlántida ore body, the two green lines defines the background range of each element (BUL: Background Upper Limit, BLL: Background Lower Limit), the two segmented green lines represent quartiles 1 (Q1) and 3 (Q3) of the background.

'Rabbit ear' anomalies are frequently explained in terms of electrochemical dispersion (Govett 1976: Smee 1983; Hamilton 1998) and could be a feasible mechanism for the generation of these contrast anomalies over the Atlántida deposit. According to Aspandiar et al. (2008), simultaneous oxidation and reduction reactions give rise to an Eh differential between the near surface and deeper areas of the body resulting in migration of electrons from the deeper parts to the upper parts along the conductor, in this case Atlantida. According to Govett's model invoking 'Spontaneous Potential' as a transport mechanism (Chapter 2), the upward flow of cations from anode to cathode results in an accumulation of cations at either side of the oxidized sulphide ore with a cation deficient zone in between. From these zones of high concentration, cations move to the surface by chemical diffusion. On a more physical scale, this pattern of anomalism could be controlled partially or entirely by N-S trending faults (and accompanying vertical permeability) bounding the Atlántida porphyry (McTrott, verbal communication).

5.4 Multivariate Analysis

The methodology and relevant information about the functions performed in this section are available in Appendix E.

5.4.1 Multiple Correlation

A graphical plot showing the bivariant Spearman correlations between the 20 variables is shown in Figure 5.7. They are ordered from highest to lower degrees of correlation.
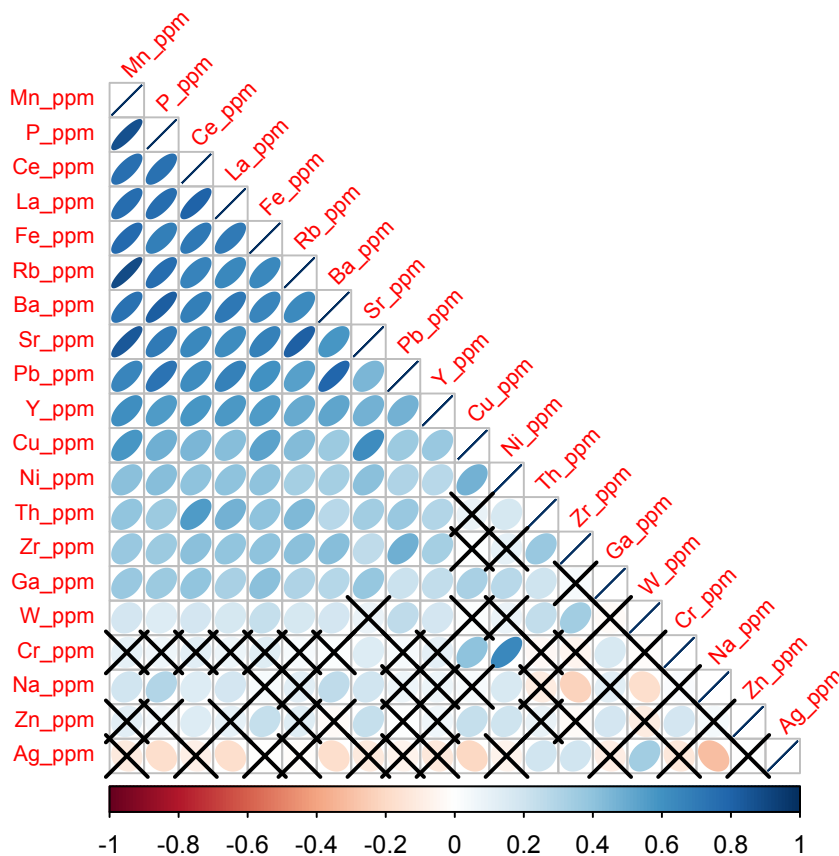
Figure 5.0.11. Ellipse correlation matrix showing the variable's correlation. Correlation of one is represented by a 45º line (elongated ellipse), while near zero correlation is represented by a circle. In other words, the similarity in distribution between two given elements is represented by an ever-thinning ellipse as correlation becomes more pronounced, and more rounded as correlation weakens. The 'X's correspond to those correlations that are not statistically reliable (no correlation). The upper part of the triangle groups the elements with the highest positive correlations.

The individual correlation coefficients can be found in Appendix D. The elements Mn, P, Ce, La Fe, Rb, Ba, Sr, Pb, Y, Cu are highly correlated as shown by the upper half part of the correlation matrix (Figure 5.8), while there is no correlation between the elements Th and Cu; Zr and Cu, Ni and Ga; W and Sr, Cu, Ni, Ga; Na and Fe, Rb, Pb, Y, Cu, Th, Ga, Cr. The elements Cr, Zn and Ag have no correlation with 10 or more elements.

5.4.2 Principal Component Analysis

Principal component analysis is performed using two different functions in the statistical software package R. Spatial distribution and gridded (interpolation) maps of the principal component (PCs) are created in the software ioGAS.

The first PCA (principal component analysis) is performed using the function 'PCAgrid' of the R software. Of the 20 PCs produced, the first eight components were retained since they explained 79.4% of the total variance and have eigenvalues[18] greater than one (Table 5.11; see methodology of PCA in Appendix E.2.1).

Table 5.10. Eigenvalues and proportion of variance explained by the principal components, as well as the loadings of the elements to each PC are shown for the first eight PC retained. Loadings between -0.199 and 0.199 are not shown, while loadings between ± 0.201-0.299 are shown in light gray.

	PC1	PC2	PC3	PC4	PC5	PC6	PC7	PC8
Eigenvalue	3.489	2.104	1.737	1.732	1.509	1.332	1.315	1.281
Prop. Var	0.322	0.117	0.080	0.079	0.060	0.047	0.046	0.043
Cum. Var	0.322	0.439	0.519	0.598	0.658	0.705	0.751	0.794
Ag			-0.296	-0.263	0.235		0.440	
Ba		-0.304	0.268					
Ce	0.305					-0.244		0.315
Cr	0.327	0.376			-0.333	-0.300	0.333	
Cu	0.252							-0.363
Fe								
Ga	0.250			-0.302	-0.415			0.487
La	0.279			0.279		-0.202		
Mn	0.233							
Na			0.662	-0.339	0.306	-0.239		
Ni	0.261						0.231	-0.475
P	0.212							
Pb		-0.355			0.244		0.306	
Rb	0.331					0.572		
Sr	0.343					0.431		
Th	0.246	-0.522	-0.465	-0.376			-0.348	
W				0.389			0.291	0.457
Y				0.502		-0.305	-0.244	
Zn	0.241	0.534	-0.233		0.560		-0.302	
Zr			-0.243		0.236			

---

[18] The eigenvalues indicate the number of significant principal components to retain.

The PCs retained grouped the following elements with high loadings[19] (in parenthesis are the elements that contribute less to the PC, i.e., loadings between ± 0.2 – 0.299):

- ➤ PC1: Sr, Rb, Cr, Ce, (La, Ni, Cu, Ga, Th, Zn, Mn, P)
- ➤ PC2: Zn, Cr, -Th, -Pb, -Ba
- ➤ PC3: Na, -Th, (-Ag, Ba, -Zr, -Zn)
- ➤ PC4: Y, W, -Th, -Na, -Ga, (La, -Ag)
- ➤ PC5: Zn, Na, -Ga, -Cr, (Pb, Zr, Ag)
- ➤ PC6: Rb, Sr, -Y, -Cr, -Ce, -Na, -La
- ➤ PC7: Ag, Cr, Pb, W, Ni, -Th, -Zn, -Y
- ➤ PC8: Ga, W, Ce, -Ni, -Cu

The spatial variation of the eight principal components scores is depicted in Figure 5.8. See Table X in Appendix D to see the principal component scores[20] for each sample.
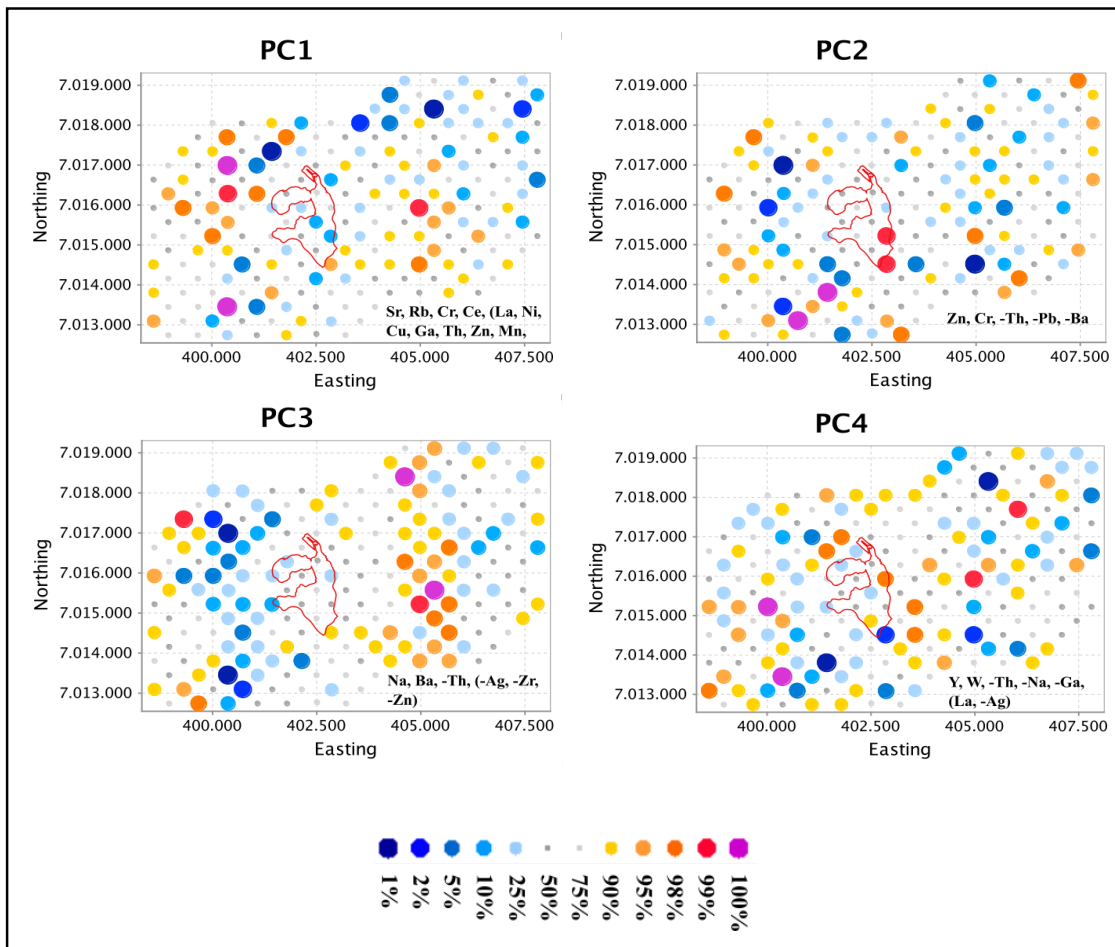
Figure 5.0.12. Symbol point maps of the distribution of the scores of the first eight PCs relative to the projection surface of the Atlántida deposit. The chosen score intervals as well as the bubble sizes and

---

[19] The loadings indicate which variables have positive or negative correlation with individual principal components.
[20] Scores: are the positions of each sample in the new coordinate system of principal components.

colors correspond to the 1, 2, 5, 10, 25, 50, 75, 90, 98, and 99th percentiles of the scores. Hot colors represent high concentrations while cold colors represent low concentrations. Large bubbles represent extreme anomalies (either larger or smaller than the median) while small bubbles represent median to close to median concentrations.
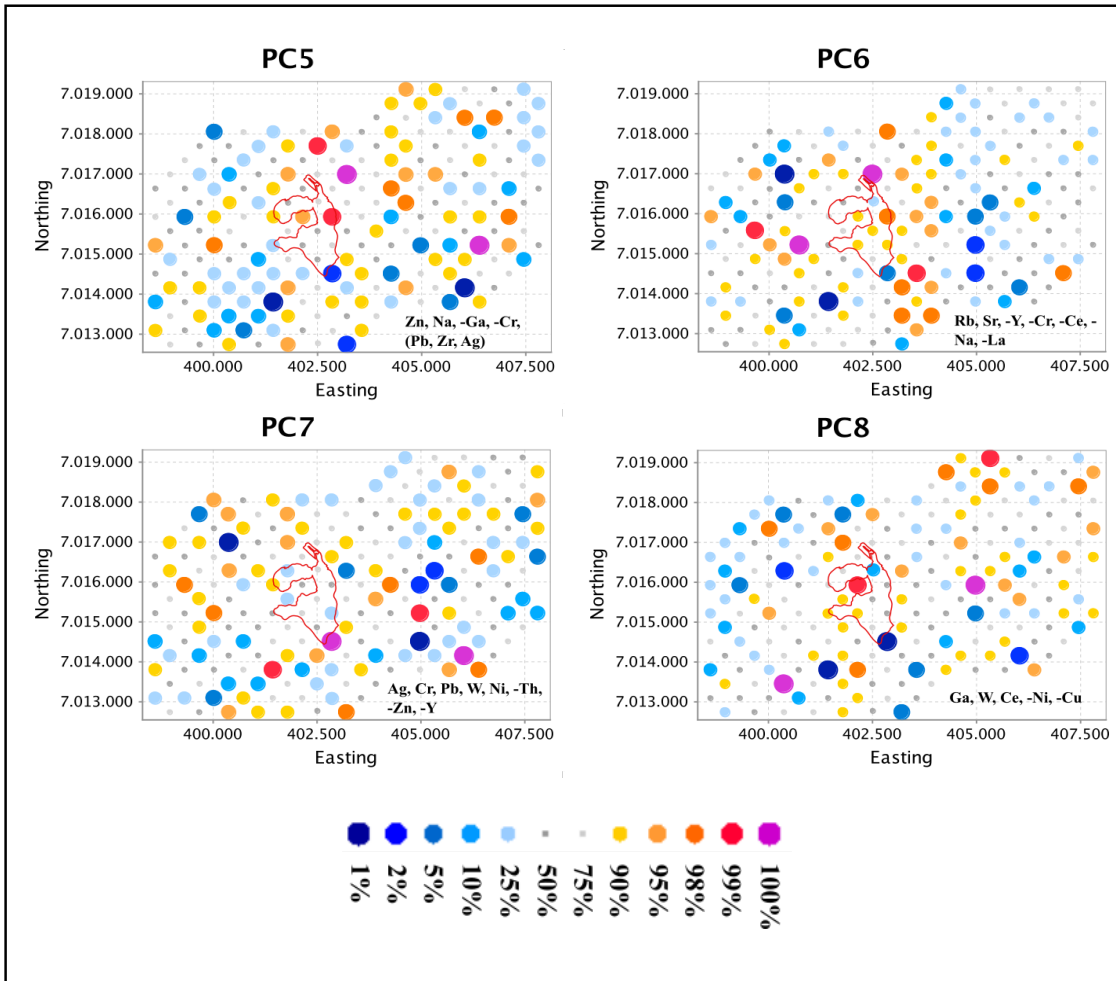
Cont. Figure 5.8. Symbol point maps of the distribution of the scores of the first eight PCs relative to the projection surface of the Atlántida deposit. The chosen score intervals as well as the bubble sizes and colors correspond to the 1, 2, 5, 10, 25, 50, 75, 90, 98, and 99th percentiles of the scores. Hot colors represent high concentrations while cold colors represent low concentrations. Large bubbles represent extreme anomalies (either larger or smaller than the median) while small bubbles represent median to close to median concentrations.

Simple interpolated maps of the eight retained PCs variables are conducted in ioGAS with a modified Inverse Distance Weighting algorithm) and are depicted in Figure 5.9.

Figure 5.0.13. Simple interpolation maps of the eight PCs scores. Hot colors represent higher concentrations and cold colors represent lower concentrations. Interpolation conducted in ioGAS with a modified Inverse Distance Weighting algorithm.
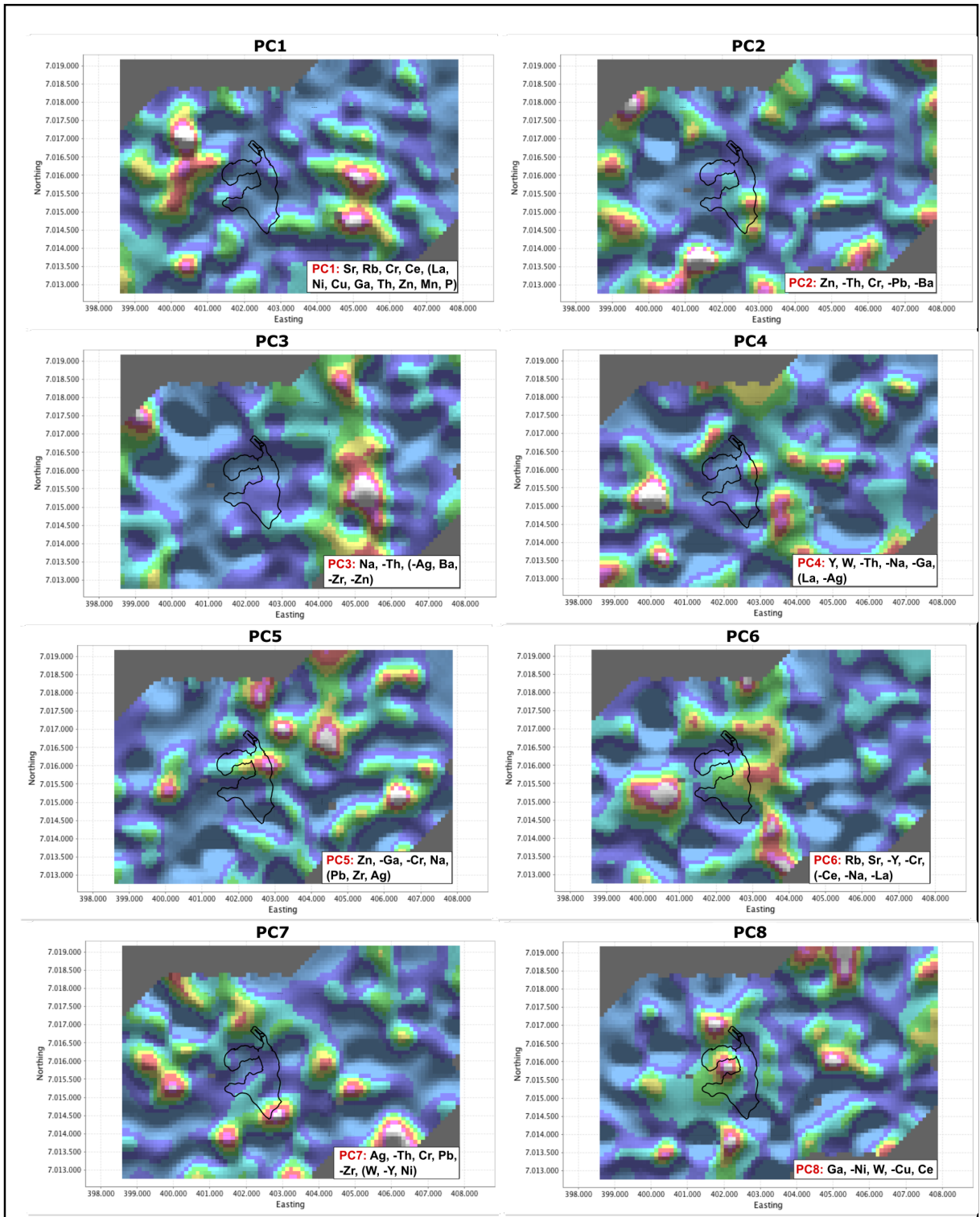
A second PCA was performed, this time with the function 'pcaCoDa' in R software, which considered the compositional nature of the data.

The PCs retained were eight accounting for 86.1% of the total variance.

Table 5.11. Eigenvalues and proportion of variance explained by the principal components, and loadings of the elements to each of the eight PCs are shown. Loadings between -0.199 and 0.199 are not shown, while loadings between ± 0.201-0.299 are shown in light gray.

	PC1	PC2	PC3	PC4	PC5	PC6	PC7	PC8
Eigenvalue	0.117	0.068	0.055	0.033	0.028	0.024	0.019	0.017
Prop. Var	0.279	0.162	0.132	0.079	0.067	0.057	0.046	0.041
Cum. Var	0.279	0.441	0.572	0.651	0.718	0.775	0.821	0.861
Ag	0.250	-0.323						0.297
Ba		0.278				0.224		
Ce								
Cr		-0.404				0.350	0.244	0.239
Cu		-0.222						
Fe								
Ga		-0.205	0.273		0.359			-0.645
La								
Mn						-0.226	0.233	
Na	-0.803		-0.482					
Ni							0.274	
P								
Pb		0.301				0.423		-0.207
Rb		0.257				-0.550	0.257	
Sr						-0.221		
Th				-0.245	0.431		-0.582	0.320
W	0.399		-0.589	0.396	0.278	-0.236		
Y				0.712	-0.429		-0.385	
Zn		-0.358		-0.254	-0.416	-0.311	-0.228	-0.350
Zr	0.292	0.246	-0.385	-0.401	-0.469			

The eight principal components grouped the following elemental associations according to the highest loadings (in parenthesis are the elements that contribute less to the PC, i.e., loadings between ±0.2-0.299):

➢ PC1: W, -Na, (Zr, Ag)
➢ PC2: Pb, -Cr, -Zn, -Ag, (Ba, Rb, Zr, -Cu, -Ga)
➢ PC3: -W, -Na, -Zr, (Ga)
➢ PC4: Y, W, -Zr, (-Zn, -Th)
➢ PC5: Th, Ga, -Zr, -Y, -Zn, (W)
➢ PC6: Pb, Cr, -Rb, -Zn, (Ba, -W, -Mn, -Sr)
➢ PC7: -Th, -Y, (Ni, Rb, Cr, Mn, -Zn)
➢ PC8: Th, -Ga, -Zn, (Ag, Cr,-Pb)

The spatial variation of the eight PC scores is depicted in Figure 5.11. See Table X in Appendix D to see the principal component scores for each sample.
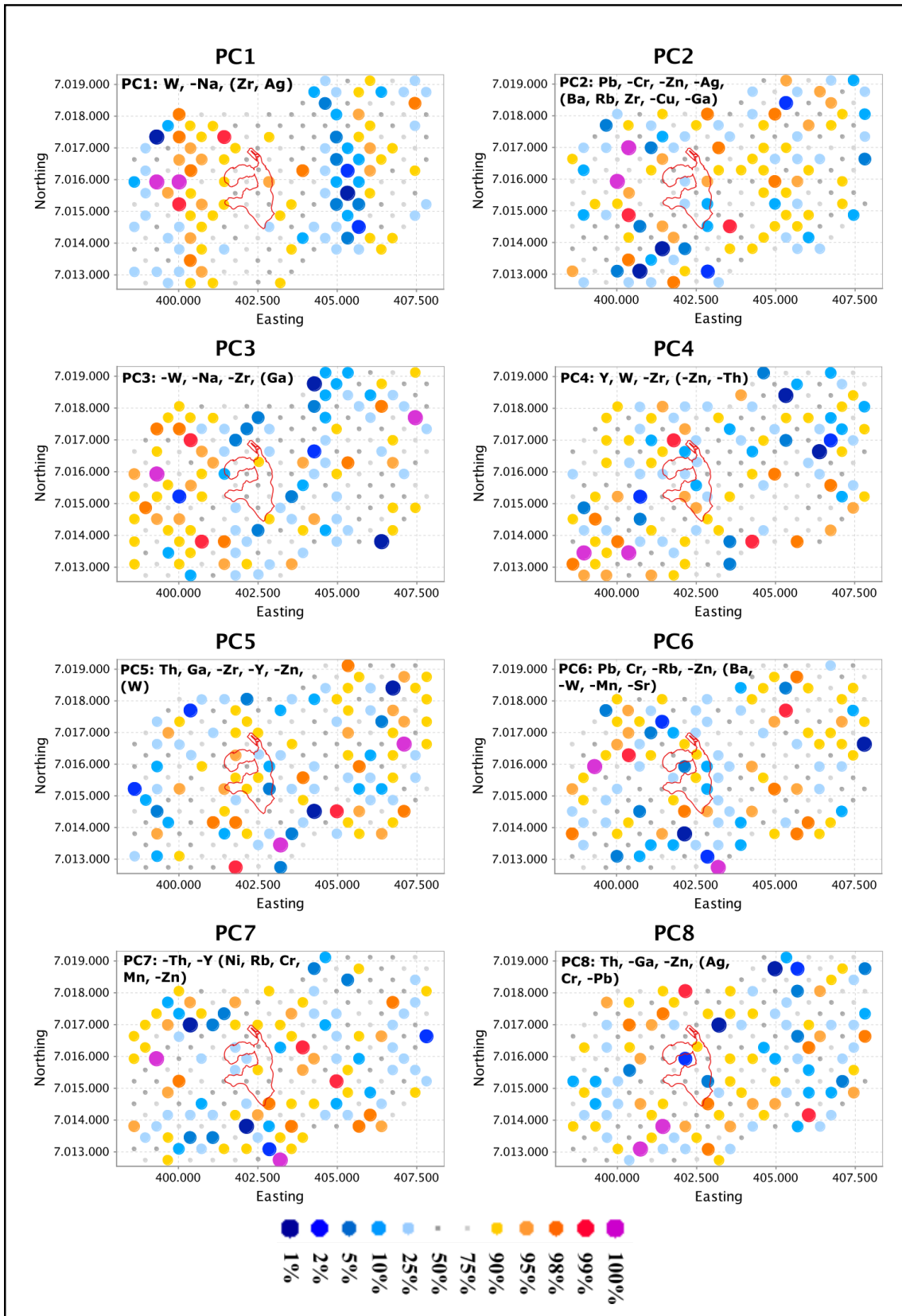
Figure 5.0.14. Symbol point maps of the distribution of the scores of the first eight PCs relative to the projection surface of the Atlántida deposit. The chosen score intervals as well as the bubble sizes and colors correspond to the 1, 2, 5, 10, 25, 50, 75, 90, 98, and 99th percentiles of the scores. Hot colors

represent high concentrations while cold colors represent low concentrations. Large bubbles represent extreme anomalies (either larger or smaller than the median) while small bubbles represent median to close to median concentrations.

Figure 5.11 depicts the interpolated map (with a modified Inverse Distance Weighting algorithm) of the eight PCs retained.
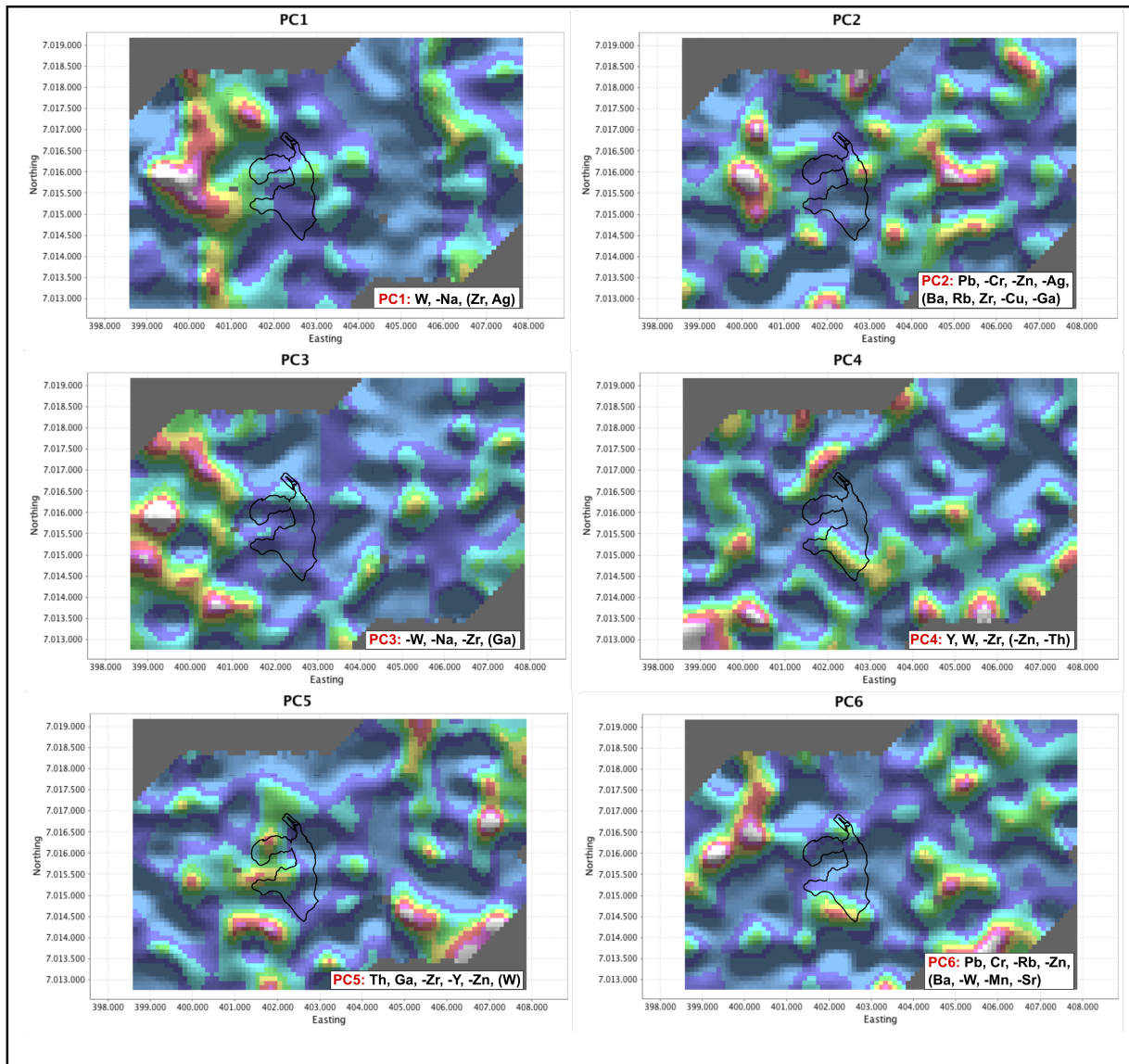
Figure 0.15. Simple interpolation maps of the eight PCs scores. Hot colors represent higher concentration and cold colors represent lower concentrations. Interpolation conducted in ioGAS with a modified Inverse Distance Weighting algorithm.
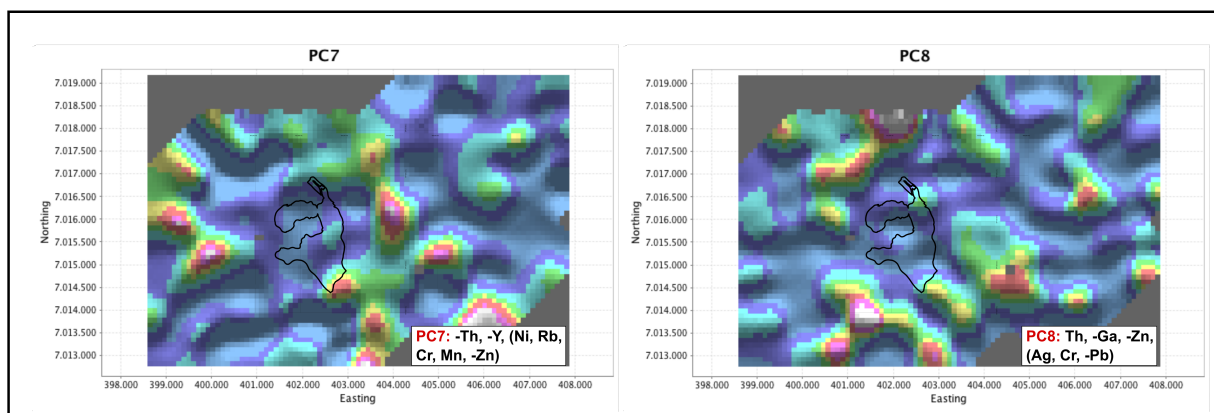
Cont. Figure 0.15. Simple interpolation maps of the eight PCs scores. Hot colors represent higher concentration and cold colors represent lower concentrations. Interpolation conducted in ioGAS with a modified Inverse Distance Weighting algorithm.

5.4.3 Factor Analysis

Robust factor analysis was performed on the data set previously scaled and centered using the function 'FaCov()' (which is not rotated) in R.

The complete output of the non-rotated factor analysis can be found in Appendix D.4. The number of factor retained was seven, explaining 81% of the total variance. Table 16 contains the loadings of the factors retained as well as their eigenvalues, proportion of variance explained by each factor and cumulative variance.

Table 0.12. Loadings or correlation between the 20 elements and the seven factors retained. (FaCov factor analysis). In blue: SS loadings (eigenvalues) of each factor, proportion of variance explained by each factor and the cumulative variance explained by the respective factor and the previous ones. In gray are the loadings with values between 0.2 and 0.299.

	F1	F2	F3	F4	F5	F6	F7
Eigenvalues	8.625	2.482	1.425	1.230	0.865	0.813	0.796
Proportion Var	0.406	0.095	0.085	0.056	0.059	0.055	0.056
Cumulative Var	0.406	0.501	0.586	0.642	0.701	0.756	0.812
Ag			0.682				
Ba	0.855						
Ce	0.825						
Cr		0.925					
Cu	0.484	0.466					-0.408
Fe	0.815						
Ga					0.824		
La	0.881						
Mn	0.956						
Na							0.731
Ni		0.828					
P	0.899						
Pb	0.769						
Rb	0.855						
Sr	0.826						
Th	0.452					0.800	
W			0.831				
Y	0.714						
Zn				0.955			
Zr	0.453		0.539		-0.503		

The factors grouped the following geochemical associations, from highest to lower loadings:

➢ F1: Mn, P, La, Rb, Ba, Sr, Ce, Fe, Pb, Y, (Cu, Zr, Th)
➢ F2: Cr, Ni, (Cu)
➢ F3: W, Ag, Zr
➢ F4: Zn
➢ F5: Ga, -Zr
➢ F6: Th
➢ F7: Na, -Cu, Ba

The first factor explains 40.6% of the variance and grouped the largest amount of elements, being Mn, P, La, Rb, Ba, Sr, Ce, Fe, Pb and Y the elements with the highest loadings. The second factor explains 9.5% of the variance and showed high loadings for Cr and Ni, with minor loading for Cu. The third factor explains 8.5% of the variance and grouped W, Ag and Zr.

Distribution of the factor's scores is depicted in the Figure 5.16, colored according to percentiles 1, 2, 5 10, 25, 50, 75, 90, 95, 98 and 99th.
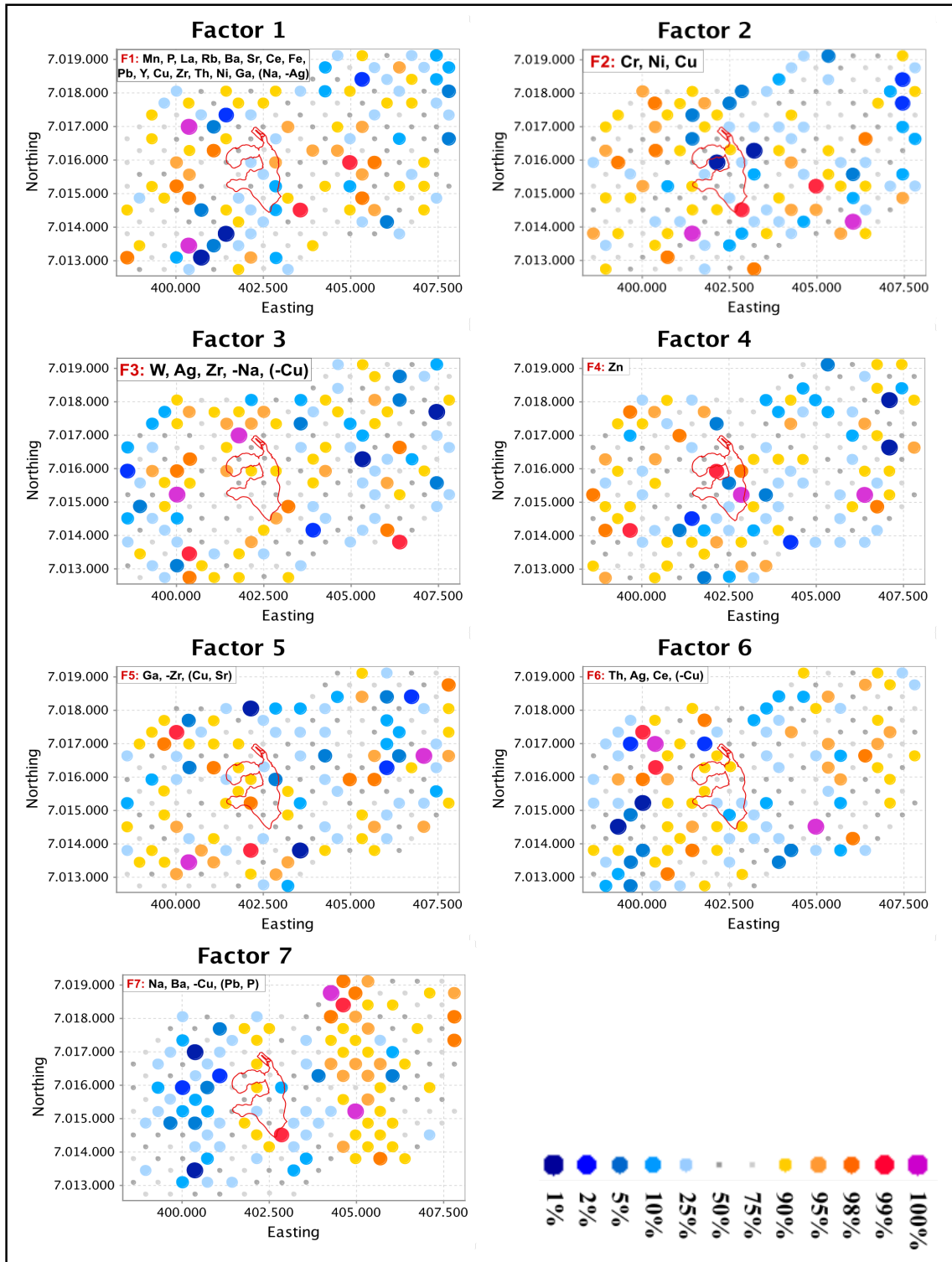
Figure 0.16. Symbol point maps of the distribution of the scores of the first eight PCs relative to the projection surface of the Atlántida deposit. The chosen score intervals as well as the bubble sizes and colors correspond to the 1, 2, 5, 10, 25, 50, 75, 90, 98, and 99th percentiles of the scores. Hot colors represent high concentrations while cold colors represent low concentrations. Large bubbles represent extreme anomalies (either larger or smaller than the median) while small bubbles represent median to close to median concentrations.

86

Furthermore, the interpolated maps (with a modified Inverse Distance Weighting algorithm) of the seven factors retained are depicted in Figure 5.13.

Figure 0.17. Simple interpolation maps of the eight PCs scores. Hot colors represent higher concentrations and cold colors represent lower concentrations. Interpolation conducted in ioGAS with a modified Inverse Distance Weighting algorithm.

5.4.4 Ordinary Cokriging

Ordinary cokriging is performed to interpolate 20 chemical elements measured on 205 geographical positions. The interpolation grid is a square of 9,300 by 6,400 meters composed of 5,952 blocks of 100 by 100 meters each.

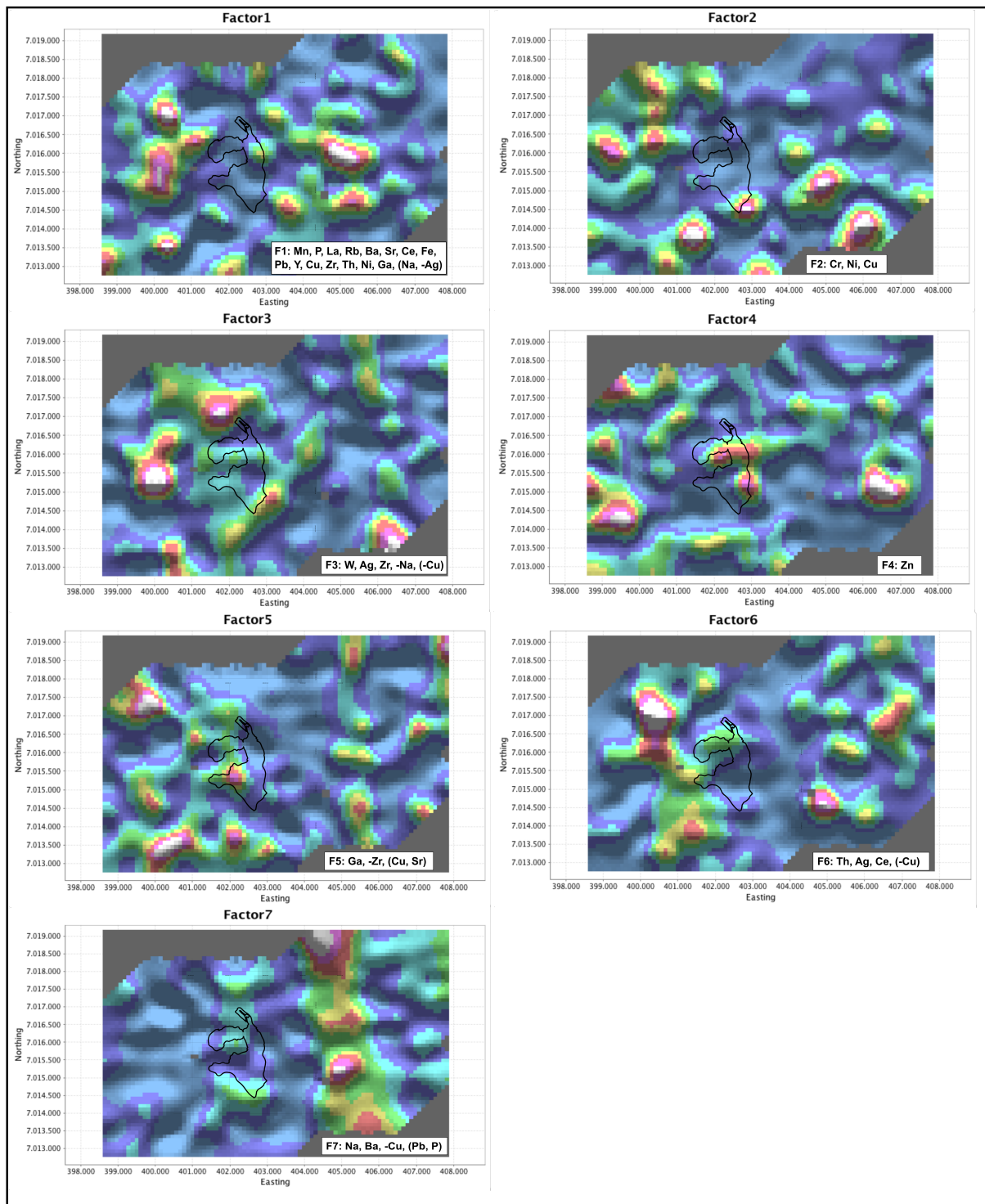The direct and cross variograms of the 20 elements are calculated omnidirectionally and fitted with a linear coregionalization model by means of a semi-automated fitting procedure (Emery (2010) and Goulard and Voltz(1992)). The display of the experimental variograms and fitted models are available in Appendix X.

The neighborhood chosen for searching conditioning data has a radius of 2000 meters.

Distribution maps depicting the raw data ordinary cokriging interpolations for Ag, Cu, Pb, Mn, Rb, Sr and Zn are found in Figure 5.14 to Figure 5.20. The interpolation maps of the rest of the elements can be found in Appendix D.5.1.

Figure 5.14 shows a large, continuous positive contrast anomaly located in the left half of the area, which can be subdivided into a high contrast anomaly NW of the deposit and a less intense contrast anomaly south of the deposit. None of these anomalous high concentrations relate to lithological units at surface. It is possible that Ag distribution in this area is related to Ag halos found commonly around porphyry deposits.

A large NS narrow negative contrast anomaly is located on the right side of the interpolation area. Its cause is likely related to a silver-poor lithology or absence of a silver source.
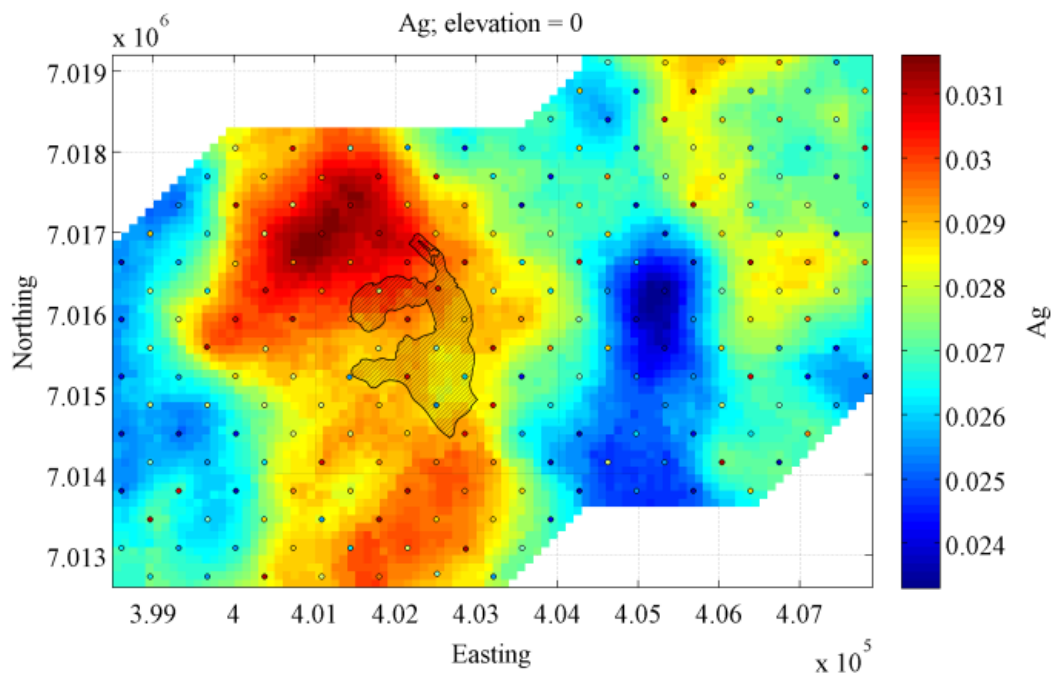
Figure 0.18. Silver ordinary cokriging interpolation of the raw data [ppm]. Small circles represent the location of collectors in the spatial map and their colors represents the original (non interpolated) concentration.

Figure 5.15 shows the copper interpolation with ordinary cokriging. Note that there is a low contrast positive anomaly around the deposit resembling a semi-anular shape, although open to the N of the deposit with background concentrations for Cu. The area of lowest concentration (blue) located in the north-east corner consists of concentrations within background levels.

Regarding the high contrast positive anomaly on the western side of the area, it is not restricted to a lithology and is rather located along the limestone (Chañarcillo Group) and the granodiorite, tonalite and hornblende-bearing quartziferous diorite unit (Kglv). Structural features of the area between the two lithologies are two parallel NW structures along the limestone and a small (orthogonal to the first) structure towards the intrusive unit. Cu preferred those structures and not others, maybe the result of the limestone providing a chemically receptive lithology at the time of mineralization, concentrating elevated copper values which later took advantage of the previously mentioned structures nearby to access the surface environment through gas transport associated with continuous oxidation of copper sulfides, this during the residence time of the collectors.

Figure 0.19. Copper ordinary cokriging interpolation of the raw data [ppm]. Small circles represent the location of collectors (208 locations) in the spatial map and their colors represents the original (non interpolated) concentration.

Pb and Mn (Figures 5.16 and 5.20) delimit the orebody with positive contrast anomalies west, north and east of the deposit, but not south of the deposit where blue colors represent background concentration. Rb and Sr (Figures 5.18 and 5.19) delimit the deposit in all directions, describing a well-define 'ring shape' with the same zonation that Pb and Mn. Zinc (Figure 5.20) outlined the inverse zonation, but also showing a 'ring shape' centered on the deposit.

Figure 0.20. Lead ordinary cokriging interpolation of the raw data [ppm]. Small circles represent the location of collectors in the spatial map and their colors represents the original (not interpolated) concentration.
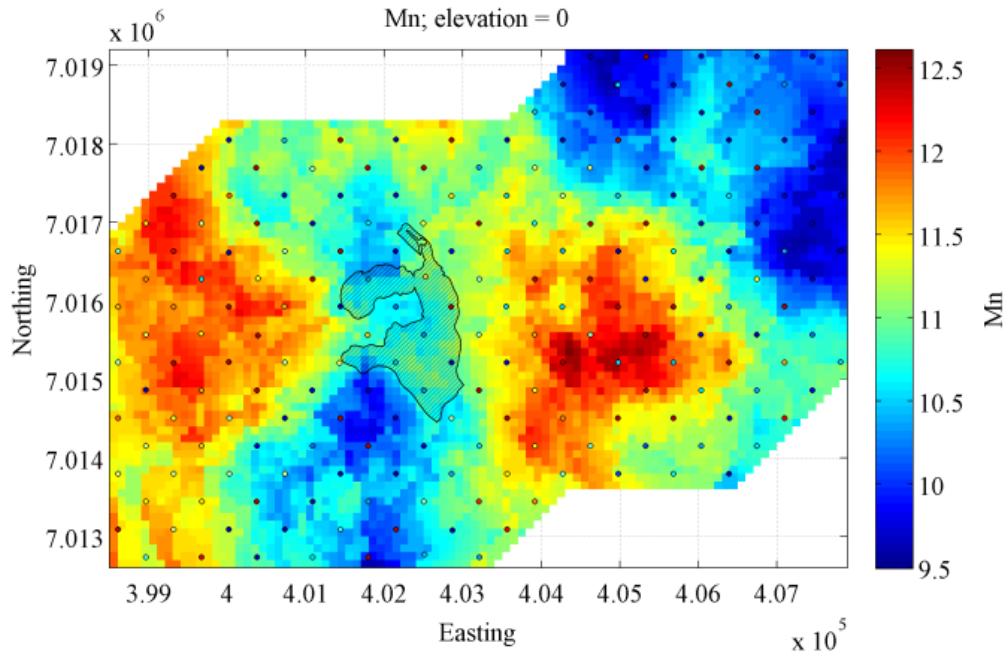
Figure 0.21. Manganese ordinary cokriging interpolation of the raw data [ppm]. Small circles represent the location of collectors in the spatial map and their colors represents the original (not interpolated) concentration.
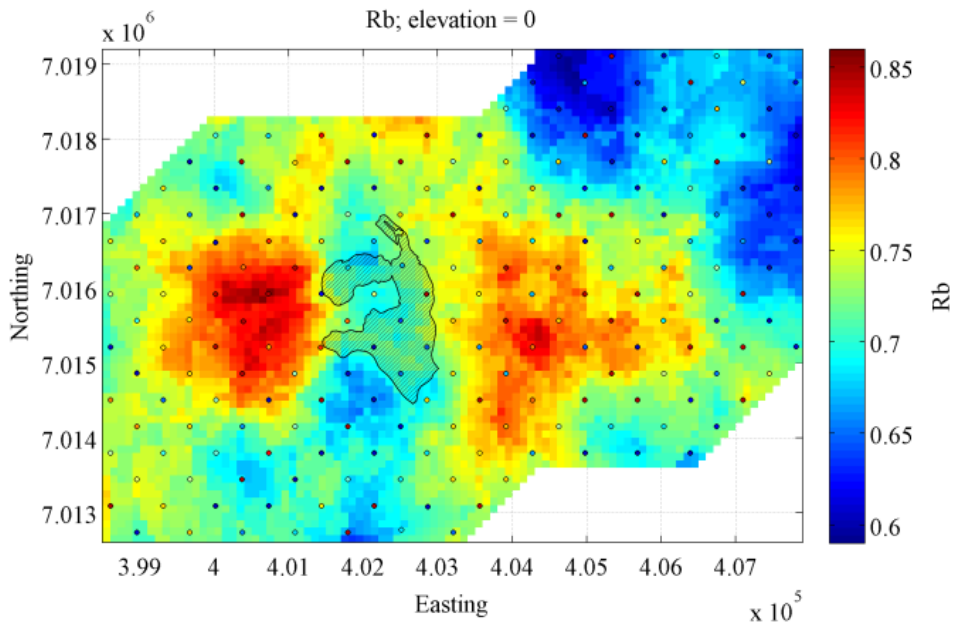
Figure 0.22. Rubidium ordinary cokriging interpolation of the raw data [ppm]. Small circles represent the location of collectors in the spatial map and their colors represents the original (not interpolated) concentration.

Figure 0.23. Strontium ordinary cokriging interpolation of the raw data [ppm]. Small circles represent the location of collectors in the spatial map and their colors represent the original (not interpolated) concentrations.
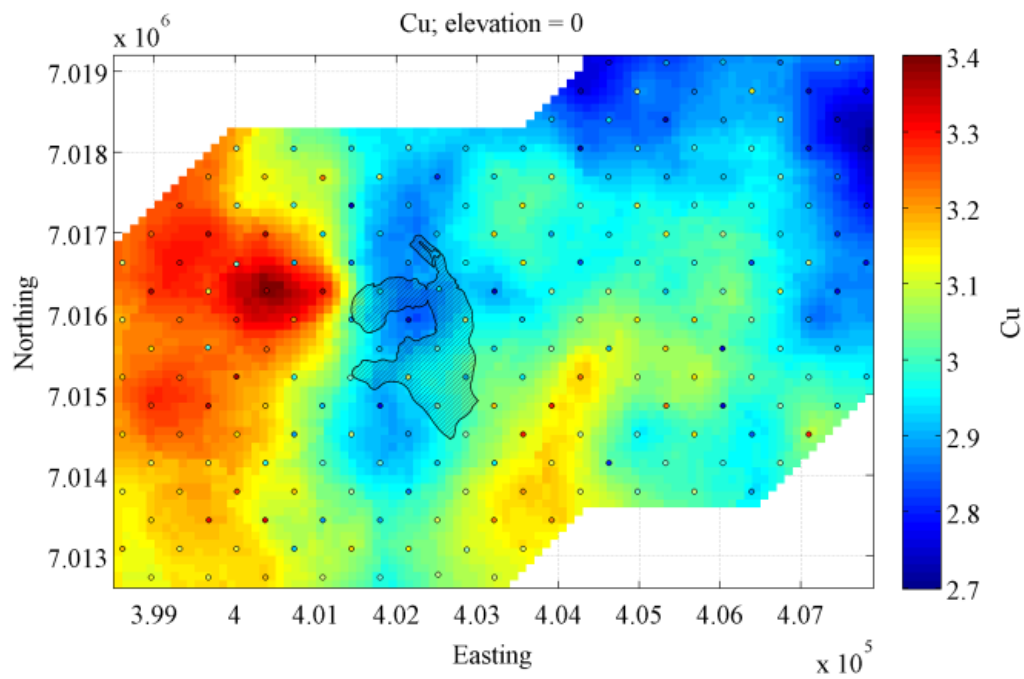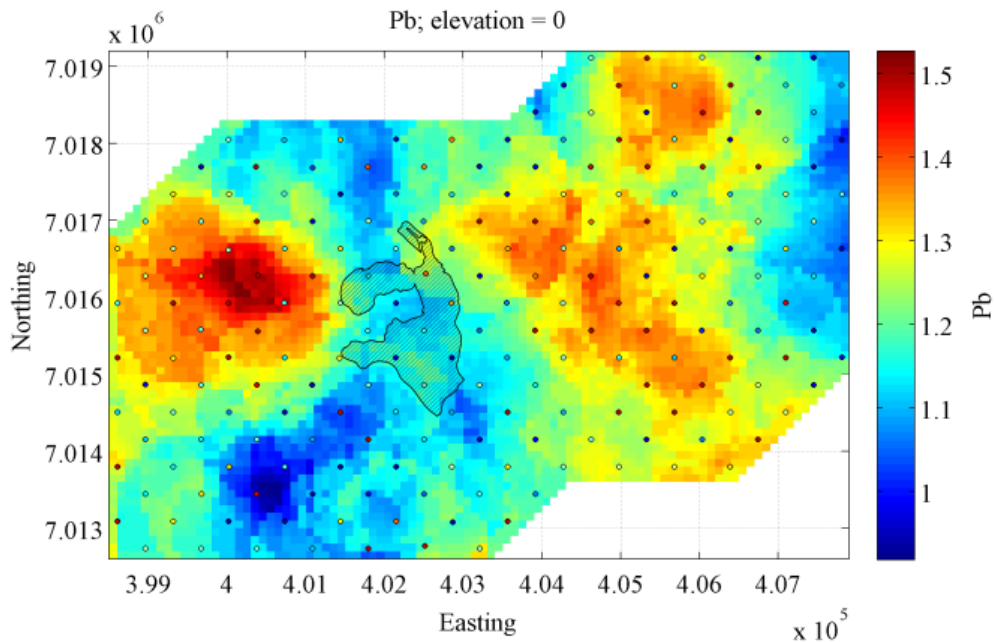
Figure 0.24. Zinc ordinary cokriging interpolation of the raw data [ppm]. Small circles represent the location of collectors in the spatial map and their colors represents the original (not interpolated) concentrations.
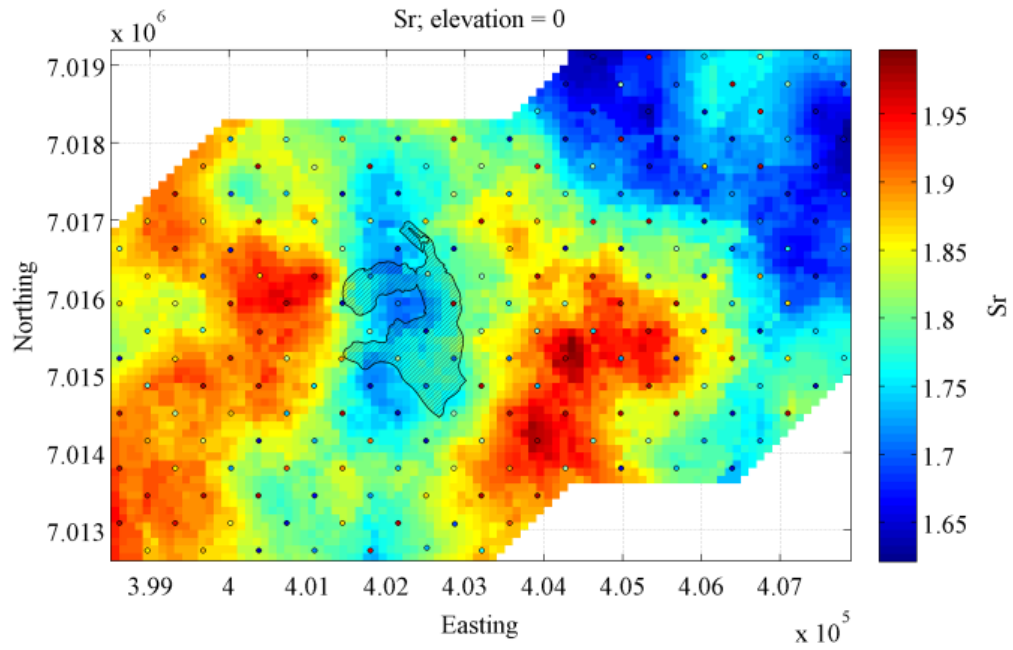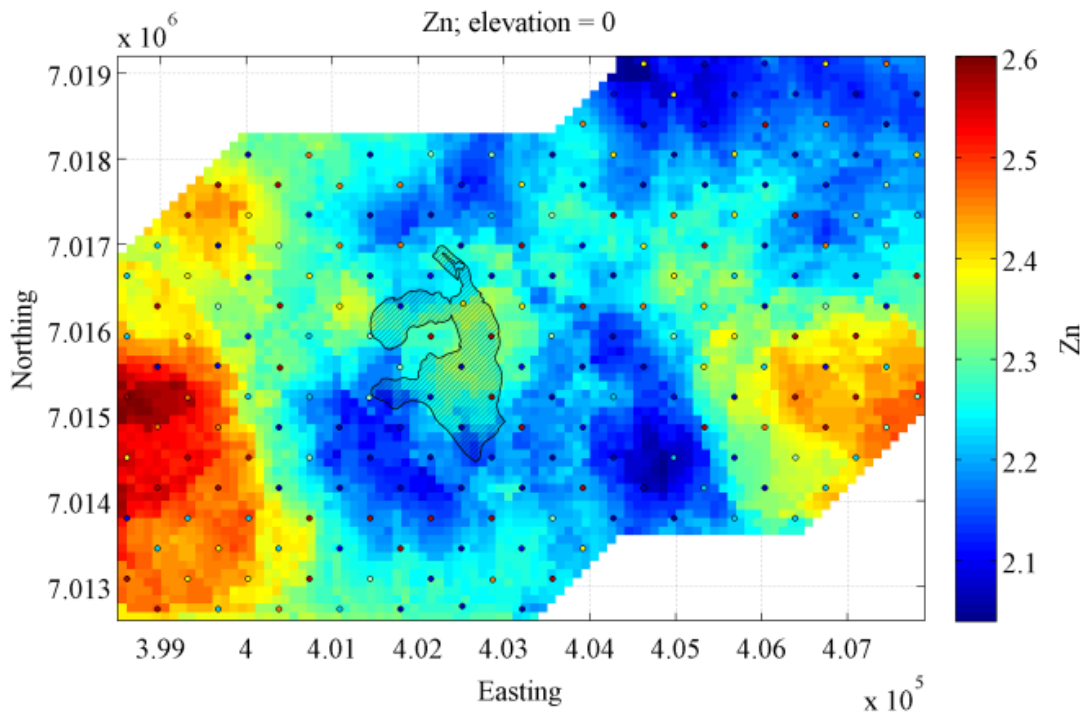
Chapter 6

Discussion

Analysis

After removal of the 234 collectors buried in the ground over a period of 90 days, they were shipped to Andes Analytical Assay Laboratory (AAA) in Chile. The activated carbon was eluted with nitric acid in a multi-step process and the solution analyzed by ICP-MS and ICP-OES. The results obtained turned out to have evident batch level shift problems in almost all the elements measured and contamination issues as evidenced by field duplicates and blank concentrations.

The reasons for the quality problems in data obtained through AAA's analysis method can be attributed to several factors: 1) differences in the conditions employed when analyzing different batches (different nitric acid, time of the reaction or environmental conditions in the laboratory), and/or 2) poor instrument calibration between batches.

A second analysis is done, this time by ALS-Chemex Laboratory, where the remaining activated carbon is digested with aqua regia solution. The batch level shift problem is solved and this technique result in reliable data.

QAQC

The activated carbon analyses of the 234 collectors (including 14 field duplicates, 12 field blanks and 208 collectors) for 53 elements yield 47 elements with contents above detection limit (DL). The QAQC determine 20 reliable elements in terms of analytical and total error associated, these being Ag, Ba, Ce, Cr, Cu, Fe, Ga, La, Na, Ni, Mn, P, Pb, Rb, Sr, Th, W, Y, Zn and Zr.

In terms of analytical reproducibility of the data, the laboratory duplicates showed remarkable results with relative error (%CV) of analytical duplicates <5% for the elements Ba, Cu, Mn and P, between 5-10% for the elements Ce, Fe, La, Pb, Rb and Sr, and between 10-15% for Ag, Ni, W and Y. Field duplicates yielded relative error of field duplicates <5% just for Cu, between 5-10% for Fe, Ni, P and Sr, and between 10-15% for Ag, Cr, Ga, Mn, Th. Thus, Cu has excellent analytical and field reproducibility;

P, Fe and Sr have very good analytical and field reproducibility as well; and Mn, Ag and Ni have good analytical and field reproducibility.

To test the presence or absence of contamination in the analysis, the element concentrations of the 12 field blanks are plotted vs the sequential order of analysis (also know as Shewart control chart). In absence of contamination, the field blanks should all lie within the range 'mean±2standard deviations' of the blanks (calculated without outliers if the case) or within the range 'median±2mad' (calculated over the total number of blanks). Visual inspection of these plots reveals that the elements Ba, Cr, Ga, Na, Ni, Pb, W and Zn have values outside the acceptable range. The reason could be due to contamination either during the residence of the collectors in the field or during storage and/or subsequent analysis in the laboratory, analytical error, or rather due to real concentration of some blanks that differ from most of the blanks, probably related to the homogeneity of activated carbon with which collectors are elaborated (although in the manufacture of the collectors used here, the total amount of jars was estimated to be used and the contents of these were mixed in order to homogenize the activated carbon between jars), although laboratory contamination is the most likely.

Finally, accuracy, tested with four international standards (reference materials), is in general sufficient as evidenced by three out of four international standards.

Exploratory Data Analysis

Comparison between the basic statistics of the blanks and the collectors installed and exposed in the field (without QAQC samples) evidenced that the concentration of the second are different from the blanks, either containing more and less concentrations relative to blanks, evidencing processes of adsorption and liberation of gases by the activated carbon as well as signal capture.

The examination of histograms and Q-Q plots (or normal probability plots) one variable at the time, for a total of the 20 reliable elements, showed the presence of multi-element geochemical populations, several outliers and that the nature of the distributions is not normal (except for Sr which is log-normally distributed) as supported by statistical tests for normality. That said, and considering that determination of background populations is necessary in order to properly isolate anomalies that might be related to mineralization (Yusta et al, 1998), to identify background populations subdivisions of samples are carried out through Q-Q plots for each element on the basis of breaks and changes in slope. The background population per element is determined, as well as the corresponding natural variability of them. It is important to observe that Ag, Fe, Na, P, W, Zr have poor resolution as evidenced in normal probability plots (Q-Q plot), making it difficult to separate background from anomalies.

Regarding the handling of outliers, when looking at one variable at a time, the suspected outliers are identified but none of them deleted. Multi-statistical approach is performed to identify multiple-outliers. Indeed, the number of isolated outliers found in the dataset is three and since they are excessively anomalous, they were interpreted as an error and thus deleted from further study.

The concentration of elements compared to their corresponding background range is analyzed through three profile sections. Section WE 7,016,280 N, located in the northern part of the Atlántida deposit (see Figure 5.3), shows anomalous quantities for Ba, Ce, Cr, Fe, La, Mn, P, Pb, Rb and Sr above background on either side of the mineralized deposit while background concentration are found directly over the deposit, producing a 'rabbit ear' pattern responses.

On section WE 7,015,250 N only Cu, Mn, Ni and Rb have concentration above background at each side of the deposit, while less clear and sometimes extending a bit farther than the deposit the elements Ba, Ce, La, P, and Sr have concentrations above background (if not, above the background third quartile) at either side of the deposit.

The presence of these 'rabbit ear' patterns over the mineralized deposit is likely due to oxidation of the buried ore.

There are no 'rabbit ear' pattern anomalies over the section NS 403,550 E, moreover there are just some few concentrations outside the background range along the section. The decreased response in this section is possibly explained by the presence of active faults or conduits that allowed redistribution of anomalies by modern day groundwater flow.

Multivariate statistics

Principal component analysis (PCA), Factor analysis (FA) and Ordinary Cokriging interpolation are performed in this study to assess relationships within the 20 reliable elements.

PCA first performed using the 'PCAgrid' function in the statistical software R produced eight components that explained 81% of the total variance. Of them, PC1, PC4, PC6 and PC7 give more information about the location of the deposit.

PC1 groups Sr, Rb, Cr, Ce, and agrees with the high correlation between Sr, Rb and Ce shown by the Spearman bivariant correlation matrix. Cr is interpreted to be part of the group because of its high correlation with Cu, which is highly correlated with Sr, Rb and Ce. The interpolation map of PC1 yielded a low concentration zone over the deposit, surrounded by discrete high contrast anomalies around the deposit.

PC4 Y, W, -Th, -Na and –Ga.

PC6 groups Rb, Sr, -Y and –Cr, while PC7 groups Ag, -Th, Cr, Pb and –Zn, both delimit the deposit but not exclusively, leaving other areas of low concentrations. PC3 mainly reflects Na and Ba concentrations and is spatially agreeable with their spatial univariate maps. The remaining components are ambiguous and do not give a good approximation of the location of Atlántida.

The second PCA performed uses the funtion 'pcaCoDa' of the R environment and, contrary to the first one, performs PCA taking into account the compositional nature of the input data.

This statistical approach yields four interesting PCs (PC2, PC6, PC7 and PC8) that contribute to the reduction of the surveyed area to the position where Atlántida is located. PC2 groups –Cr, -Zn, -Ag and Pb and account for 16% of the total variance. PC2 locates two zones of low concentrations partially surrounded by high contrast anomalies, one of the zones localizing the deposit.

PC6, PC7 and PC8 separate the surveyed area in three zones. PC6 groups the elements –Rb, Pb, Cr and –Zn and account for 5.7% of the total variance, PC7 groups – Th and Y explaining 4.6% of the variance and PC8 groups –Ga, -Zn and Th explaining 4.1% of the variance. Al of which localize the deposit.

Factor analysis yield seven factors that explained 81.2% of the variance. The first factor (F1) represented by Mn, P, La, Rb, Ba, Sr, Ce, Fe, Pb, Y and Cu is interpreted as representing a group of cations[21] that might be related to electrochemical processes of dispersion. This association coincides with the first 11 elements with the highest correlation established from the Spearman bivariant correlation matrix. Factor 2 grouped Cr and Ni, with minor loading for Cu and is interpreted to either represent the presence of mafic rocks and/or copper hydrothermal mineralization. Factor 3 grouped W, Ag and Zr and is interpreted to represent sulfide minerals like molybdenite, galena and chalcopyrite, since W^{+4} and Zr^{+4} ion has a radius close to that of Mo^{+4} and Ag is widely present as a trace element in galena, chalcopyrite and others. Factor 4 represents just Zn.

The spatial distribution of the factors F1 to F7 (except F4) show zones of background concentration above the deposit. Interpolated maps of the factors result in significant contrast anomalies describing semi-anular shapes, particularly F4 has a zone of high concentration above the deposit surrounded by low concentration, while the factors F1, F2, F3 describe the inverse zonation.

---

[21] The oxidation states are shown in parenthesis: F1: Mn (+2, +3), P (-3, +3, +5), La (+3), Rb (+1), Ba (+2), Sr (+2), Ce (+3, +4), Fe (+2, +3), Pb (+2, +4), Y (+3), Cu (+1, +2); F2: Cr (+3, +6), Ni (+2, +3); F3: W (+4, +6), Ag (0, +1, +2), Zr (+4); F4: Zn (+2).

Spatial maps of ordinary cokriging interpolation yield anomalies for Cu, Mn, Pb, Rb, Sr and Zn describing a semi-anular shape centered on the deposit. Cu, Mn, Pb, Rb and Sr with background concentrations above the deposit surrounded by a semi-anular high concentration pattern, while Zn described the inverse. From these, the element that best describes or localizes the deposit is Sr, showing a well-defined semi-anular shape anomaly agreeable with the 'rabbit ears' pattern above the deposit and most importantly is highly precise as shown by QAQC of analytical and field duplicates. On the other hand the poor resolution for Ag, Fe, Na, P, W, Zr manifests with severe (not continuous) changes in concentrations in the corresponding cokriging maps.

Notice that the semi-anular shape described by Cu, Mn, Pb, Rb and Sr in the cokriging maps is agreeable with the semi-anular shape described by the interpolation maps of F1 (which contains, among others, these elements), and that the same inverse semi-anular zonation described by Zn in the cokriging map is shown by F4 (Zn) in the factor analysis. The remaining elements do not depict the semi-anular shape in the cokriging maps, but they do when they are grouped as in F2 and F3.

A completely different feature is found in the sodium cokriging interpolation map (Appendix D.5.1). It illustrates NS high contrast positive and negative contrast anomalies described by sodium when are not explained in terms of lithological units. Since Na is non-volatile to vapour transport, the sodium anomaly might be explained by effusion of mineralized groundwater to the surface probably by seismic pumping through the fracture zone located in the east part of the sampled area. Evidence of saline groundwater having reached the surface and evaporated is reported in Cameron (2004) in three sites in Chile (Spence, Gaby Sur and Mansa Mina). But care must be taken since Na in general is likely a deceptive element in the search for porphyries in Atacama, as groundwater and ubiquitous caliche in the area provide a ready source of Na cations (environmental contamination, not true signal from the underlying porphyry) (Trott, verbal communication). That being said, redistribution of Na by fluids/gases moving through structure may be a guide to covered structures.

Similarly to the Na interpolated map, Ba and P yield a NS continuous area of high concentrations on the eastern side of the area that does not seem to relate to lithology and are more likely related to the highly fractured zone in the area (Appendix D.5.2). Oxidation of the orebody may have promoted the release of barium (a relatively volatile element) from biotite, its intermediate mobility plus the availability of fractures making possible the wide distribution of barium in areas adjacent to the deposit. Phosphorous tends to locate the orebody with positive anomalies to the east and west but neither in the north or south where in conjunction with the orebody, is characterized by background concentrations only.

Another interesting feature in cokriging maps was described by Ce,Th, Zr. The interpolation of cerium and thorium locate the orebody projection in a NS area of low

concentrations. The high contrast positive anomaly NW of the deposit is present for Ce, Th and Zr and is not related to lithological contacts. As the mobility of these three elements is relatively low (Rose et, 1979) they probably migrated upward facilitated by a NW active fault from the deposit.

It is important to notice that the fitting of semivariograms were important when interpolating. The first maps given by the cokriging (not included in this thesis) were not as clear as the ones presented in Chapter 5. The reason was that the fitting of the direct and cross variograms was not good enough the first time.

Regarding the semi-anular shape of the contrast anomalies described above, its explanation is associated with metal transport mechanisms as well as the underlying lithology and alteration zones. One arguing point could be, well what happens if the structural setting of the area of study is such that it caused the described shape of the anomalies?

Chapter 7

Conclusions

In the arid environment of northern Chile, dispersion of metals from buried deposits through transported covers occurs in mobile forms such as ions or micro-particles carried up by water and/or gas through electrochemical processes (Hamilton, 1998), or by cyclical dilatancy pumping, i.e. the structurally induced permeability cycling that occurs before and after earthquakes (Cameron and Xie, 2002) (Xie et al., 2011). Geochemical results from several studies support the likelihood of vertical transport of metals through thick transported cover (Fabris et al., 2009). Thus, weathering of mineral deposits imparts a chemical signature on ground and surface water (Wanty et al., 2003).

The Atlántida Cu-Au-Mo porphyry deposit is covered by post-mineral piedmont gravels up to 80 m. Atlántida alteration is mainly phyllic and a potassic core starts at approximately X m depth. Adjacent skarn is present in the contact areas between the intrusive fases and the limestones. Mineralization is predominantly pirite, chalcopyrite with minor molybdenite and gold.

This study set out to check whether or not the gas collectors inserted in the ground are a viable tool used to capture a present time signal from the buried deposit. The gas collector method is promising since they seek to eliminate soil heterogeneity using a homogeneous sample medium that equilibrates with the surrounding medium (Lopez, 2014) and thus are not influenced by the different regolith units.

For several reasons it is impossible to determine a range that defines the true background population. Among these reasons the most obvious is that the geochemical data is spatially dependent and at each sample site a range of different processes have influenced the element abundances measured (McQueen, X). Then it should be natural that different populations are overlapped, making it difficult to define real limits to separate background from anomalies. Nevertheless, good approximations can be done and so, in this thesis the background limits are defined taking into account the distribution of the data, i.e., different elements are treated differently. That said, it is important to apply robust or non-parametric techniques through out when applying statistical analysis in a geochemical data that inherently are related to multi-element events.

Between the multi-element statistical analyses performed, results from cokriging interpolation and factor analysis maps suggest, at a sampling density of 500 m by 500 m, the location of the deposit, particularly elements Cu, Pb, Mn, Rb, Sr, and Zn and factors 1, 3 and 4. These elements and factors are deemed effective due to good quality control. Furthermore, the semi-anular shape for Cu and Sr are strongly dependable and robust results, evidencing the usefulness of the method in terms of surface response and anomaly detection for this specific case study.

Surprisingly, the results don't reflect any lithological pattern, and seemed to be controlled mainly by structure and groundwater hidrology and hydrogeology.

In conclusion, considering that at the beginning of this study the total area surveyed was 6.5 km by 9.5 km and that the size of a deposit that a type company looks for is at least about 2 km by 2 km (potential target area), it can be said that the gas-sampling technique used here successfully reduced the original area by approximately 70%, making it highly possible for a geologist, without prior knowledge of the location of the prospect, to hit the target and in this scenario soil gas prospection with collectors would constitute a viable tool to identify processes of oxidation of sulfide mineralization occurring underground.

This study also recognizes that the result of the soil gas distribution is dependant on external factors, particularly the presence of active faults and/or fractures, structures within the sedimentary cover, rock-water interaction, the sampling density, time of exposure and the dispersion processes acting among others. Thus, an adequate interpretation needs at least prior knowledge regarding the structures.

Although gas sampling technique have existed since the old times, it still need to be tested broadly, at least in above known deposits and if possible, in arid terrains.
With this study, now we know that some elements yields all concentration below detection limit, future application of this technique can help determine if these elements should not be measure at all next time or if their lack in response are particularly of the Atlántida geochemistry or suitable conduits to transport gas anomalies.

Also, future research needs to be done to help determine the transport mechanisms for specific elements released from the oxidation front.

Bibliography

Chapter 1

Aspandiar, M.F. 2004. Potential mechanisms of metal transfer through transported overburden within the Australian regolith: A review. Open File, Regolith 2004, p.18.

Aspandiar, M.F.; Anand, R.R.; Gray, D.J. 2008. Geochemical dispersion mechanisms through transported cover: Implications for mineral exploration in Australia. Open File Report 246, CRC LEME, Perth, 2008.

Bolviken, B.; Logn, O. 1975. An electrochemical model for element distribution around sulphide bodies, in I. Elliott and K. Fletcher, eds., Geochemical Exploration 1974: Elsevier, p.631-648.

Cameron, E.I.; Hamilton, S.M.; Leybourne, M.I.; Hall, G.E.M.; McClenaghan, M.B. 2004. Finding deeply buried deposits using geochemistry.

Clark, J.R. 1996. Unique significant Enzyme leach anomaly patterns in areas of tropical/subtropical weathering. Queen's University Conference Proceedings, Kingston, ON, p. 241 – 256.

Clark, J.R.; Yeager, J.R.; Roger, P.; Hoffman, E.L. 1997. Innovative Enzyme Leach Provide Cost-Effective Overburden/Bedrock Penetration: Proceedings of Exploration 97, p. 371 – 374.

Fabris, A.J.; Keeling, J.L.; Fidler, R.W. 2009. Soil geochemistry as an exploration tool in areas of thick transported cover, Curnamona Province. MESA Journal 54, September 2009.

Govett, G.J.S. 1973. Differential secondary dispersion in transported soils and post-mineralization rocks: An electrochemical interpretation, in M.J. Jones, ed, Geochemical Exploration 1972: Institute of Mining and Metallurgy, p. 81-91.

Hamilton, S.M.; Cameron, E.M.; McClenaghan, M.B.; Hall, G.E.M. 2004. Redox, pH, and SP variation over mineralization in thick glacial overburden. Part I: methodologies and field investigation at the Marsh Zone gold property: Geochem.: Explor., Environ., Anal. 4, p. 33 – 44.

Owens, L.B. 2013. Thesis submitted in Partial Fulfillment of the Requirements for the PhD degree: Geochemical Investigation of Hydrothermal and Volcanic System in Iceland, New Mexico and Antarctica, p. 9 – 10.

Noble, R.R.P.; Stanley, C.R. 2009. Traditional and novel geochemical extractions applied to a Cu-Zn soil anomaly: a quantitative comparison of exploration accuracy and precision. Geochemistry-Exploration Environment Analysis 9, p. 159 – 172.

Sato, M.; Mooney, H.M. 1960. The electrochemical mechanism of sulphide self-potentials: Geophysics, 25, p. 226-249.

Schode, R. 2014. The Global Shift to Undercover Exploration – How fast? How effective?, Society of Economic Geologist 2014 Conference, Keystone, Colorado, p. 16.

Smee, B.W. 1983. Laboratory and field evidence in support of the electrochemically-enhanced migration of ions through glaciolacustrine sediment: Journal of Geochemical Exploration, 19, p. 277-304.

Williams, T.M.; Gunn, A.G. 2002. Application of enzyme leach soil analysis for epithermal gold exploration in the Andes of Ecuador: Applied Geochemistry 17, p. 367 – 385.

Chapter 2

Amilibia, A., (2009). Compressional deformation along the Chañarcillo basin west margin: North Chilean Late Jurassic-Early Cretaceous back-arc basin, Trabajos de Geología, Universidad de Oviedo, 29, p. 78-83.

Arévalo, C., (2005a). Carta Copiapó, Región de Atacama. Servicio Nacional de Geología y Minería. Carta Geológica de Chile, Serie Geología Básica, 91, scale 1:100,000.

Arévalo, C., (2005b). Carta Los Loros, Región de Atacama. Servicio Nacional de Geología y Minería. Carta Geológica, Serie Geología Básica, 92, scale 1:100,000.

Arévalo, C.; Grocott, J.; Martin, W.; Pringle, M.; Taylor, G. (2006). Structural setting of the Candelaria Fe oxide Cu-Au deposit, Chilean Andes (27º30'S). Economic Geology 101, p. 819-841.

Arévalo, C.; Mourgues, F.A.; Jaillard, E.; Bulot, L.G. (2005). Comparative evolution of the Lower Cretaceous Pluto-volcanic arc and back-arc from the Atacama Region, Chile. *In* International Sysposium on Andean Geodynamics, No. 6, Extended Abstracts, p. 57-60. Barcelona.

Charrier, R.; Pinto, L.; Rodriguez, M. (2007). Chapter 3, Tectonostratigraphic evolution of the Andean Orogen in Chile, p. 21-114, in: *The Geology of Chile,* edited by Teresa Moreno and Wes Gibbons, published by The Geological Society.

Cooke, D; Hollings, P; Walshe, J. (2005). Giant Porphyry Deposits: Characteristics, Distribution, and Tectonic Controls. Economic Geology, August 2005, v. 100, p. 801-818.

Corvalán, J. (1974). Estratigrafía del Neocomiano marino de la región al sur de Copiapó, Provincia de Atacama. Revista Geológica de Chile 1, p. 13-36.

Corbett, G. (2004). Epithermal and Porphyry Gold – Geological Models, in Pacrim 2004 Congress, Adelaide, South Australia, p. 15 – 23.

Maksaev, V. (2001). Reseña metalogenica de Chile y de los procesos que determinan la metalogénesis andina.

Maksaev, V. (2005). World Skarn Deposits: Skarns of Chile.

Maksaev, V.; Munizaga, F.; Valencia, V.; Barra, F. (2009). LA-ICP-MS zircon U-Pb geochronology to constrain the age of post-Neocomian continental deposits of the Cerrillos Formation, Atacama Region, Northern Chile: tectonic and metallogenic implications. *Andean Geology 36 (2), p.* 264-287.

Maksaev, V.; Almonacid, T.A.; Munizaga, F.; Valencia, V.; McWilliams, M.; Barra, F. (2010). Geochronological and termochronological constraints on porphyry copper mineralization in the Domeyko alteration zone, northern Chile. Andean Geology 37 (1), p. 144 – 176, 2010.

Marschick, R.; Fontboté, L. (2001). The Candelaria-Punta del Cobre iron oxide Cu-Au (Zn-Ag) deposits, Chile. Economic Geology 96 (8), p. 1799-1826.

Martínez, F; Arriagada, C; Peña, M; Del Real, I; Deckart, K. (2012). The structure of the Chañarcillo Basin: An example of tectonic inversion in the Atacama region, northern Chile. Journal of South American Earth Science 42 (2013), p. 1-16.

Matthews, S.; Cornejo, P.; Riquelme, R. (2006). Carta Geológica de Chile, Carta Inca de Oro. Escala 1:100,000. Pages: 8-18.

Mourgues, F. A., (2007). La transgression du Crétacé Inférieur au Nord du Chili. Biostratigraphie, Paléontologie (Ammonites) Stratigraphie Séquentielle et Tectonique Synsédimentaire. Doctoral thesis (Unpublished). University of Toulouse, France.

Palacios, C; Townley, B; Lahsen, A; Egaña, A. (1993). Geological developmet and mineralization in the Atacama segment of the South American Andes, northern Chile (26º15' – 27º25'S).

Segerstrom, K.; Parker, R.L. (1959). Cuadrángulo Cerrillos, Provincia de Atacama. Instituto de Investigaciones Geológicas, Carta Geológica de Chile 2, p. 33, scale 1:50,000.

Segerstrom, K.; Ruiz, C. (1962). Cuadrángulo Copiapó, Provincia de Atacama. Instituto de Investigaciones Geológicas, Carta Geológica de Chile 6, p. 42, scale 1:50,000.

Sillitoe, (1998). Major regional factors favoring large size, high hypogene grade, elevated gold content and supergene oxidation and enrichment of porphyry copper

deposits, in Porter, T.M., ed., Porphyry and hydrothermal copper and gold deposits: A Global Perspective, Perth, 1998, Conference Proceedings: Glenside, South Australia, Australien Mineral Foundation, p. 21-34.

Tilling, R. (1962). Batholith Emplacement and Contact Metamorphism in the Paipote-Tierra Amarilla Area, Atacama Province, Chile. Unpublished Ph.D. Thesis. Yale University, New Haven CT USA, p. 195.

Chapter 3

Appleby, S. K. YEAR. U-Pb analysis of zircons: the Lochnagar Granite, NE Scotland.
Bissig, T.; Heberlein, D.R.; Dunn, C.E. 2013. Geochemical Techniques for Detection of Blind Porphyry Copper-Gold Mineralization under Basal Cover, Woodjam Prospect, South-Central British Columbia (NTS 093A/03,/06). Geoscience BC Summary of activities 2012, Geoscience BC, Report 2013-1, p. 63 – 78.

Bowring, S.A.; Schoene; B.; Crowley, J.L.; Ramezani, J.; Condon, D.j. YEAR. High-precision U-Pb zircon geochronology and the stratigraphic record: progress and promise.

Cohen, D.R.; Kelley, D.L.; Anand, R; Coker, W.B. 2007. Major Advances in Exploration Geochemistry, 1998 – 2007: Proceedings of Exploration 2007.

Hill, G.T.; Owens, L.; Norman, D.I. 2006. Surface Geochemistry in Exploration for a Buried Geothermal System, Socorro, New Mexico.

Maksaev, V.; Munizaga, F.; Valencia, V.; Barra, F. 2009. LA-ICP-MS zircon U-Pb geochronology to constrain the age of post-Neocomian continental deposits of the Cerrillos Formation, Atacama Region, Northern Chile: tectonic and metallogenic implications. *Andean Geology 36 (2), p.* 264-287.

Olson, N.; Dilles, J.; Cernuschi, F.; Kent, A. 2014. Zircon U-Pb Geochronology and Geochemistry in Northern Chile: Results from the Atlantida Prospect.

Schoene, B. 2013. U-Th-Pb Geochronology. In: Rudnick R (ed), Treatise on Geochemistry 3, Elsevier, Oxford, UK, in press.

www.appliedspectra.com/technology/LA-ICP-MS.html

www.chemiasoft.com/chemd/node/52

www.eag.com/mc/inductively-coupled-plasma-spectroscopy.html

www.elementalanalysis.com/services/inductively-coupled-plasma-icp/

Chapter 4

Filzmoser, Peter. 2006. Outlier Detection with Application to Geochemistry. Open file.

Piercey, S. 2014. Modern Analytical Facilities 2. A Review od Quality Assuance and Quality Control (QA/QC) Procedures fir Lithogeochemical Data. Geoscience Canada.

Chapter 5

Reiman, C; Filzmoser, P. 1999. Normal and Lognormal data distribution in geochemistry: death of myth. Consequences for the statistical treatment of geochemical and environmental data. Environmental Geology 39 (9) July.

Dol, W.; Verhoog, D. 2010. Common Agricultural Policy Regionalized Impact – The Rural Development Dimension.

Ben-Gal, Irad. 2005. Chaper 1: Outlier Detection. in: Maimon O. and Rockach L. (Eds.) Data Mining and Knowledge Discovery Handbook: A Complete Guide for Practitioners and Researchers," Kluwer Academic Publishers, 2005

Filzmoser, P.X. A multivariate outlier detection method.

Filzmoser, Peter.; Gschwandtner, Moritz. 2015. Package 'mvoutlier'.

Holland, Steve M. 2008. Principal components analysis (PCA).